8-22-2011

An Optical Analysis of the Blowoff Behavior for Bluff Body-Stabilized Flames in Vitiated Flow

Trevor Jensen
University of Connecticut - Storrs, trj08001@engr.uconn.edu

An Optical Analysis of the Blowoff Behavior for Bluff Body-Stabilized Flames in Vitiated Flow

Trevor Ray Jensen

B.S., Brigham Young University-Idaho, 2006

A Thesis

Submitted in Partial Fulfillment of the

Requirements for the Degree of

Master of Science

at the

University of Connecticut

2011

APPROVAL PAGE

Master of Science Thesis

An Optical Analysis of the Blowoff Behavior for Bluff Body-Stabilized Flames in Vitiated Flow

Presented by

Trevor Ray Jensen, B.S.

Major Advisor _____
Michael W. Renfro

Major Advisor _____
Baki M. Cetegen

Associate Advisor _____
Thomas J. Barber

University of Connecticut

2011

Acknowledgements

I express my gratitude to Pratt & Whitney for their financial support of this research.

Many thanks go to my major advisors, Professors Michael Renfro and Baki Cetegen, for their direction and encouragement in this research, and most especially their seemingly endless plethora of good ideas to combat my projects' tendencies toward a state of higher disorder. Thanks for introducing me to the wonderful world of fire and lasers. Special thanks, also, to Prof. Renfro for teaching the best class I've ever audited.

I acknowledge the help, ideas, and support of all of my lab colleagues, including Kathryn and the gentlemen from the center of excellence next door, Mark and Jared. Extra special acknowledgements go out to Kristin. Thanks for being a great lab assistant and helping me get all of my data for this thesis… ok, maybe I was the assistant. Still, panda-sized thanks for all of your help.

Extra, extra special acknowledgements to my wife, Shannon. Thanks for your help, love, support, involvement, encouragement, intellect, work ethic, magnanimity, formatting skills, and hotness. Couldn't have/wouldn't have done it without you.

Table of Contents

Table of Figures

Table of Tables

ABSTRACT

In bluff body-stabilized flames, a variety of physical phenomena contribute to the flame destabilization as lean blowoff is approached. These effects include increased strain on the flame shear layers, decreased attenuation of Bénard-von Kármán vortex shedding, and the presence of thermoacoustic instabilities. Lean, bluff body-stabilized flames were studied in an enclosed rectangular-duct, turbulent combustion rig with a triangular flame holder under vitiated conditions with both symmetric and asymmetric fuel distributions. Air and fuel flows within the rig were characterized using a PIV system and a continuous emissions gas analyzer, respectively.

High-speed videos of these flames undergoing blowoff were taken to serve as the primary data source for analysis. To examine the effects of Bénard-von Kármán vortex instabilities and local strain-induced extinctions on the lean blowoff process, proper orthogonal decomposition (POD) algorithms were applied to the frames of the high-speed videos. POD mode shapes representing each of these phenomena were extracted and the relative contributions of these mode shapes were plotted over time as the flame approaches blowoff. Time-series analysis was also performed on a trace of the pressure oscillations and POD mode coefficients for a preliminary examination of the relevant acoustic influence on the blowoff event.

For future application to the turbulent combustion rig, a tunable diode laser absorption spectroscopy (TDLAS) system was developed. A TDL with a center wavelength in the near infrared region was simultaneously scanned across absorption lines of H_2O and CO_2

to obtain temperature and species concentration data. A McKenna Flat Flame burner was used to create a calibration environment for these measurements. Both direct and wavelength-modulated spectroscopy methods are examined, and their respective viability for use in the combustion rig is discussed.

1 Motivation

When premixed combustion occurs, it often takes place in a narrow reaction zone which separates the burned products and unburned reactants [1], and then propagates normal to itself. The propagation rate of the reaction front into the unburned stream is termed the flame speed. In many typical combustors, the reactant mixture velocity is two or more orders of magnitude greater than the stoichiometric laminar flame speed of most fuels. A flame propagating in such a flow would be convected downstream and never stabilize without an eddy region, or recirculation zone, to anchor the flame. The recirculation zone entrains hot combustion products from the flame shear layers, which then serve as an ignition source to the oncoming unburned reactants [2].

Recirculation zones are formed by flow separation in several ways: step combustors use a sudden expansion in the flow, swirl combustors use swirling jets, and bluff body combustors employ a fluid jet or geometric structure, to name a few. The development of a recirculation zone downstream of a bluff body is shown in Figure 1.1.

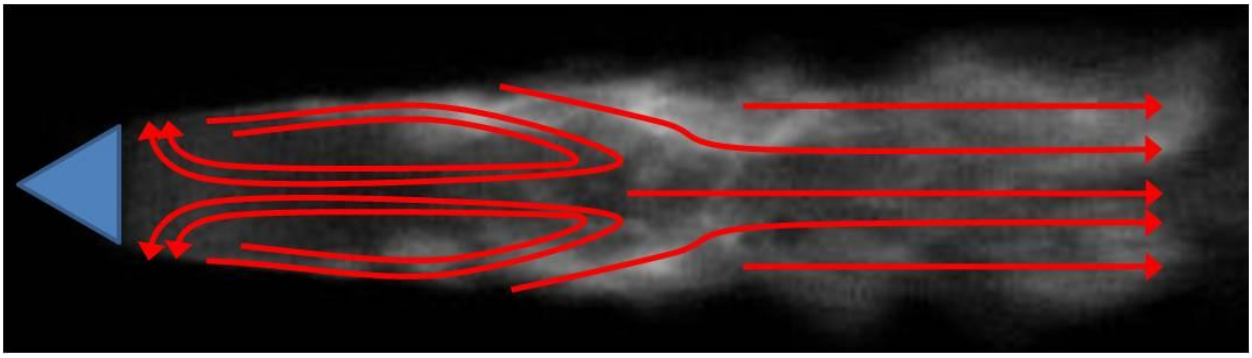

Figure 1.1: Diagram of flow over a bluff body. Adapted from Tuttle [3].

The streamlines depict that some of the combustible mixture that flows over the bluff body and ignites in the flame shear layers will then flow upstream to ignite new reactants. This creates a stable flame, anchored to the bluff body.

The use of recirculation zones for flame anchoring is well documented [4] and currently finds industrial application in both ground-based power systems and aircraft engines. While the ability of recirculation zones to fulfill the spatial and temporal requirements of combustion processes to effectively stabilize a flame is well understood, the conditions and physics which destabilize such an anchored flame is still an area of active research.

Bluff-body combustors, the focus of this research, support stable combustion under a limited range of fuel distributions for a given airflow. A variety of effects contribute to the deterioration of flame stability at the extremes of a bluff-body's operational envelope. These include thermo-acoustic instabilities, increased strain on the flame shear layers, and enhanced presence of asymmetric Benard-Von Kármán vortices [5, 6, 7]. The combination of these effects with a dynamic fuel distribution can lead to flame extinction, an event referred to hereafter as blowoff. Figure 1.2 shows a flame breaking along the reaction zone due to high strain exposure.

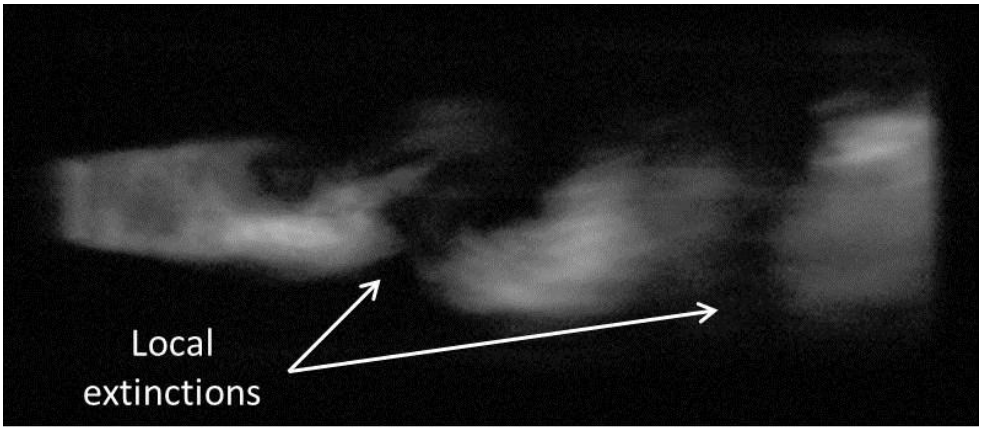

Figure 1.2: Flame extinctions.

Figure 1.3 displays a drawing of the experimental bluff body rig (discussed in detail in Ch. 2). It is clear that the fuel injectors are quite close to the bluff body flame holder. The limited fuel-air mixing time inherent in this design can produce undesired, local rich and lean zones that further enhance the strain and vortex instabilities discussed. To accurately predict the conditions leading up to blowoff, the physics of these combustion instabilities should be well understood.

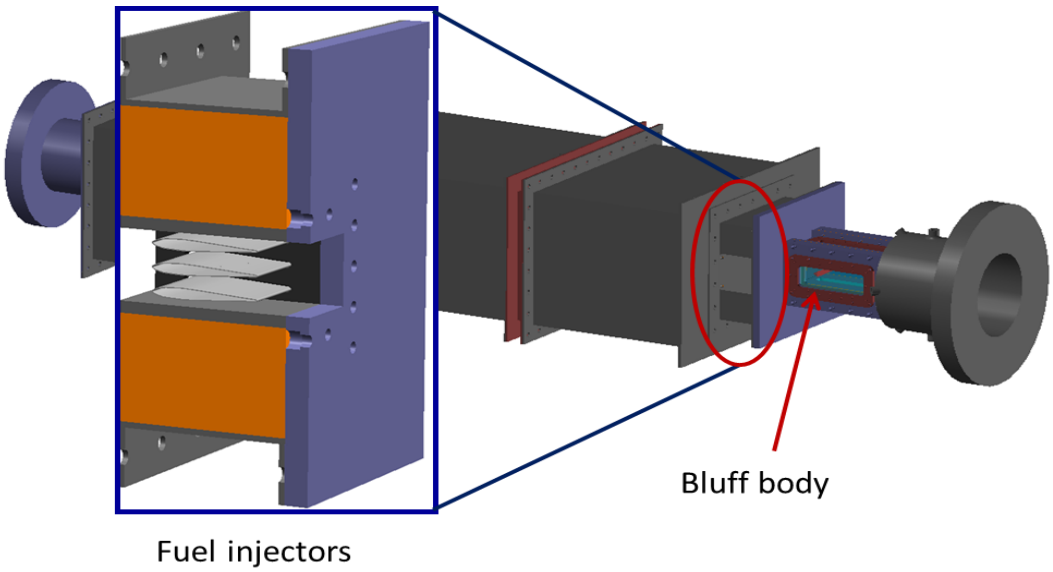

Figure 1.3: Proximity of fuel injectors to bluff body in experimental rig [3].

Bluff bodies are used as flame anchors both in primary combustors and augmentors [8-9]. Augmentors naturally operate in vitiated conditions, breathing the combustion products of the primary combustor. Aircraft augmentors are particularly subject to dynamic environments. Lower temperatures and pressures from high-altitude operation slow both molecular transport and chemical reaction rates. Conditions from the opposite operational extreme, such as high temperatures, high Mach number, and high air flow rates at low altitude, increase molecular transport and sensitivity to turbulent effects [10]. These augmentors also experience all the accelerations of high-speed flight, which can result in fueling profiles with different degrees of stratification. To the end of minimizing afterburner blowoff occurrences, this research explores various optical diagnostic and analysis techniques to understand the contribution of the aforementioned combustion instabilities to the lean blowoff event in a bluff body combustion rig. Studies were conducted with vitiated air flow and stratified fuel profiles, mimicking the conditions present in aircraft afterburners.

1.1 Turbulent Premixed Flames

To understand the theories governing the lean blowoff process in these bluff body-stabilized flames, the dynamic behavior of turbulent partially-premixed flames must be understood. In premixed flames, the fuel and oxidizer are in a mixture that is nearly uniform in both temperature and composition. However, it is presently more common for the fuel distribution across a second-stage combustor to be characterized as partially premixed. As advances in cooling design and material sciences have been made, operating temperatures and pressures in aero gas turbine engines have increased. As a

result, the augmentor fuel injection has migrated much closer to the flame holder to discourage autoignition in these higher temperature and pressure conditions. This also decreases fuel and air mixing time, making the assumption of a fully premixed flame inaccurate [9].

In turbulent environments, the propagation of the flame reaction front can be influenced by turbulence, either preexisting in the flow or generated by the combustion process. Turbulent eddies can penetrate the thermal diffusion layer, increase downstream mixing, and enhance thermal and mass transport. As the reaction rate is limited by thermal and mass diffusion of the hot products to the cold reactants, it follows that turbulence will modify the reaction rate. Damköhler [11] first proposed describing turbulent premixed flames as wrinkled laminar flames whose reaction rates increase proportionally to the increased flame surface area due to wrinkling. Many models today still rely on this concept [12-13].

Flame wrinkling from stretch is a result of the normal and tangential flow velocity components on the flame surface. A general definition of stretch rate at a point on the flame surface of area *A* is given by:

$$\kappa = \frac{1}{A}\frac{dA}{dt} \tag{1.1}$$

Law [14] breaks up the effects of stretch into two highly-coupled categories: hydrodynamic stretch and flame stretch. Hydrodynamic stretch is a physical displacement and warping of the flame surface geometry, which yields an increase in

flame surface area and a change in burning rate across the surface. Flame stretch refers to the effect of the tangential velocity on the mass flux into the reaction zone, which modifies the temperature and concentration profiles in the transport region. These phenomena are important to this study as they can affect flame extinction by altering the time available for combustion to occur in the reaction zone.

1.2 Bluff Body-Separated Flows

Flow past a bluff body will generate vorticity above and below the bluff body, opposite in sign. It is well known that in non-reacting flows, the interaction of these vorticity regions creates large-scale, asymmetric vortices, termed Benard-von Kármán (BVK) vortices, which shed from the base of the bluff body [15]. BVK disturbances are termed absolute instabilities because they persist independent of external forcing [16]. BVK instabilities are periodic, forming a sinuous wake with a characteristic frequency given by:

$$f_{BVK} = St\frac{U}{L} \tag{1.2}$$

where *St* is the Strouhal number, *U* is velocity, and *L* is the characteristic length, which in this case is the height of the bluff body. When a flame anchors to the bluff body and heat is released, a temperature gradient, and thus a density gradient across the flame are naturally produced. The effect of heat release on the BVK vortex street is shown mathematically by the vorticity transport equation below and is well-explained in [17]:

$$\frac{D\vec{\omega}}{Dt} = (\vec{\omega}\cdot\nabla)\vec{V} - \vec{\omega}\left(\nabla\cdot\vec{V}\right) + \frac{1}{\rho^2}\nabla\rho\times\nabla P + \nu\nabla^2\vec{\omega} \tag{1.3}$$

where ω, V, ρ, P, and ν denote vorticity, gas velocity, density, pressure, and kinematic viscosity, respectively.

There are many physical processes accounted for in the above equation, namely vortex stretching in the first term on the right, a vorticity sink from gas expansion in the second, baroclinic vorticity production in the third, and viscosity-dependent diffusion in the fourth term. This shows that the presence of a flame causes temperature-sensitive vorticity generation due to dilatative, baroclinic, and viscous effects. This vorticity will compete with the shear-generated vorticity off of the bluff body. Thus, the BVK instabilities in a strongly-burning flame are effectively damped out. Flames in these conditions will be dominated, instead, by Kelvin-Helmholtz (KH) shear layer instabilities. The flames studied here, stabilized on a triangular bluff body, are prone to both KH and BVK instabilities, as shown in Figure 1.4.

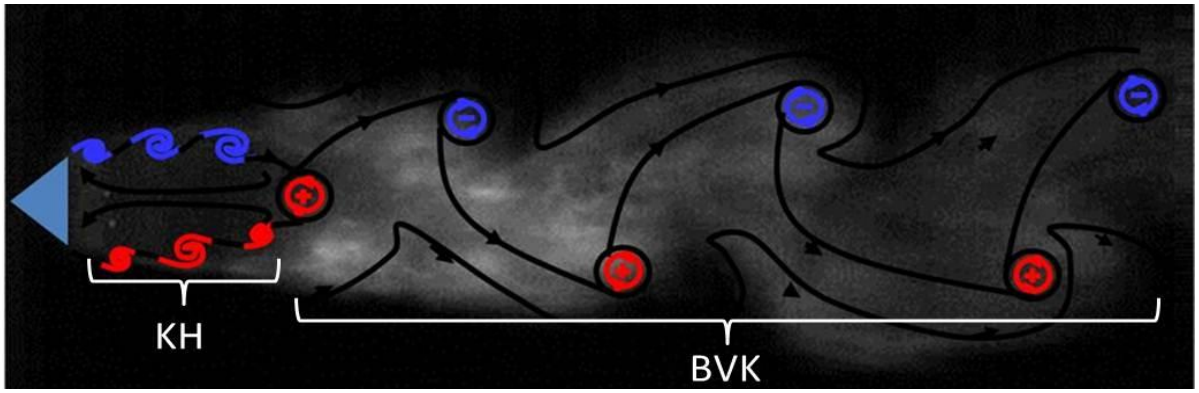

Figure 1.4: Vorticity illustration showing the presence of both KH and BVK instabilities in a flow field. Adapted from [3]

Kelvin-Helmholtz vortices are symmetric, locally convective instabilities which roll up into tightly concentrated vorticity packets that are swept away from the bluff body

surface [18]. These occur in the near-field of the wake, close to the bluff body, at a frequency indicated by the expression [19]:

$$f_{KH} = 0.0235 f_{BVK} \cdot Re^{0.67} \tag{1.4}$$

At high Reynolds numbers, KH instabilities clearly have a much higher characteristic frequency than BVK vorticies.

The BVK vortices in a stable, unvitiated flame are damped, as discussed with Eq. 1.3, by the effects of a large density gradient, among others. However, as the equivalence ratio of the mixture decreases and the flame is brought closer to blowoff, the flame temperature also decreases, which in turn decreases the dilatation ratio across the flame sheet. Thus, in unsteady, unvitiated flames near blowoff, the presence of BVK vortices can still be observed [17]. Figure 1.5 shows two LES images from high dilatation ratio-flames. When the equivalence ratio of the flame is brought to a less-stable region, BVK instabilities are apparent.

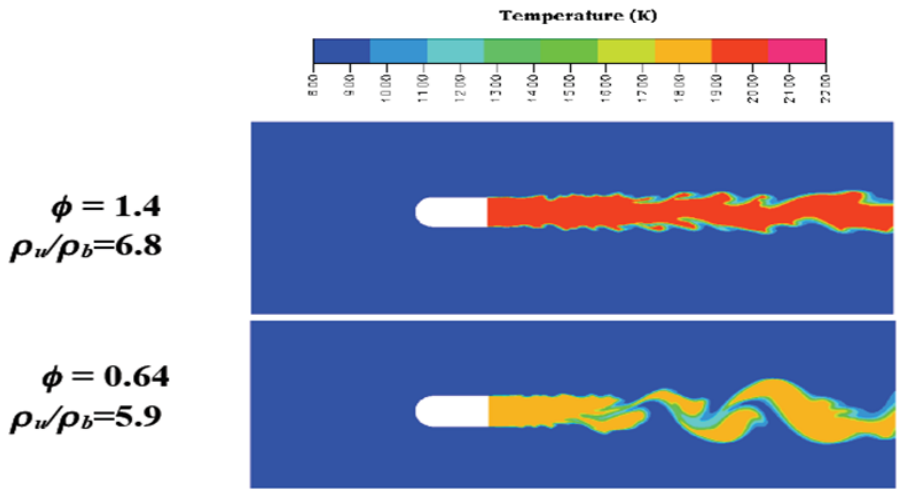

Figure 1.5: High dilatation ratio flames [17].

In vitiated flames the temperature of the ambient bulk flow is much nearer to that of the flame, and a smaller density gradient exists between the burned and vitiated gases. This environment provides a decreased attenuation of the BVK vortices, allowing them to dominate the flame dynamics, particularly near blowoff [20].

1.3 Blowoff Mechanisms

The first steps to identifying the underlying physics behind blowoff were observations of transient characteristics in bluff body flames immediately prior to extinction. Nicholson and Field [21], and Thurston [22] were among the first to observe this transient behavior, which they characterized as large-scale pulsations or oscillations of the flame. One of the first theories to describe actual blowoff mechanics came from investigations by Williams, et al. [23]. Williams posited that combustion will desist when insufficient heat is transferred from the hot products to the cold reactants to sustain ignition. Longwell [24] similarly suggested that the rate of reactant entrainment into the recirculation zone needs to balance the burning rate in order to avoid flame extinction. This was followed by a hypothesis from Zukoski and Marble [25] that the time scale of reactant and product interaction must exceed a critical ignition delay time. This time scale will be related both to the length of the recirculation zone, which is affected by the geometry of the flame holder [26-27], and to the aerodynamic and chemical time scales of the mixture, which can be represented by a Damkohler number, defined here [11, 28]:

$$Da = \frac{\tau_{flow}}{\tau_{chem}} \tag{1.5}$$

where τ_{flow} is the characteristic flow timescale and τ_{chem} is the characteristic chemical reaction timescale.

Another parameter shown to be a significant player in blowoff dynamics is the strain rate to which the flame is exposed [29-32]. As local strain rates exceed the extinction strain rate, local flame extinctions occur [33]. However, overall flame extinction is observed to occur significantly before the average strain rate reaches the extinction strain rate [34-36]. This suggests that a large-scale, localized extinction event can cause irreparable damage to the flame shear layers. This effect was put into a more comprehensive blowoff mechanism by Chaudhuri, et al. [37]. They showed that partial flame extinctions occur along the shear layers due to instantaneous exceeding of critical strain rates by KH vortices when the equivalence ratio and flame speed decrease. A cycle of intermittent re-ignitions of the flame shear layers due to flame retraction into the recirculation zone and further flame extinctions is then observed. Chaudhuri, et al., write that this process eventually leads to blowoff when the shear layers become sufficiently unreactive. Their work was performed on unvitiated, symmetrically-fueled flames.

This investigation examines the effects of both vitiation and fuel stratification on the blowoff process. It is uncertain whether combustion within the recirculation zone near blowoff is a phenomenon that exists in vitiated flames. To gain new insights into these issues, additional diagnostic approaches are explored. Among these is the development of a method that will provide high-frequency temperature measurements in the

recirculation zone. Such data could determine, among other things, the presence of recirculation zone burning where visual approaches struggle.

1.4 Tunable Diode Laser Absorption Spectroscopy

A significant portion of the work presented here was spent on the development of a tunable diode laser absorption spectroscopy (TDLAS) application for an experimental bluff body combustion rig (described in detail in Ch. 2). This was done in order to provide accurate, high-frequency temperature and species measurements of the flame near blowoff. As such, a background of the physics and application of TDLAS is presented here.

1.4.1 Infrared Absorption

Molecules have a number of different physical means by which they can transition between quantum energy levels, thereby absorbing or emitting electromagnetic energy. The most energetic nonnuclear transitions are electronic, in which an electron transitions between shells, subshells, orbitals, or spin states. Less energetic transitions involve changes in the rotational and vibrational energy states of the molecule.

Infrared radiation is not sufficiently energetic to induce electronic transitions in most molecules. Thus, infrared absorption is generally limited to molecular species that have small energy gaps between various vibrational and rotational states. It can be shown that for heteronuclear molecules, vibrational transitions will always be accompanied by rotational transitions [38]. These energy changes couple to produce a rovibrational spectrum. The rovibrational motion causes the molecular charge centers to shift which

results in a change in dipole moment, allowing absorption to occur. It is this process that prevents monatomic species like O_2 or N_2 from absorbing infrared radiation, as they experience no net dipole moment change from vibrational or rotational transitions. Conversely, heteronuclear molecules like CO_2, the species of interest in this study, prove to be particularly sensitive to infrared absorption.

1.4.2 Beer-Lambert Law

A basic TDLAS setup consists of a tunable diode laser source with controllers for tuning, beam shaping optics, a gaseous absorption sample, and a photodiode for detection.

Typical tunable diode lasers emit light in the infrared. When the laser emission is tuned to a characteristic absorption line of the absorbing medium, the signal intensity measured by the photodiode will decrease according to the Beer-Lambert law [39]:

$$\frac{I}{I_0} = e^{-\int_0^L \alpha \cdot dl} \tag{1.6}$$

Where I is the measured laser intensity, I_0 is the incident laser intensity, L is the path length (cm), and α (cm^{-1}) is the absorption coefficient of the absorbing gas. The absorption coefficient is a path-integrated value that will give an average measurement across the path length. It can be calculated by [40]:

$$\alpha = 2 \cdot P_s \cdot S(T, v_0) \cdot \frac{\sqrt{\frac{\ln(2)}{\pi}}}{\alpha_D} \cdot V(X, Y) \tag{1.7}$$

where P_s is the partial pressure (atm) of the absorbing gas, $S(T,v_0)$ is the line intensity ($cm^{-2}\cdot atm^{-1}$) of the transition line, T is temperature (K), v_0 is the wavenumber (cm^{-1}) of the transition line center, and $V(X,Y)$ is the Voigt function to account for line broadening.

Temperature-dependent line strength is calculated with respect to known line strength at a reference temperature, T_0 [40]:

$$S(T,v_0) = S(T_0)\frac{Q(T_0)}{Q(T)}\frac{[1-e^{\left(-hc\frac{v_0}{kT}\right)}]}{[1-e^{\left(-hc\frac{v_0}{kT_0}\right)}]}e^{[\left(\frac{hcE''}{k}\right)\left(\frac{1}{T_0}-\frac{1}{T}\right)]} \quad (1.8)$$

Where Q is the molecular partition function of the absorbing gas, h is Planck's constant (J·sec), c is the speed of light (cm/sec), k is Boltzmann's constant (J/K), and E'' is the lower-state energy of the transition (cm^{-1}).

In the Voigt function, the parameters are defined as follows:

$$X = \frac{2(\nu-\nu_0)}{\alpha_D}\sqrt{\ln(2)} \quad (1.9)$$

$$Y = \frac{\alpha_L}{\alpha_D}\sqrt{\ln(2)} \quad (1.10)$$

where α_D is the Doppler halfwidth and α_L is the Lorentzian halfwidth. These quantities and concepts are discussed subsequently.

1.4.3 Spectral broadening

Spectral broadening occurs in a line shape for several reasons [39, 41], including power broadening, Doppler broadening, transit-time broadening, pressure broadening, and natural lifetime broadening. However, there are usually only two dominant broadening effects in a TDLAS experiment applied to atmospheric gases. The first of these is

Doppler broadening. Doppler broadening is a result of the random velocity of the gas molecules relative to the light wave. Each photon that propagates through the absorbing gas will be red or blue shifted depending on the velocity of the individual gas molecules. As this effect is dependent on the distribution of molecular velocities, the lineshape function will be defined by combining the Doppler effect equation from classical physics with the Maxwell-Boltzmann distribution [38]:

$$Y_D(\nu) = \frac{1}{\nu_0}\left(\frac{mc^2}{2\pi kT}\right)^{\frac{1}{2}} e^{-mc^2(\nu-\nu_o)^2/2kT\nu_0^2} \tag{1.11}$$

where ν is the emitted wavenumber, ν_0 is the line center wavenumber, m is particle mass, T is temperature, k is Boltzmann's constant, and c is the speed of light. A common quantity used in characterizing this lineshape is the full width at half maximum (FWHM), which is given by:

$$\Delta\nu_D = \sqrt{\frac{8kTln(2)}{mc^2}}\nu_0 \tag{1.12}$$

Combining this with Equation 1.11, the Doppler line shape function in terms of its FWHM is [38]:

$$Y_D(\nu) = \frac{2}{\Delta\nu_D}\sqrt{\frac{\ln(2)}{\pi}}\, e^{-4\ln(2)\left({}^{(\nu-\nu_0)}/_{\Delta\nu_D}\right)^2} \tag{1.13}$$

This lineshape function is immediately recognized as Gaussian by nature, and broadens as the temperature of the absorbing media increases.

The second non-negligible form of lineshape broadening is collisional, or pressure broadening. In 1905, Lorentz hypothesized that if a molecule elastically collides with another molecule while absorbing or emitting radiation, the phase and amplitude of the radiation can be altered [42]. As the pressure of the absorbing gas increases, the number of collisions per second per atom increases and the line broadens. The equation describing this lineshape in terms of its FWHM is given by:

$$Y_C(\nu) = \frac{\Delta\nu_C}{2\pi}\frac{1}{(\nu-\nu_0)^2 + (\Delta\nu_C/2)^2} \tag{1.14}$$

where the FWHM $\Delta\nu_C$ is defined as:

$$\Delta\nu_C = \frac{2Z^*}{\pi} \tag{1.15}$$

and Z^* is the molecular collisional frequency. Collisions between some molecular pairs will be more effective at broadening than others [38].

The experimentally observed spectral line profile is a convolution of the Gaussian and Lorentzian functions that describe the Doppler and collisional broadening effects. This convolved lineshape, called the Voigt profile, is defined as follows:

$$Y_V(\nu, \Delta\nu_C, \Delta\nu_D) = Y_D \otimes Y_C \tag{1.16}$$

$$= \frac{\sqrt{\ln(2)\,a}}{\pi^{3/2}} \int_{-\infty}^{\infty} \frac{-\ln(2)\,(\nu' - \nu_0)^2/\Delta\nu_D^2}{(\nu-\nu')^2 + \Delta\nu_L^2}\, d\nu' \tag{1.17}$$

where the a parameter is a ratio of the Lorentzian and Gaussian halfwidths:

$$a = \frac{\Delta\nu_L}{\Delta\nu_D} \tag{1.18}$$

Figure 1.6 shows a comparison of a Gaussian, Lorentzian, and Voigt profiles with normalized intensity and equal halfwidth.

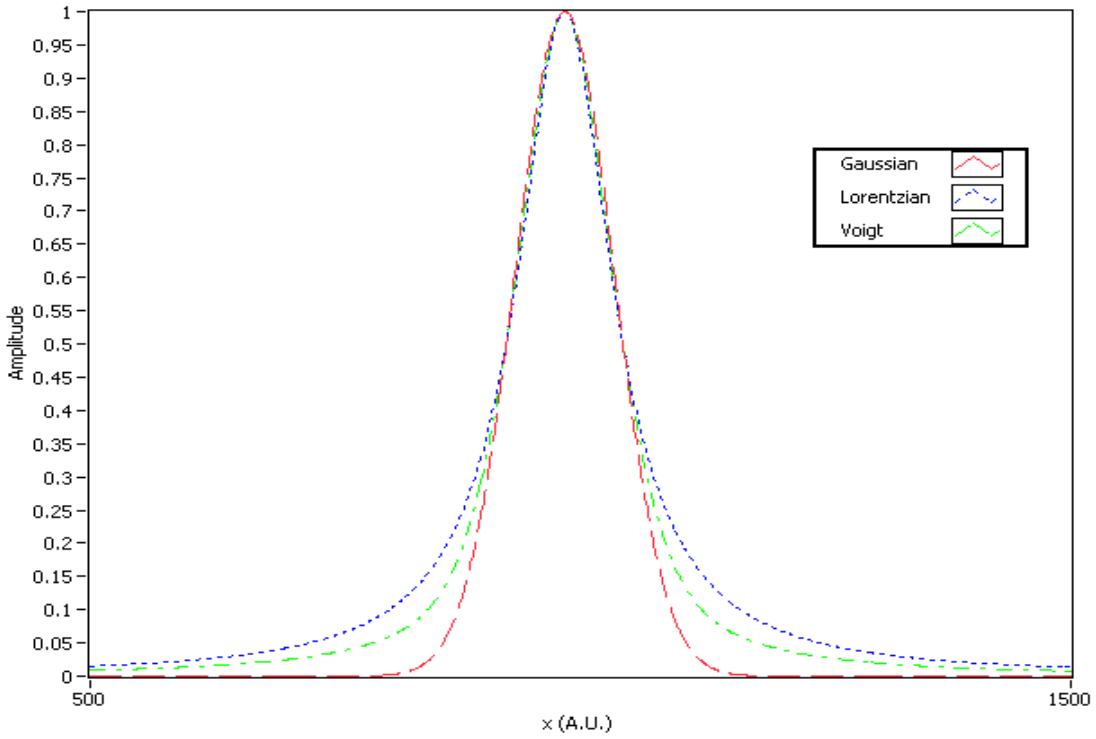

Figure 1.6: Comparison of Gaussian, Lorentzian, and Voigt profiles

The Lorentzian function has the broadest wings, while the Gaussian is narrower and the Voigt falls in between the two.

There are various ways of generating the Voigt profile for the purposes of lineshape fitting [43-45]. For this work, the algorithm of Liu, et al., [46] was implemented. This algorithm offers an analytical approximation to the Voigt profile by generating it through a weighted sum of Lorentzian and Gaussian functions. Liu, et al., [46] report

that the maximum errors of line curve width and area in this weighted sum method are 0.01% and 0.2% respectively.

1.4.4 Modulation Spectroscopy

Common experimental techniques in TDLAS involve the use of modulation spectroscopy. This can take two forms: wavelength modulation spectroscopy (WMS) [47] and frequency modulation spectroscopy (FMS) [48]. The main difference between these two methods is that in the former, the modulation frequency is small compared to the line halfwidth, and in the latter, it is large. The underlying principles for these two techniques are the same, however. In general, the signal corresponding to the output wavelength of the laser is modulated at a high frequency, while the DC component is tuned across the wavelength of interest. The signal received by the detector is then processed by a lock-in amplifier which simultaneously retrieves the first (1f) and second (2f) harmonics of the absorption profile by referencing the modulation frequency and its second multiple. Taking a ratio of the 2f to 1f signals eliminates the need to account for the baseline laser intensity, as well as any corrections for photodetector gain and laser alignment [49-50]. This method increases sensitivity over direct absorption spectroscopy when gas concentrations or signal to noise ratios are low [50-51].

WMS techniques have been applied to hydrocarbon combustion flames to achieve simultaneous measurements of velocity, temperature, and partial pressure of the species of interest [52-53]. This information comes out of the Doppler shift, intensity ratio, and collisional broadening of the resultant absorption profiles, respectively. Near infrared (NIR) diode lasers are a viable and popular choice with this technique, due in

part to their development for the telecommunication and optical storage industries [54-55]. As a result of this development, NIR diode lasers have become increasingly economical and robust.

In the remaining chapters of this thesis, the exact experimental configurations used in data collection for both bluff body-stabilized combustion and TDLAS will be described and characterized. The data obtained from the combustion rig is presented in stages along with its primary method of analysis. The evolution of the analysis methodology is covered. Multiple TDLAS techniques and their application to the current setup are then reviewed. Finally, future steps and developments for this work are discussed.

2 Combustion Rig Setup

Blowoff experiments were performed in an augmenter-scaled turbulent combustion rig, shown in Figure 2.1.

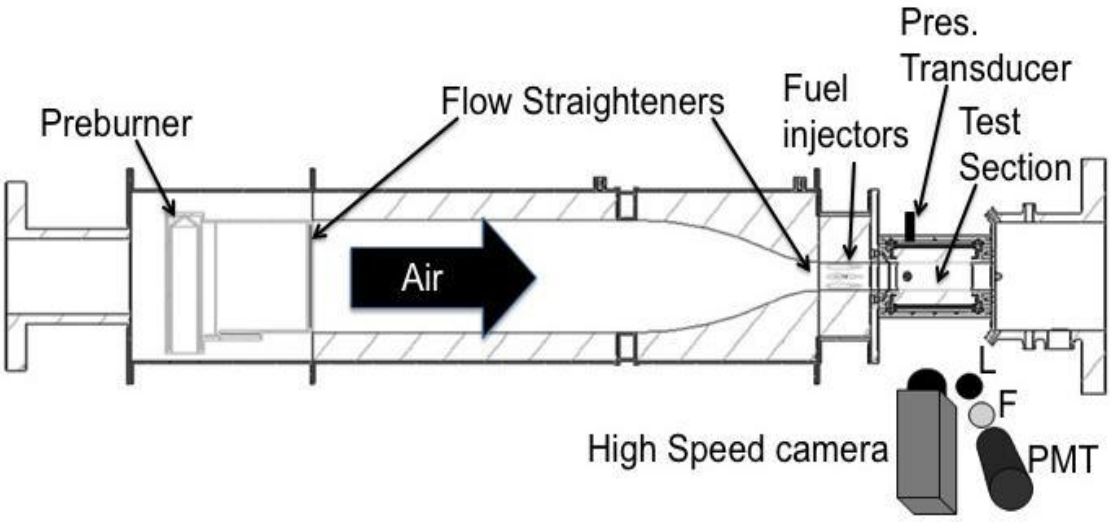

Figure 2.1: Experimental Bluff Body Combustion Rig [3].

Dry, room-temperature air entered the rig and passed through a Maxon NP-LE duct burner, which burned gaseous propane for vitiated tests. Most of the air through the duct burner was diverted around a primary combustion region burning near stoichiometric and used for dilution such that the overall equivalence ratio was 0.17. The gas stream then proceeded through a flow straightener, followed by a Kast-O-Lite-insulated settling section to allow for mixing of the vitiated combustion products. The gases were then accelerated past a seed injector pipe and through a convergent nozzle. These sections were followed by another flow straightener and three airfoil injectors, where propane fuel for the main burner was injected.

The vitiated air and fuel mixture then passed into the experimental test section, optically-accessible through a 38 x 127-mm quartz window, where a 9.62-mm equilateral triangular bluff body was placed mid-span across the duct (76.2 mm wide by 38.1 mm high). To ensure gap closure between the bluff body and the quartz window, small triangles of graphite gasket were affixed to the tip of the bluff body, preventing bypass leakage while accommodating the thermal expansion. A 19-mm quartz window was placed on the top of the test section for laser or camera access, which could be replaced by a steel blank with ports for a pressure transducer or other probes. Downstream of the test section window, five water spray nozzles were used to extinguish any propagating flames before they reached the exhaust. A steel-wool muffler was added to the end of the rig to damp some of the natural acoustics. A perforated plate was also inserted into the exhaust pipe to damp an 80-Hz longitudinal acoustic mode that is assumed to run from the atmospheric exit of the exhaust on the building roof to the flow straightener immediately upstream of the fuel injectors. Unvitiated tests were performed in the same rig, but without the activity of the preburner.

The fuel injectors were spaced at intervals of approximately 10 mm (one bluff body height). Each injector was fueled through a separate channel which allowed them to produce both spatially uniform and non-uniform fuel/air mixture profiles. The fuel flow through each channel was metered by a feedback loop that controlled a pressure regulator which measured the fuel pressure upstream of a calibrated, near-choked orifice.

A row of 1.5-mm holes was drilled along the thickest section of the airfoils for the fuel to exit. Experimental testing confirmed that varying the number of holes along the fuel struts did not affect the distribution or quantity of fuel dispensed.

Choked conditions exist when the exit velocity of the gas out of a nozzle or orifice becomes sonic, or Mach 1. In terms of the upstream to downstream pressure ratio, choked flow occurs when the following criterion is met:

$$\frac{P_u}{P_d} \geq \left(\frac{k+1}{2}\right)^{\frac{k}{k-1}} \tag{2.1}$$

where *k* is the specific heat ratio, c_p/c_v, of the gas [56]. For propane, which has a *k* value of 1.131, the upstream to downstream pressure ratio must be at least 1.73 to reach choked conditions.

Local regulations restricted the pressure of propane flowing into the building which housed the rig to 20 psig. As the rig was exposed to atmospheric pressure, such conditions make it impossible to achieve choked flow. However, for these experiments, the calibrated orifices were operated only in a region where fuel flow response to the regulator's input voltage was linear, thus mimicking choked conditions and allowing the flow to be well-characterized.

2.1 Auxiliary Setup

Two high-speed imaging setups were used (see Figure 2.2). The first involved two Phantom cameras (v12.1 and v7.3) focused on the bluff body from the top and side windows. Images were captured at a rate of 5000 frames per second with an exposure

time of 200 µs. The second setup used a single Photron camera at 10000 fps with a 100-µs exposure time. A photomultiplier tube (PMT) was focused through an objective lens on the bluff body wake. The PMT used a 432-nm band pass filter to primarily collect CH* chemiluminescence from the flame. When the luminosity of the shear layers dropped below a threshold value for longer than 50 ms, a trigger pulse was sent to the camera, which turned off image acquisition and preserved the existing data in the camera buffer.

In experiments involving the blowoff event, the flame would be brought to extinction by holding the air flow constant and reducing the equivalence ratio via fuel flow at a rate of approximately $\frac{\Delta\Phi}{\Delta t}$ =0.01/min until blowoff occurred.

Figure 2.2: High-speed setup.

In addition to the high speed video and CH* chemiluminescence data, a Kulite dynamic pressure transducer was connected through a port at the combustor wall above the bluff body wake to capture acoustic pressure fluctuations. Both the pressure transducer and the PMT signals were collected with a sampling rate of 10 kHz.

2.2 Combustion Rig Characterization

Various levels of stratification in the fuel profile, termed "fuel gradients," were used in experimentation. These were achieved by injecting varying fuel flows through the separate injectors, while keeping the difference between any two actively fueled injectors constant. The reported fuel gradients represent the difference in injected equivalence ratio between the bottom two channels, as computed by:

$$\xi \equiv \frac{(\Phi_3 - \Phi_2)\mathrm{h}}{\mathrm{s}} \tag{2.2}$$

where Φ_x represents the injected equivalence ratio in fuel channel x, h is the height of the bluff body, and s is the separation between the fuel injectors. For most stratified cases (ξ=0.50, 0.75, 1.00), the top injector was capped and not provided any fuel, keeping its injected equivalence ratio at a constant zero. Thus, as the equivalence ratio in the second and third airfoils varied, their relation to the first was not fixed. One stratified case (ξ=0.25) was explored, however, where the top injector was used, and its injected equivalence ratio followed the same pattern as the other two, such that the difference between it and the equivalence ratio from the neighboring injector would also describe the gradient. Naturally, for the unstratified "flat" cases, all three fuel

injectors were employed and injected with the same fuel flow per side. Figure 2.3 is a drawing of the fuel injector layout.

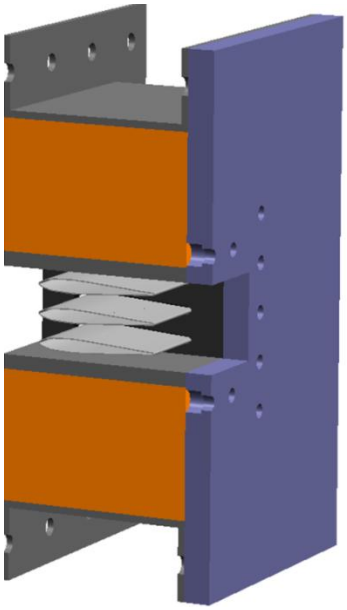

Figure 2.3: Fuel injector layout.

In each case, no fuel was injected through the top of the first fuel channel or the bottom of the third channel. That is, fueling was done only between the injectors, not in the space between the outer injectors and the chamber. This was done to minimize the concentration of unburned hydrocarbons in the exhaust.

Fuel distribution profiles were quantified using a Horiba MEXA 584-L continuous emission analyzer. A stagnating sampling probe was inserted through a port in the top face of the test section, immediately downstream of the bluff body. The fuel/air mixture entered the probe and passed through a 31-cm water-cooled, parallel-flow heat exchanger, intended to handle vitiated temperatures and cool the mixture prior to reaching the gas analyzer. The probe-heat exchanger system was affixed to a translation

stage to raise or lower the probe in increments of about 1.5 mm. Data was taken across the entire span of the test section, both vertically and transversely, and is shown in Figure **2.4**-5.

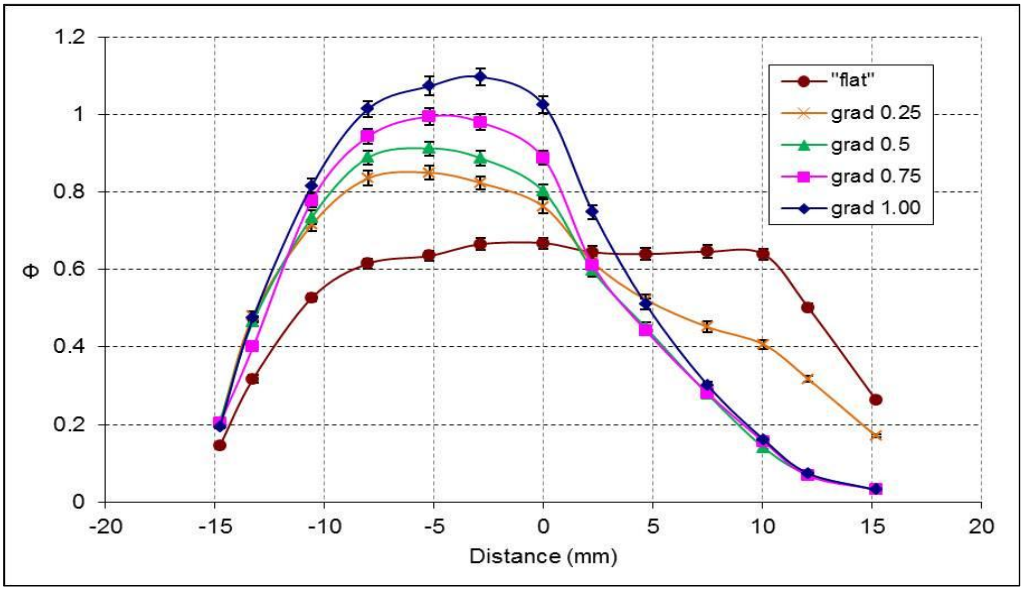

Figure 2.4: Fuel profiles of a flat case and all four gradient cases mentioned.

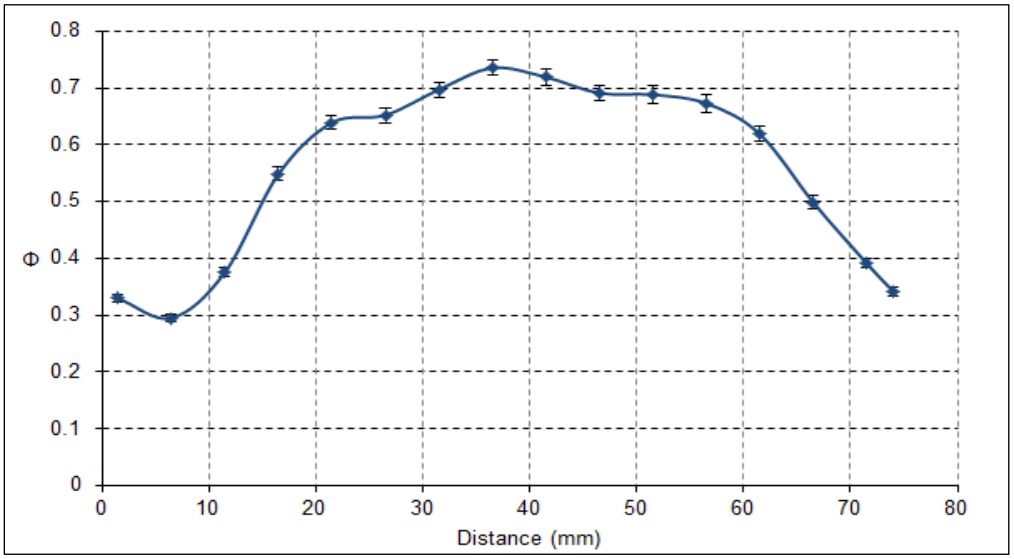

Figure 2.5: Transverse fuel profile across the test section along the span of the bluff body for flat fueling conditions.

Bulk flow air velocities through the rig were characterized using a particle imaging velocimetry (PIV) system. The PIV setup included a Flow Master CCD camera, New Wave dual cavity Nd:YAG laser with 50 mJ per pulse, and LaVision 7.0 control software. One-micron alumina seed particles were injected through a seeding tube in the mid-span of the mixing section of the rig, supplied from a separate air stream. Sufficiently high particle seeding density within the rig was ensured by manual application of periodic forcing to the seeder tube.

A flow parameter table for conditions that were characterized by PIV in both unvitiated and vitiated experiments is given below (all values are approximate):

Table 2.1: Flow parameters.

	V (m/s)	Mach	Re	T (K)
Unvitiated 0.0625 kg/s	23.5	0.068	14502	300
Unvitiated 0.0720 kg/s	27.8	0.082	17155	300
Unvitiated 0.0865 kg/s	32.3	0.094	19932	300
Vitiated (ϕp=0.17) 0.0625 kg/s	53.0	0.097	6668	735
Vitiated (ϕp=0.17) 0.0865 kg/s	71.0	0.128	8933	765

For vitiated mixtures, viscosity calculations inherent in the Reynolds numbers in Table 2.1 were approximated as [57]:

$$\mu_{mix} = \frac{\sum X_i \mu_i (M_i)^{\frac{1}{2}}}{\sum X_i (M_i)^{\frac{1}{2}}} \tag{2.3}$$

where X_i is the mole fraction of species i, μ_i is dynamic viscosity of species i, and M is molar mass. Only the major species (N_2, O_2, CO_2, and H_2O) were included in the calculation. Equation 2.3 assumes each species is separate and ignores the effect of the interaction of unlike molecules on viscosity, which introduces only negligible error. Reynolds numbers calculated with viscosities from vitiated mixtures increased by only 3-5% over calculations assuming air.

Velocities provided in the table are averaged across two bluff body heights around the center of the duct. Much effort has been put into creating a flat velocity profile through the use of flow straighteners. However, due to the design of the rig, any significant flow straightening must be done upstream of the air foil fuel injectors. Thus, imperfections in the aerodynamic shape of the fuel struts have a prominent effect on the flow distribution at the bluff body. Figure 2.6 shows a comparison of air velocity profiles taken by PIV before and after a perforated aluminum flow straightener was inserted immediately upstream of the fuel injectors. Many flow straightener designs were experimented with, which generally consisted of perforated aluminum sheets, layered to maximize the blockage ratio (Figure 2.7). The effect of this was increased turbulence and enhanced mixing.

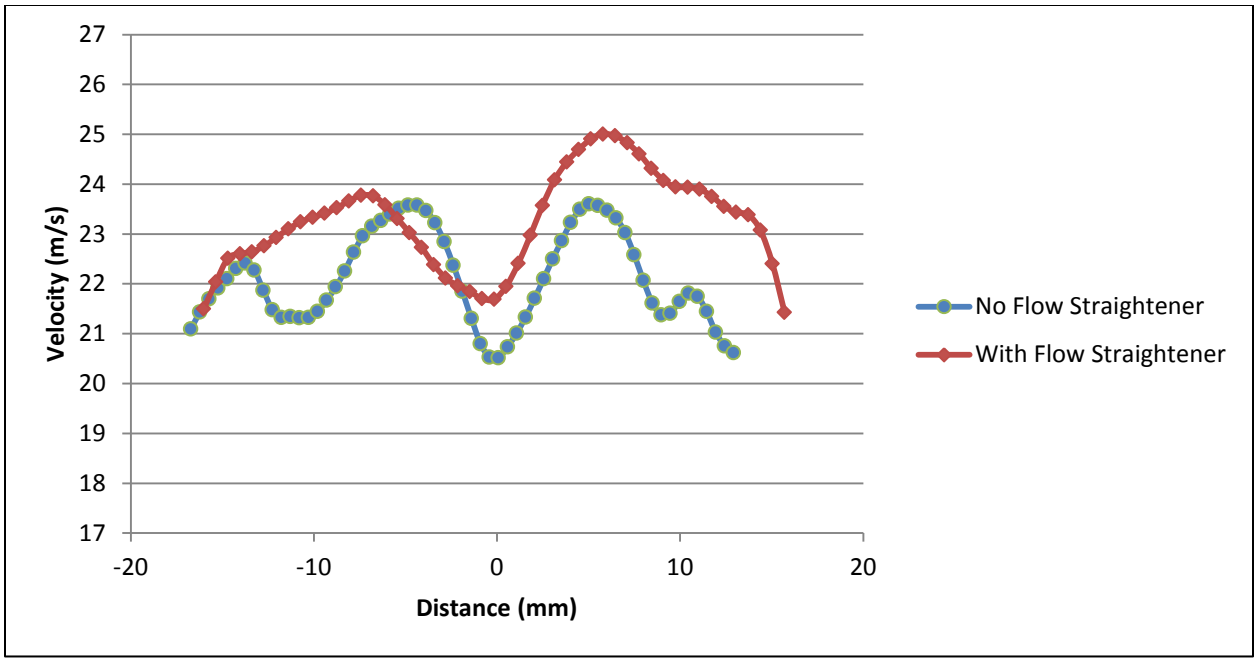

Figure 2.6: Air velocity profiles with and without flow straightener.

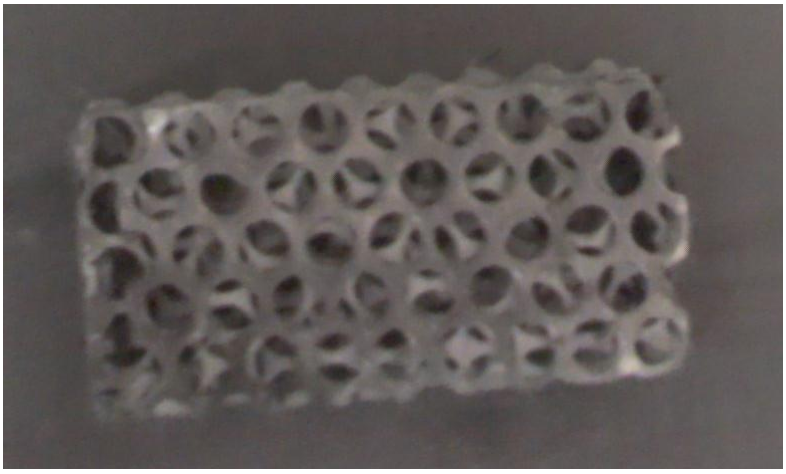

Figure 2.7: Example of a flow straightener tested in the rig.

Figure 2.6 highlights the effects of the airfoils on the flow, as seen by the three evenly spaced dips, as well as the level of improvement that the flow straightener made by mixing out the dips to a degree. The large center dip can also be attributed to the seed injector pipe brazed into the convergent section of the rig. Figure 2.8 and Figure 2.9

show a comparison of vitiated to unvitiated flow and a velocity profile taken with the bluff body in place, respectively.

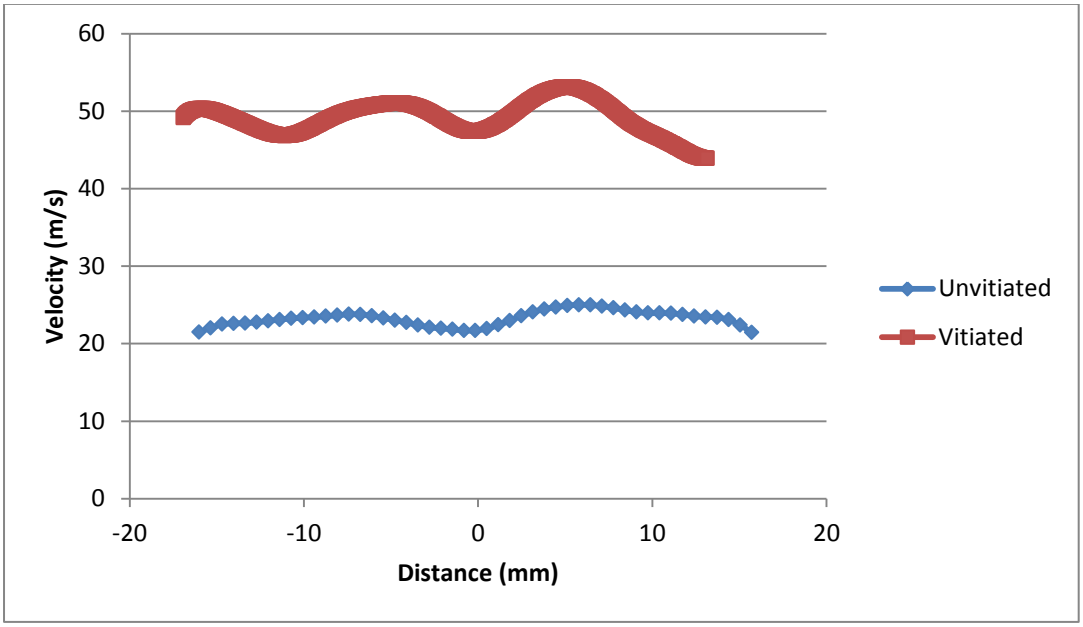

Figure 2.8: Vitiated and non-vitiated velocities

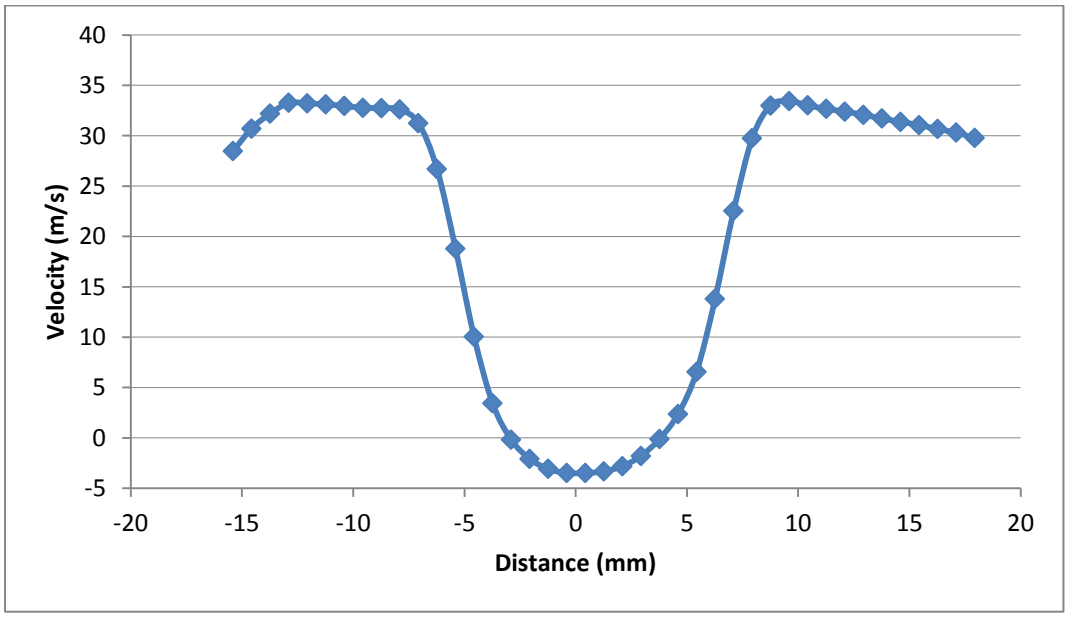

Figure 2.9: Velocity profile with bluff body.

In Figure 2.8, the effects of the fuel struts on the vitiated velocity seem exacerbated as compared to the unvitiated profile. However, for both cases the peak to peak difference around the major dip in the center remains approximately 5% and the peak to trough difference is approximately 10%.

Figure 2.9 shows the velocity profile with the bluff body in place measured just downstream of the bluff body trailing surface. The negative velocity in the region of the bluff body (-4.8 mm to 4.8 mm) indicates the recirculation zone. It is evident that, with the bluff body in place, the undesired structures shown in the previous figures don't appear to survive.

2.3 TDLAS setup

A typical tunable diode laser absorption spectroscopy (TDLAS) setup consists of a tunable diode laser, tuned by the combination of a current controller and a temperature controller, followed by beam shaping optics, an absorbing environment of interest, a detector, and a data acquisition system (Figure 2.10).

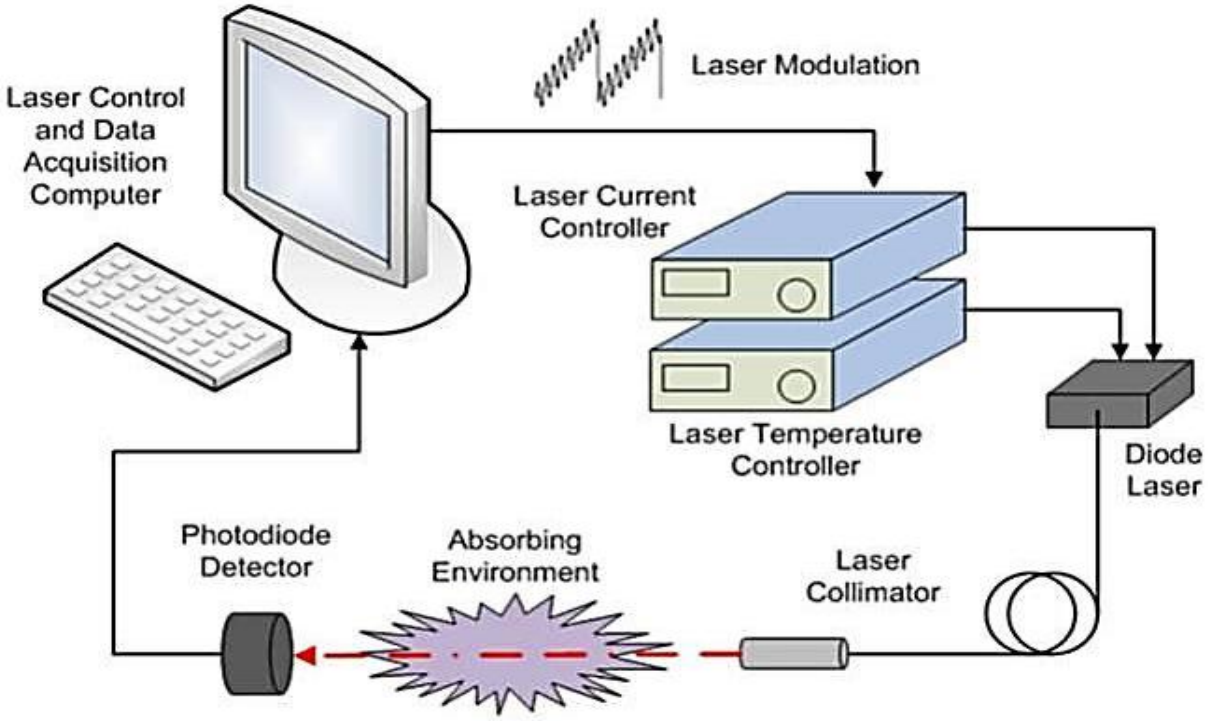

Figure 2.10: TDLAS diagram [58].

The TDLAS application developed in this work used a distributed feedback (DFB) diode laser mounted on a TO5 geometry with an internal thermoelectric cooler (TEC). To convect away heat and allow it to tune properly, the laser was mounted on a finned copper heat sink with a carbon-based thermal compound.

A DFB laser works as the injection current creates a population inversion in the semiconductor band gap. The emitted radiation oscillates in an optical cavity and refracts off of a small diffraction grating. The laser emission wavelength changes with the index of refraction, which is modified by temperature. The temperature is altered both by the TEC and the laser injection current. The TEC affects the temperature of the entire laser system, including the diode, casing, and heat sink, and thus produces slow,

coarse tuning. The injection current generates heat within the laser which dissipates according to the Joule effect, proportional to the square of the current. Since the heat generated from the injection current is localized to the active area of the laser, the wavelength response to changes in the current is much quicker than its response to changes in TEC resistance [59].

The laser used in this study (Nanoplus 525-2753-2) outputs a center wavelength of about 2752.5 nm. The beam passed through an aspheric collimating lens with a focal length of 4 mm, through the absorbing gas, and to a Thorlabs PDA20H PbSe photodetector with a 10kHz bandwidth and a wavelength response from 1.5-4.8 microns. An iris was also used between the detector and the burner to pass the laser beam and decrease unwanted infrared emissions from the flame. To aid in the alignment process, the laser was affixed to three separate translation stages: two for positioning and one for focus, as shown in Fig. 2.11.

For calibration purposes, a 2-inch, stainless steel McKenna Flat Flame Burner was used to produce a uniform column of combustion products, with CO_2 acting as the absorption gas of interest. The beam passed over the burner within a millimeter of the surface to minimize the effects of the ambient air on the temperature of the combustion gases of interest.

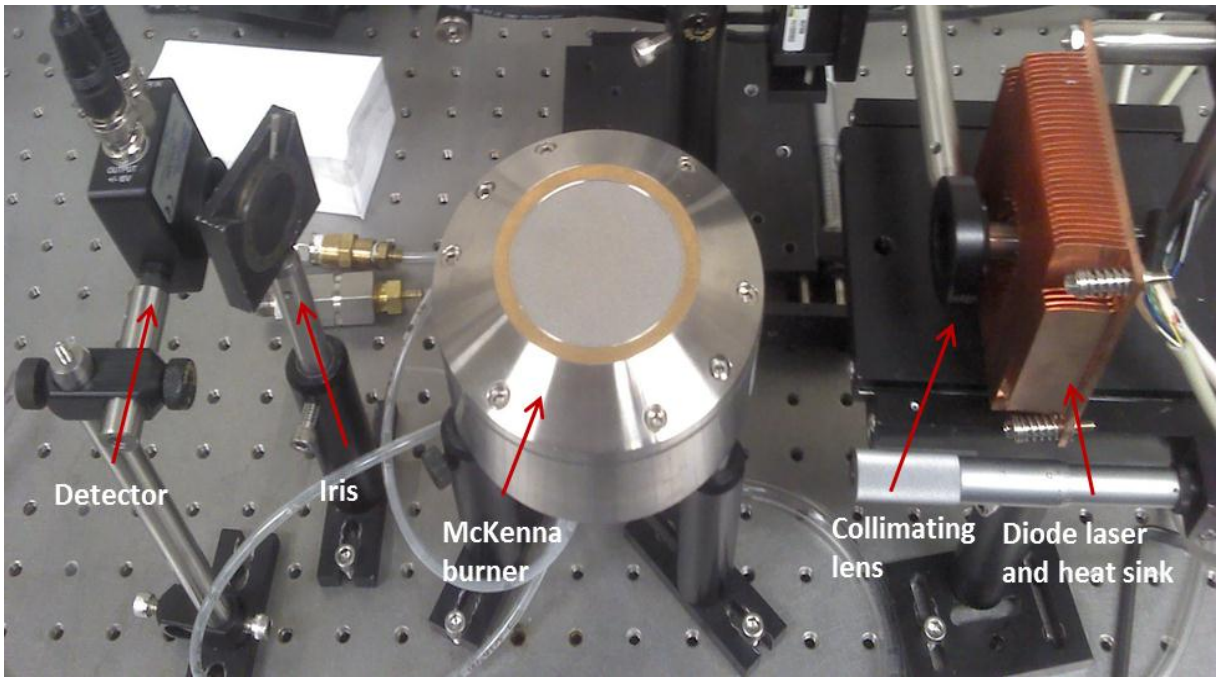

Figure 2.11: TDLAS calibration setup.

To produce the desired wavelengths, a National Instruments LabVIEW program created a triangular voltage ramp that was used as an input to a Thorlabs LDC 500 current controller through a DAQ board. With the coarse-tuning laser temperature held constant, the fine-tuning current scanned the laser wavelength across the spectral absorption lines of interest. As this occurs, a percentage of the laser light is absorbed according to the Beer-Lambert law and the signal to the detector is diminished. Figure 2.12 shows a raw input ramp of 10,000 samples with the output signal from the detector.

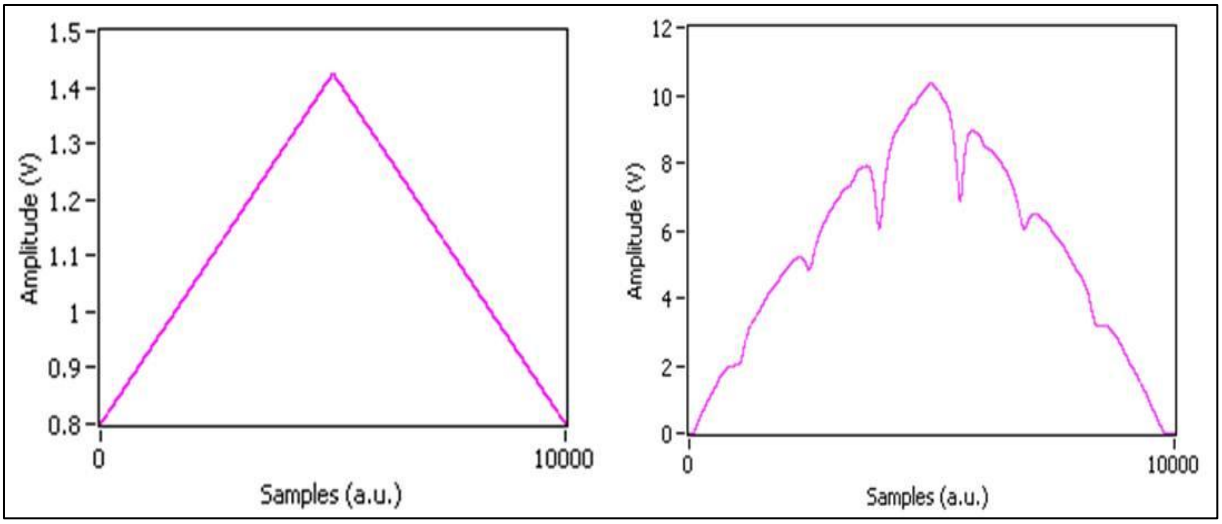

Figure 2.12: Input voltage ramp (left) and detector output with absorption (right)

Clear absorption is seen from the detector signal as the wavelength is scanned across particular absorption lines. The voltage ramp is offset by 0.8V due to a minimum response voltage of the laser which varied at different wavelengths.

3 Flame Blowoff Analysis

3.1 Blowoff Equivalence Ratio Data

Large data sets of flame blowoff equivalence ratios were compiled for rig characterization and to examine trends in the blowoff curves. The blowoff curves for various fueling gradients versus Reynolds number are shown below.

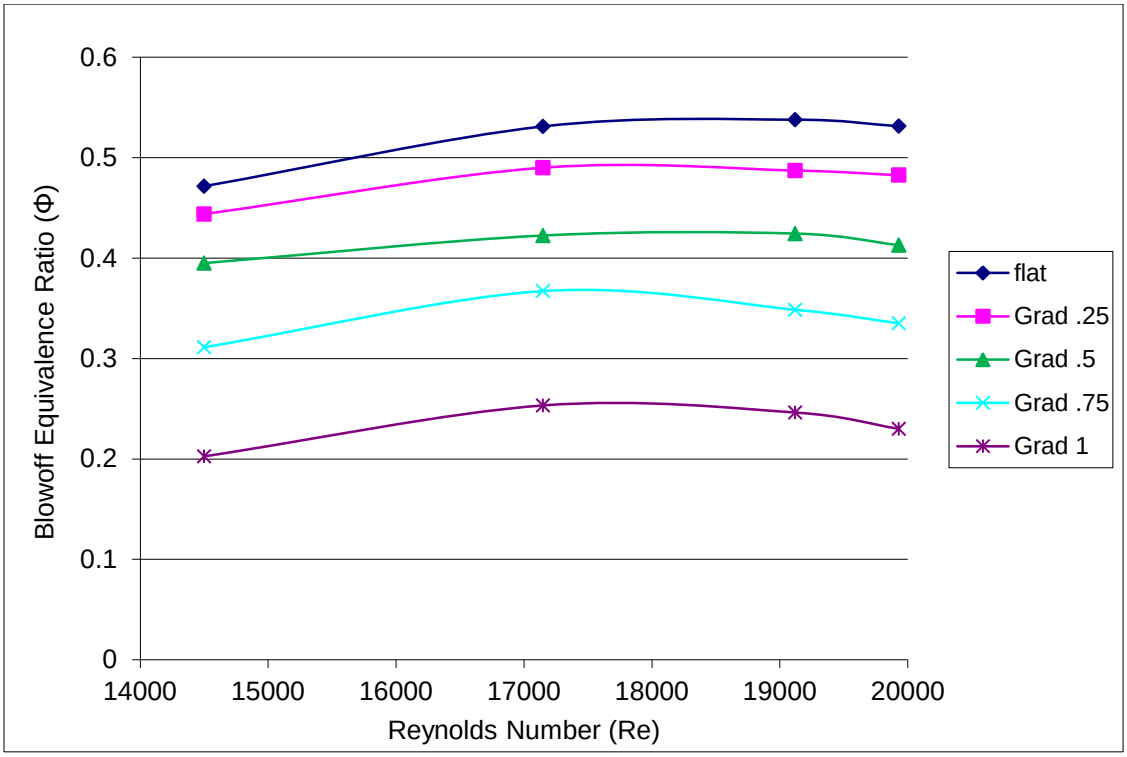

Figure 3.1: Blowoff equivalence ratios as a function of Reynolds number for different upstream fuel profiles.

The equivalence ratios reported in Figure 3.1 represent the equivalence ratios of the mixture around the center fuel strut. In the flat case, this is also the equivalence ratio around all fuel struts, but for the gradient cases, the fueling outside the center channel follows the schema outlined in section 2.2 of this thesis.

The general upward trend with increasing Reynolds number is expected, as increased velocity induces increased strain on the flame sheet, which is a major precursor to the blowoff process. The equivalence ratios shown in Figure 3.1 are total injected equivalence ratios across the entire test section, not what is present around the bluff body. This can be misleading in the asymmetrically-fueled cases. As was shown from the gas analyzer results in Fig. 2.3, for a given injected equivalence ratio, the actual equivalence ratio across the bluff body is significantly increased with increasing fuel gradient.

To obtain a more accurate picture of actual blowoff points, fuel profiles for each gradient case were characterized at multiple injection equivalence ratios. Data was interpolated between these points to project profiles for any desired equivalence ratio. Using this interpolation, the fuel profiles for each gradient case were compared at their respective blowoff points. The result is shown in Figure 3.2.

Clearly, the lean sides of the profiles differ by a significant amount, but the rich regions are nearly identical in each case. This makes sense, as it is primarily the physics of the richer shear layer which will govern blowoff in the large gradient cases. This is because the lean side equivalence ratio is below the lean limit for these flames and any burning is being piloted by the rich side. Thus, when the rich shear layer blows out, the entire flame will extinguish.

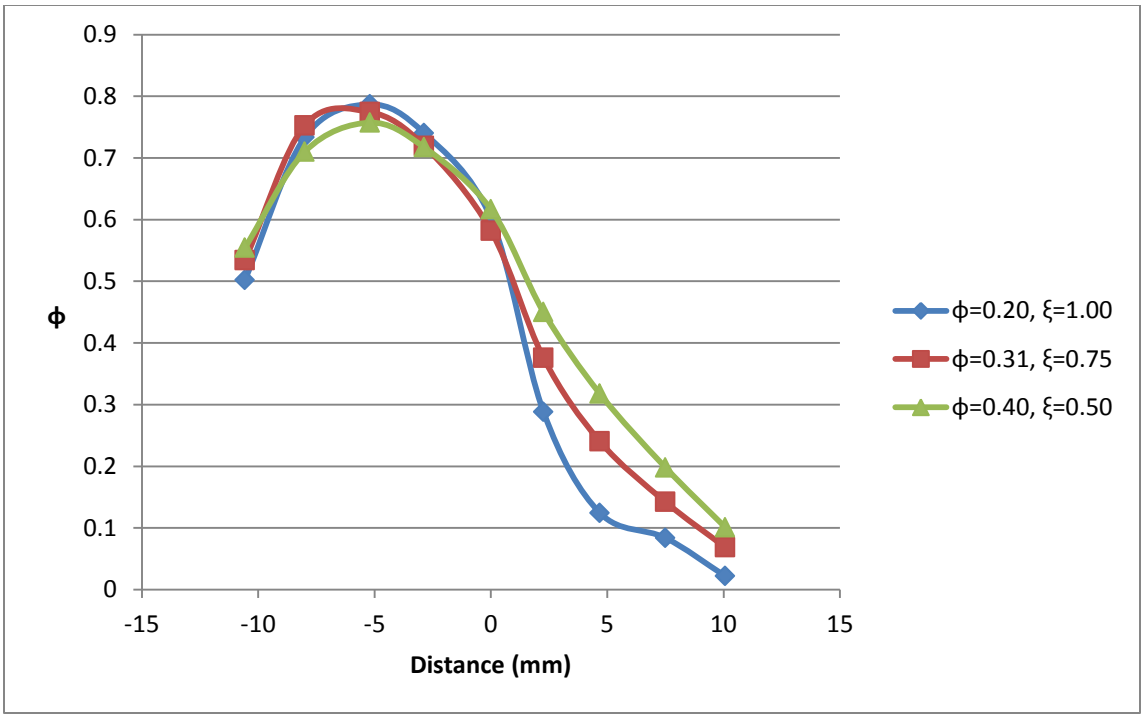

Figure 3.2: Fuel profiles near blowoff.

3.2 Transverse effects

The transverse fuel profile from Fig. 2.4 is highly symmetric with a bump in the center which reflects the presence of the upstream seeder tube. Simultaneous high speed videos were taken of the top and side views of the flame using the two-Phantom camera setup at 5000 fps. These were analyzed together to examine any three-dimensional effects on the flame near blowoff. When the flame is relatively stable, the top images show that the flame is largely two-dimensional (see Figure 3.3).

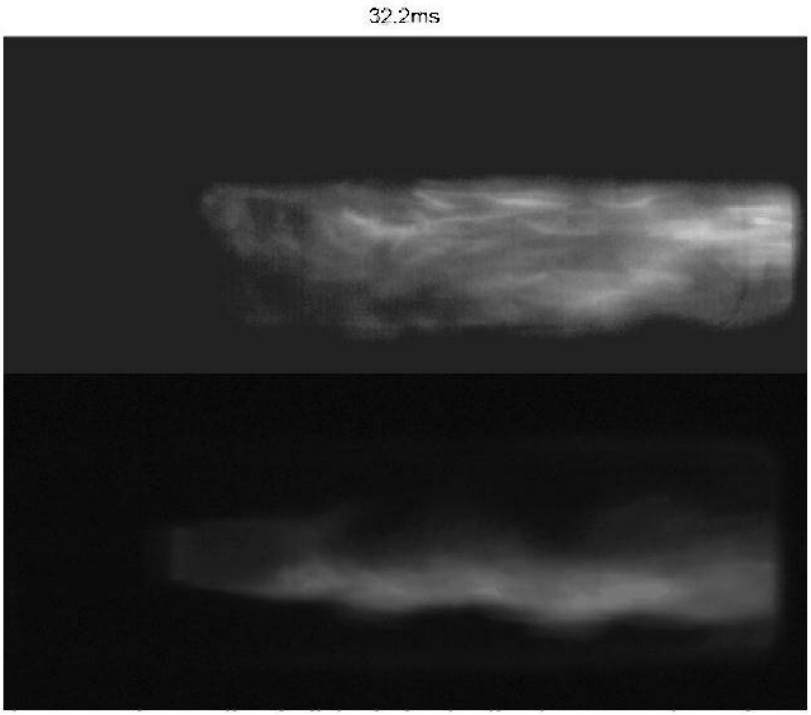

Figure 3.3: Instantaneous chemiluminescence image. Top image is top view of flame, bottom image is side view. Timer is countdown to blowoff.

However, when the flame approaches blowoff and Von Kármán vortices more heavily dominate the flame structure, the three-dimensionality of the flame becomes more apparent. Figure 3.4 shows a series of 9 consecutive images of the top and side views of the flame near blowoff.

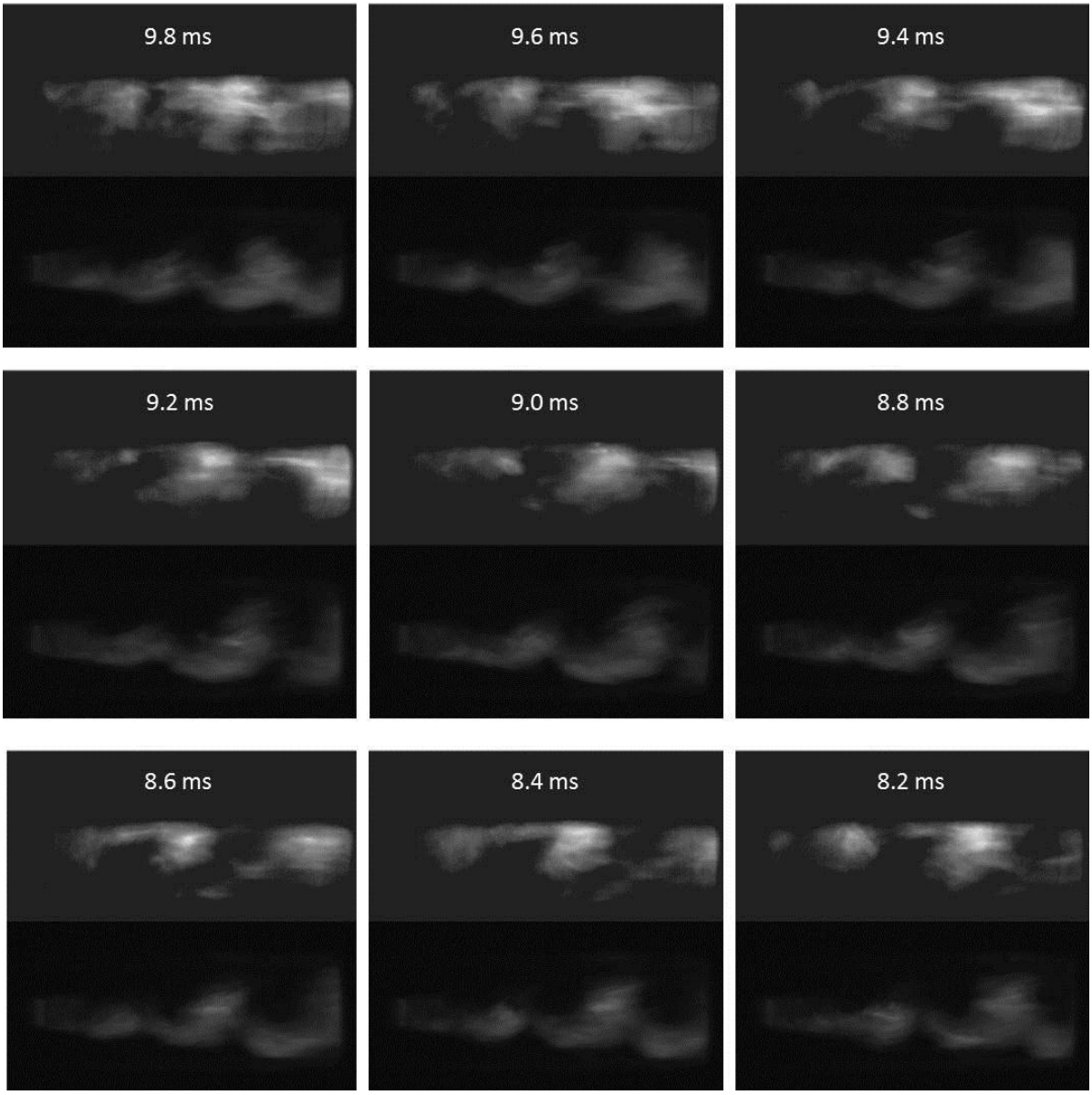

Figure 3.4: Top and side views of the flame chemiluminescence as it approaches blowoff.

It can be seen in Figure 3.4 that immediately downstream of many of the advecting vortices, the flame pinches off, leaving holes in the flame sheet. The topside view of this behavior shows that in some instances it is only a partial pinching. That is, the flame extinguishes and pulls in on one side, while remaining intact on the other.

It was noticed that a gap existed between the bluff body and the quartz window on the order of hundreds of microns. Such a gap would allow air to pass by the end of the bluff body and pull into the flame, weakening it on the side shown from the frames above. The transverse asymmetries can be an effect of this, in combination with slightly uneven fuel distributions and potential three-dimensional behavior of the vortices. In an attempt to weaken these effects, a small triangular piece of graphite gasket was affixed to the end of the bluff body to ensure closure of the small gap. This made the flame visibly more uniform spanwise across the bluff body.

3.3 Proper Orthogonal Decomposition of Flame Images

To achieve a more quantitative analysis of the high-speed videos, proper orthogonal decomposition (POD) algorithms were employed. POD is a statistical method used to reduce large data sets down to their most prominent spatial features, hereafter referred to as modes. Much like Fourier decomposition, these modes are orthogonal bases which can combine to exactly recreate the original data. Unlike Fourier decomposition, however, these modes are not restricted to sine and cosine functions, but are selected mathematically to best fit the data they represent [59].

The original data set is described by the equation:

$$OD_i^t \approx \sum_{j=1}^{M} a_i^t v_j^i \tag{3.1}$$

where *OD* is the original data or images, *i* is the pixel count, *t* is the time step, *j* is the mode number, v_j^i are the spatial modes, and a_i^t are the temporal weighting coefficients [60].

Numerous "snapshot" images are selected from a given chemiluminescence movie to represent the data set as a whole. The modes are then extracted by calculation of the eigenvectors of the covariance matrix from this reduced data set. The modes are prioritized by repositioning the eigenvectors in descending order according to the largest eigenvalues. This technique was first applied to turbulent flows by Lumley [61], and has since found application in many other combustion-related fields [62-64].

A preliminary POD analysis was done on the high-speed videos (5000 fps) from the Phantom camera. Vitiated conditions were run at two different fuel gradient cases (ξ=0.50, ξ=1.00). Limited data sets of one video per case were available for this initial study. Roughly thirty snapshot images were taken from the frames of both videos to form the POD mode shapes. The 30 snapshot images were selected to represent the large variety of patterns the flame exhibits, providing representation for a strongly burning flame, a vortex-dominated flame, the flame at blowoff, and transitions between these states. From these snapshot images, nine mode shapes were extracted, representing the ability to reconstruct any of the flame images with 98% accuracy. Figure 3.5 shows three original false-color images next to their POD-reconstructed counterparts.

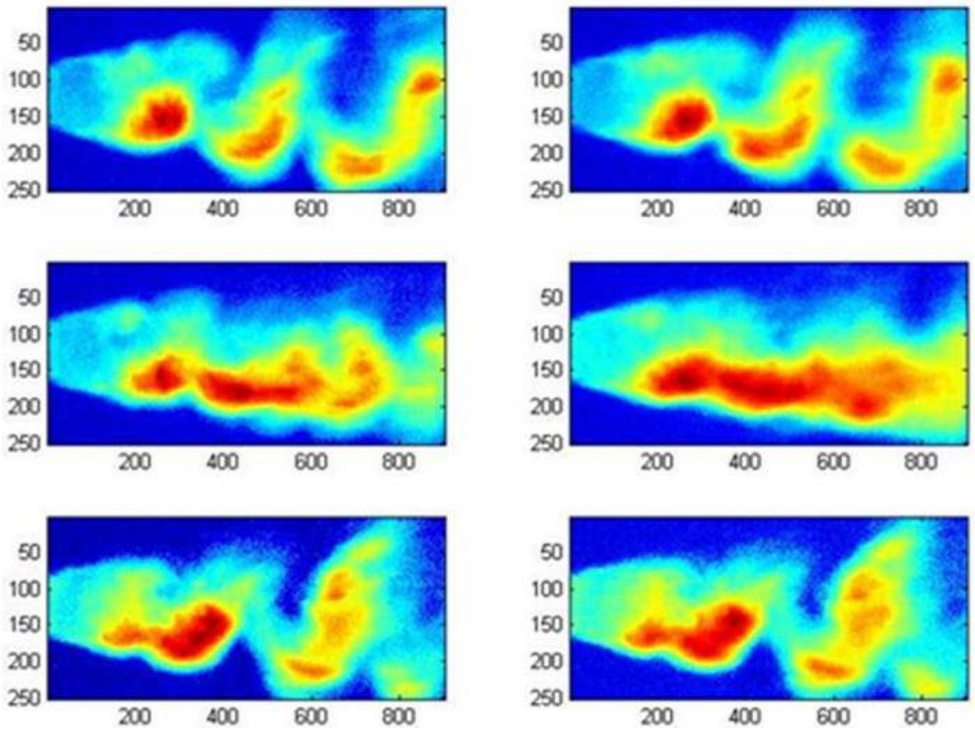

Figure 3.5: Original (left column) and reconstructed (right column) images.

The reconstructed data is a good representation of the original images, but still fails to capture some of the finer structures, as is most apparent in the middle set of images.

This comparison is useful in understanding the level of completeness of the number and content of the extracted mode shapes. However, it is uninteresting from the perspective that the purpose of the POD analysis is not to reconstruct the flame, but to quantify its dynamic phases, particularly at blowoff. Thus, a visual examination of the POD mode shapes is telling. The nine modes shapes from the initial vitiated flames are shown in Figure 3.6.

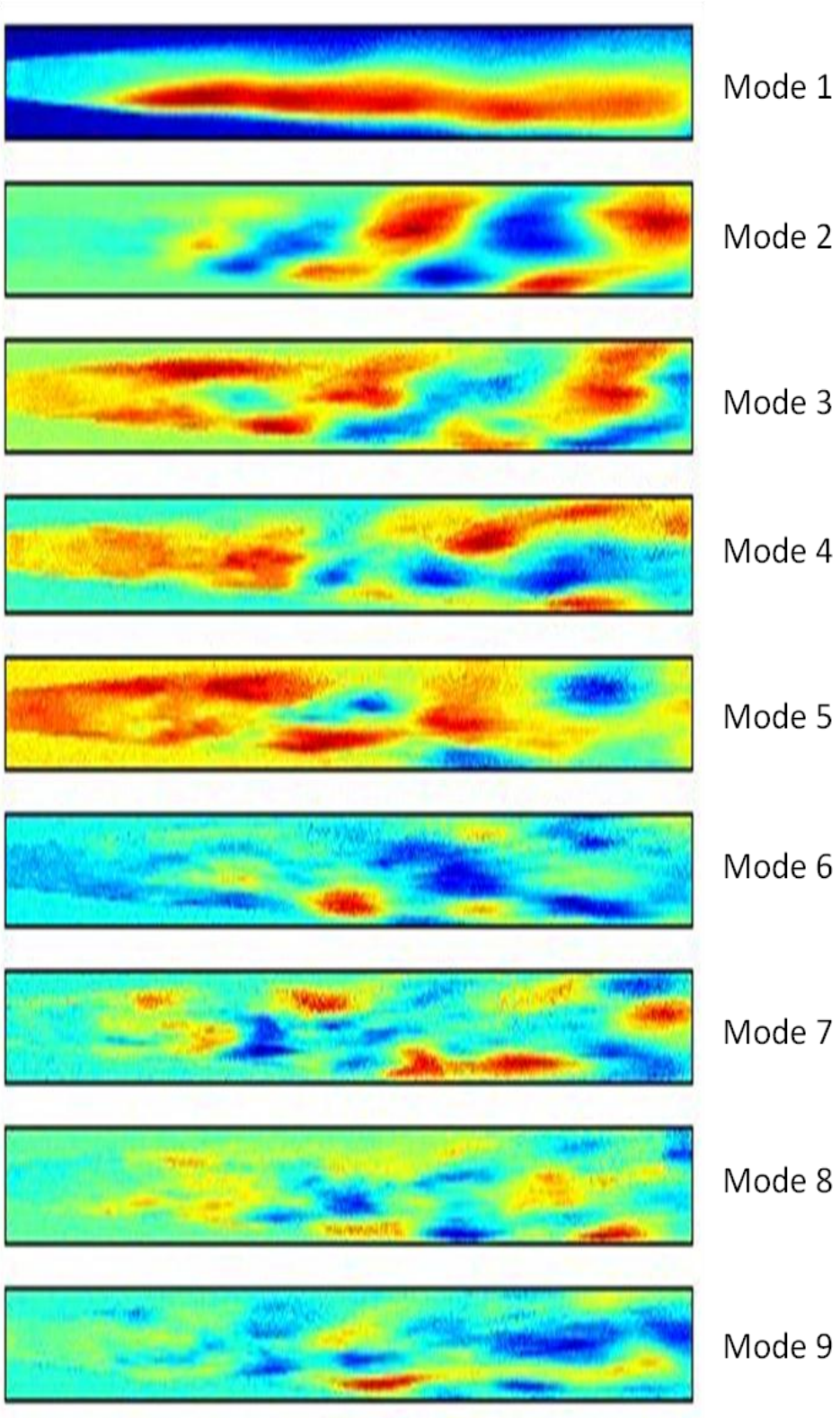

Figure 3.6: POD mode shapes computed from 30 Phantom camera snapshot images.

The first mode, as is mathematically expected, depicts approximately the time-averaged flame. The single strongly-burning shear layer in this mode is representative of the asymmetrically-fueled flames. The second mode displays a clear pattern of alternating vortices. The weighting constants multiplied by the mode shapes in reconstructing the flame images can be positive or negative. This allows for the intense red regions and weak blue regions of the image to alternate in adding to or subtracting from the reconstruction. The third and fifth modes also show the presence of Von Kármán vortices, downstream of strongly-burning shear layers. The fourth mode displays strain-induced flame pinching in the mid-field of the flame. The higher modes handle higher frequency perturbations in the flame and are difficult to associate with any specific physical behavior.

A fast Fourier transform (FFT) was applied to the mode constants to determine frequencies at which these modes become more or less pertinent to the total flame structure. While some of the modes show no characteristic frequency, many of them, including the vortex-dominated second mode, revealed a single broad frequency peak at about 1300 Hz. This data was compared with an FFT of the data measured from the pressure transducer, which also showed a frequency peak at about 1300 Hz (see Figure 3.7). This frequency corresponded to a Strouhal number of 0.23, which is known to be associated with von Kármán vortex shedding. This is in good agreement with previous findings [65].

It is also observed that the other pertinent acoustic frequencies seen in the pressure trace, such as the peaks at 192Hz and 650Hz, are not reproduced in the FFT of the POD constants. This suggests that any acoustic-flame coupling at these frequencies is relatively weak. This will be explored further subsequently.

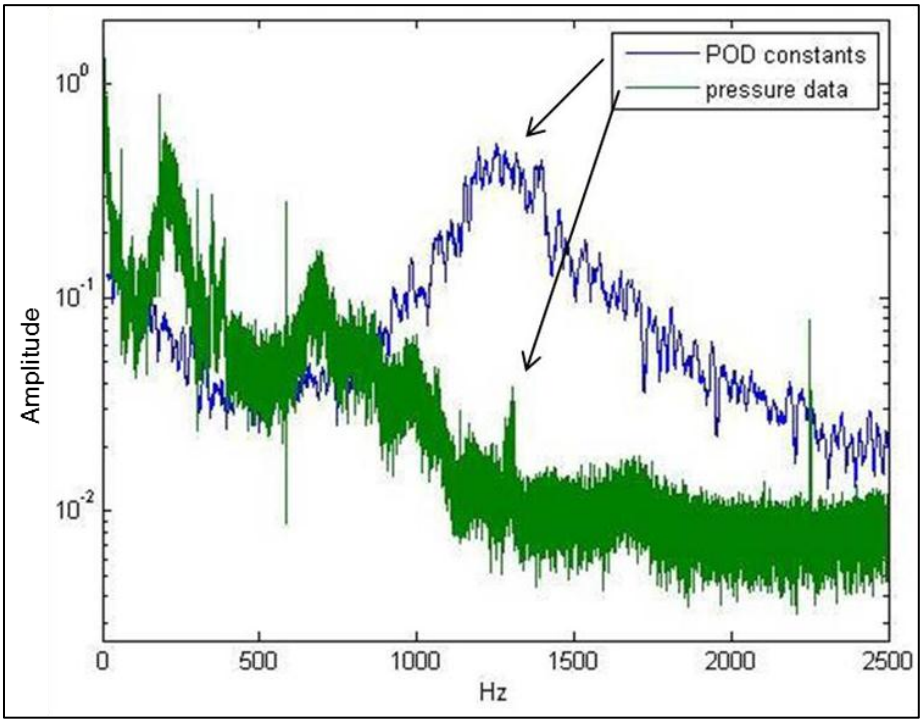

Figure 3.7: FFT's of POD mode constants and pressure

Statistical mode energies were examined to understand the strength of each mode as the flame approaches blowoff. These energies were calculated according to the following equation:

$$E(i,j) = \frac{\left|var\left(PC(i,j)\right)\right|}{\left|var(RD(j))\right|} \tag{3.2}$$

where *i* is the mode, *j* is the time step, *var()* is the variance, *PC* is the principal component, and *RD* is the reduced data (constructed from all modes). This type of

statistical energy reveals the percent contribution of each mode to the total flame reconstruction in time.

Figure 3.8 shows a normalized plot of the mode constants in the 0.50 fuel gradient case for modes 1, 2, and 4 over time, leading up to blowoff.

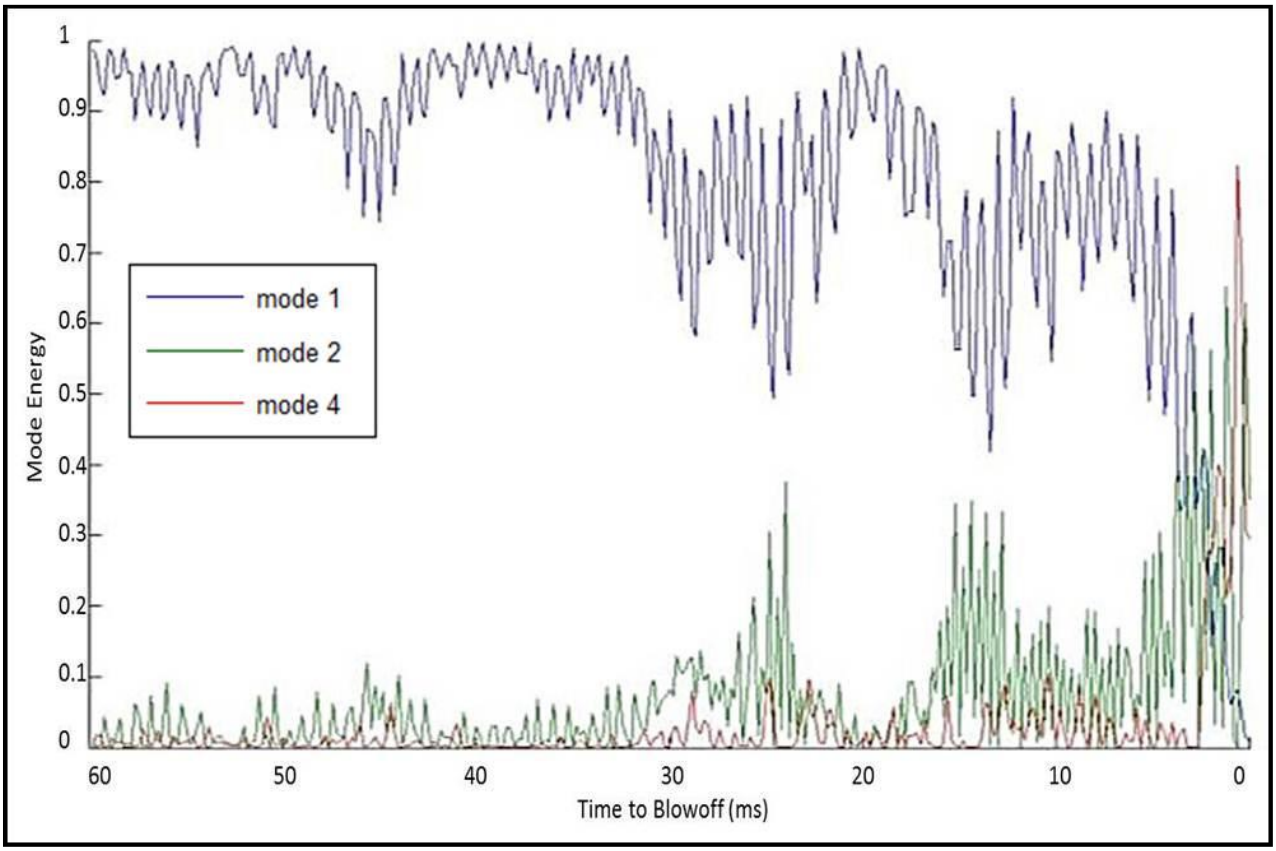

Figure 3.8: Mode energies through blowoff.

It is shown in Fig. 3.8 that while the flames are strongly burning, the first mode, or flame average, accounts for at least 90% of the image decomposition energy. Decreases in the strength of the first mode indicated deviations from the flame average. As the energy of the first mode decreases, other mode energies necessarily increase, indicating the onset of more dynamic pre-blowoff behavior.

The large dips in first mode energy that begin approximately 30 ms prior to blowoff are mirrored by increases in the second mode energy. Recall from Figure 3.6 that the second mode represents a strong Von Kármán vortex street. Thus, at these points, the strongly-burning single shear layer becomes deformed by the absolute instabilities shedding from the bluff body. This is an indication of weakened heat release in the flame, which drives the dilatation ratio lower and gives way to increased vorticity.

Figure 3.8 shows that the flame average then recovers and the vortices retreat. This cycle repeats with the subsequent spikes in vortex behavior increasing in duration and the flame average recoveries decreasing in magnitude until the final blowoff sequence is initiated. This occurs when the magnitude of the second mode energy becomes sufficiently strong such that it overtakes the first mode energy, indicating that the flame structure is now truly dominated by the vortices.

An interesting conclusion is drawn by examination of the fourth mode energy. Throughout the initial oscillations between the energies of the flame-averaged first mode and the vorticity-dominated second mode, the flame-pinching fourth mode remains relatively unaffected. In the final milliseconds before total flame extinction, however, the fourth mode energy spikes and overtakes all other modes. This suggests that when the magnitude of the Von Kármán vortices is sufficiently high, the local strain on the flame at certain points will exceed the extinction strain rate. This causes the flame to extinguish at a point and pinch off, which shortly precedes final blowoff. This

dynamic series of events shown quantitatively by the POD analysis, can be seen visually in the flame chemiluminescence from the selection of frames in Figure 3.9.

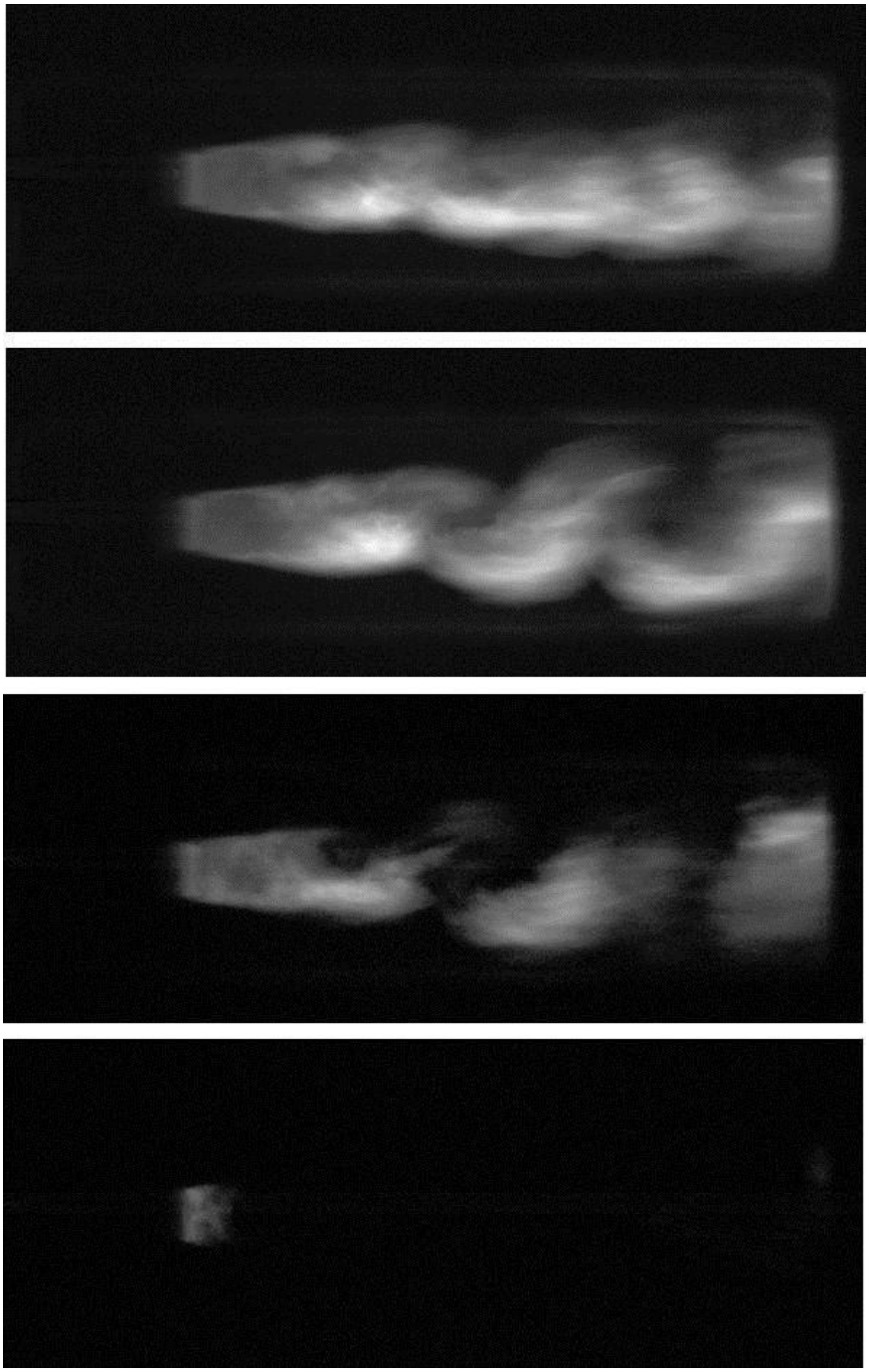

Figure 3.9: Prominent flame dynamics prior to blowoff. From top to bottom - strongly burning flame, vortex-dominated flame, pinched flame, blowoff.

The POD modes show that the flame pinching in these vitiated experiments is occurring further downstream than what has been observed in unvitiated cases [66]. A comparison is shown in Figure 3.10.

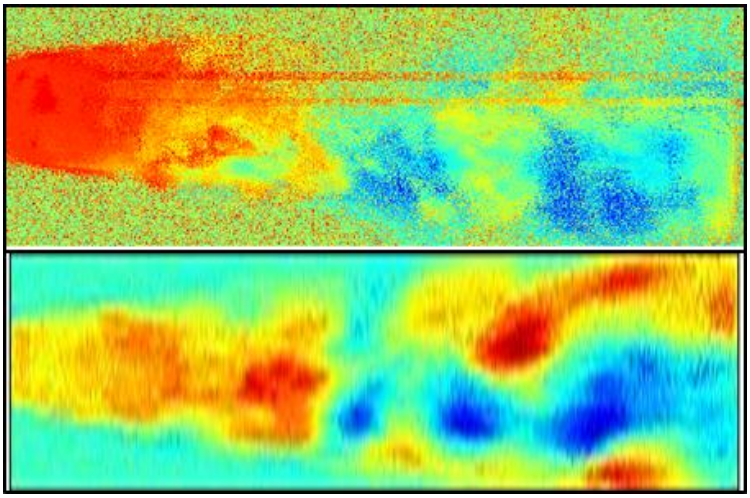

Figure 3.10: Unvitiated flame retreat with recirculation zone burning (top) versus vitiated flame pinching (bottom).

In unvitiated flames, local extinction in the near field of the flame can cause vortices to entrain cold reactants into the recirculation zone, which cools the hot products used to ignite the shear layers. This can also cause burning in the recirculation zone which further contributes to the blowoff process [67]. In the vitiated case presented above, however, no isolated recirculation zone burning is represented in the POD mode shapes. This can be explained by the observation that the flame pinching occurs sufficiently far downstream of the recirculation zone such that it does not entrain cold reactants, as in the unvitiated cases.

These are interesting observations, but they shed light on some of the imperfections and inadequacies of the method that led to them. At this point, it is uncertain whether

the lack of recirculation zone burning in the vitiated flames is due to the vitiation effects or to the limited study of highly-stratified fuel profiles. Also, the POD mode shapes were derived from approximately thirty images from a single data set of each type of flame. This may not be enough to isolate every small-time scale behavior of interest in the flame.

3.4 Statistical Analysis

Although this analysis has been termed preliminary, there is still useful data that can be gleaned from it. The mode energy plot reveals three basic regimes of the flame:

1. The steady regime where time-averaged behavior dominates.
2. The transition to blowoff, which is signaled by the onset of more dynamic flame behavior, beginning approximately 30 ms prior to extinction.
3. The final blowoff sequence, occurring during the last 10 ms up to extinction.

Computational memory limitations prohibit the use of every frame as a snapshot image in the POD mode extraction. These flame regimes help to identify where in time to concentrate the snapshot images for POD calculations.

For the next analysis, a more complete set of data was taken. Using the Photron camera setup, multiple videos of each flame case were taken at 10,000 fps. Selection of the snapshot images for POD mode determination in these cases was based on the aforementioned flame regimes, according to the following algorithm:

1. Every frame in the blowoff regime (last 10 ms).

2. Every third frame in the transition regime (from 10 – 30 ms before extinction).
3. Every fifth frame in the steady regime (from 30 – 70 ms before extinction).

The same snapshot image selection process was used for each of multiple videos per flame case, resulting in approximately 250 images per video. While multiple data sets can offer more statistically conclusive results, they can also pose computational problems, requiring greater amounts of memory to handle the large matrix multiplication operations needed in these calculations. Thus, it becomes important to include in the calculation only the minimum number of data sets required to obtain a statistically converged solution.

To examine how many data sets (videos) needed to be included in the analysis, multiple POD mode sets were extracted from a series of symmetrically-fueled flame cases. Mode shapes were taken using a single data set (250 total images), and then retaken using two data sets (500 total images), three sets (750 total images), and so forth. Correlation coefficients of the resultant mode shapes were calculated according to [68]:

$$r = \frac{\sum_m \sum_n (A_{mn} - \bar{A})(B_{mn} - \bar{B})}{\sqrt{[\sum_m \sum_n (A_{mn} - \bar{A})^2][\sum_m \sum_n (B_{mn} - \bar{B})^2]}} \tag{3.3}$$

where *r* is the correlation coefficient, *A* and *B* are the images being correlated, and *m* and *n* are pixels. The modes from the one-video set were correlated to the modes from the two-video set, and the two-video set to the three-video set, and so forth. The purpose of this was to examine, quantitatively, how much the mode shapes change with

the inclusion of additional data sets. The result of this analysis for the first ten modes is shown in Figure 3.11.

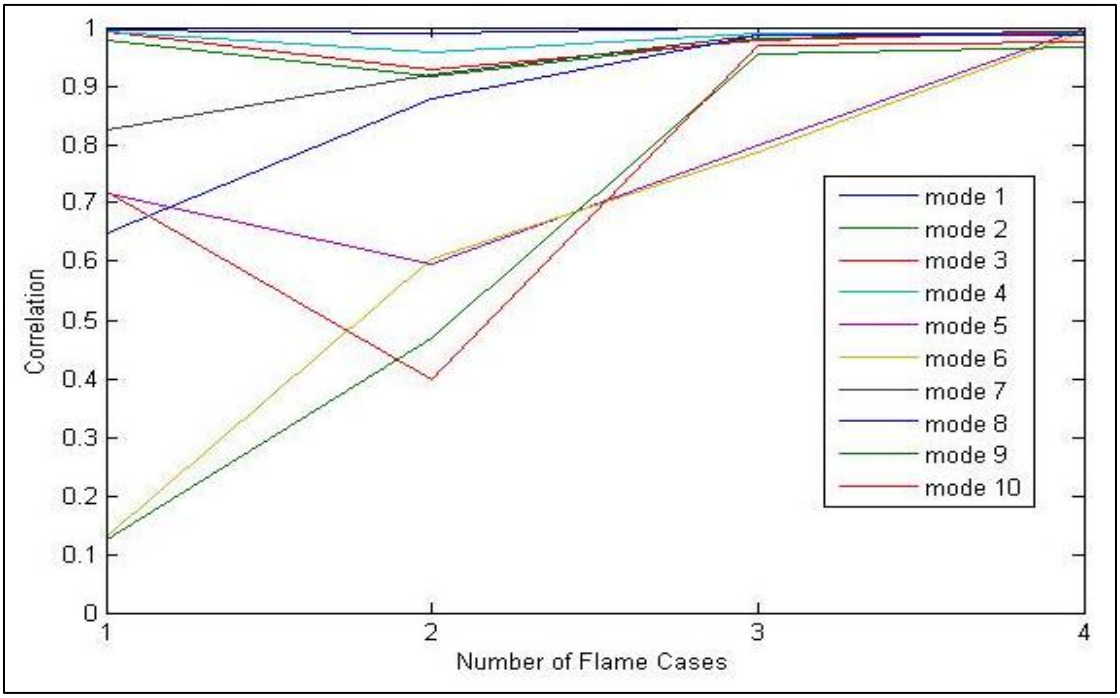

Figure 3.11: Absolute value of the mode shape correlation coefficients.

The x-axis in this plot denotes number of flame cases used in the analysis. Each mode extracted from a given number of videos was correlated with the corresponding mode from the set taken from one additional video. Hence, the correlation at the first point on the plot is between mode shapes from one and two data sets, the second point is between mode shapes from two and three data sets, and so forth.

An autocorrelation domain is [-1,1], where a value of 1 signifies perfect correlation between the data sets, a value of 0 signifies no correlation, and -1 signifies negative correlation. In the case of POD modes, the weighting coefficients that are multiplied by the mode shapes to reconstruct the original data can be positive or negative. That is, in

recreating the original data, the mode shape images can either constructively add to the total reconstruction or destructively take from it. Hence, negatively correlated modes could in reality be positively correlated with a sign change in their weighting coefficients. For this reason, the absolute values of the autocorrelation results are shown in Figure 3.11.

The plot reveals that the correlations of all the mode shapes converge approximately to unity by the fourth data set. That is, by including a fifth video, the mode shapes did not change from what they were with only four videos. Thus, the combined information from four data sets is concluded to accurately represent the dynamics of their particular configuration.

3.5 Analysis of symmetrically-fueled cases

Following the results of the statistical analysis above, a total of 1000 snapshot images taken from four data sets of symmetrically-fueled flames were employed to extract POD mode shapes. The first ten modes are shown in Figure 3.12.

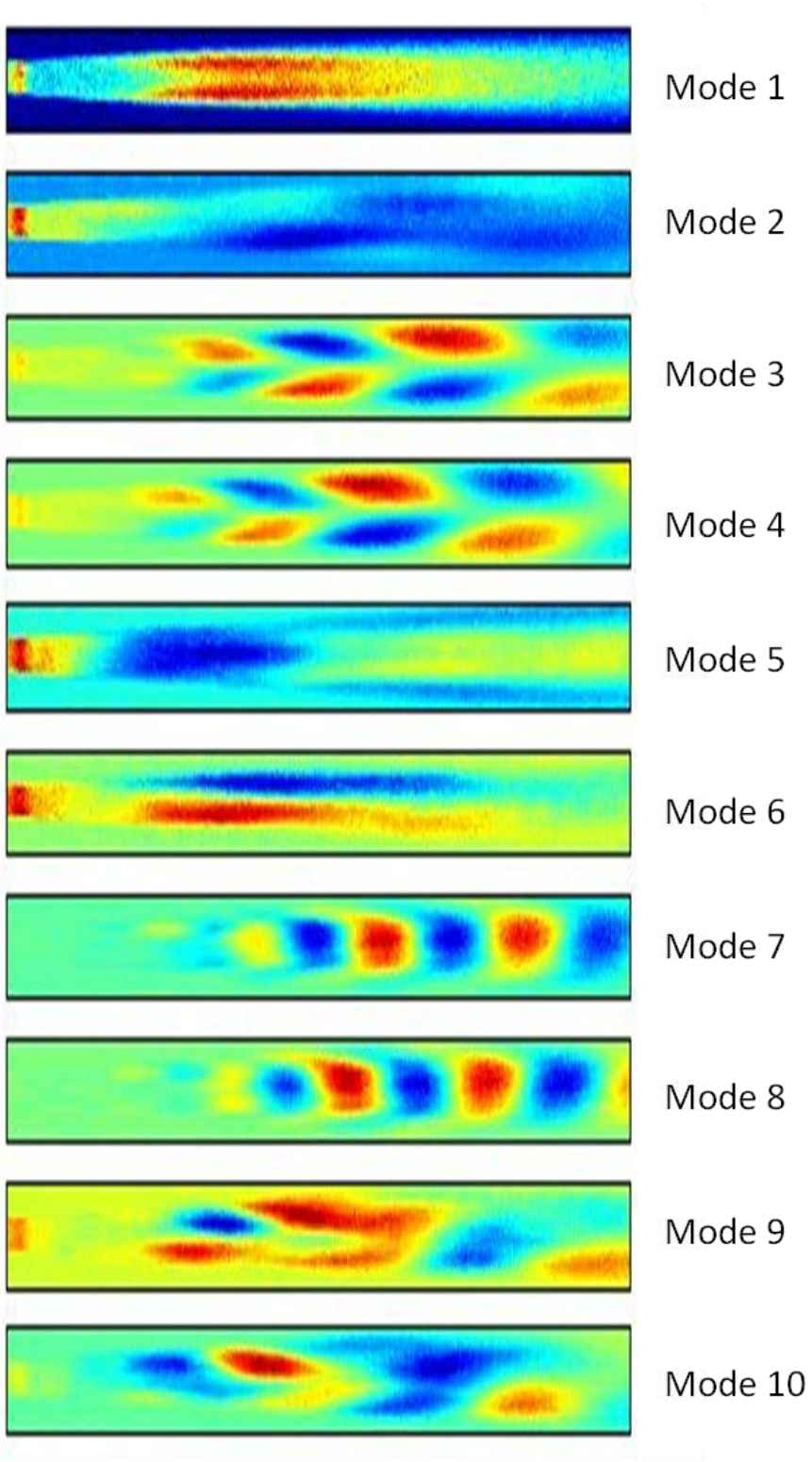

Figure 3.12: POD modes for the flat-fueled flames.

As expected, the first mode again represents approximately the time-averaged flame, with two symmetric shear layers. Also, consistent with the preliminary analysis, a strong vortex-shedding presence is apparent in some of the modes. However, in this case, modes 3 and 4 both display vortex shedding, spatially out of phase with each other. This allows for reconstruction of the vortex advection.

Mode energy plots were constructed for these symmetric flames in the same manner as discussed previously. One example is given in Figure 3.13.

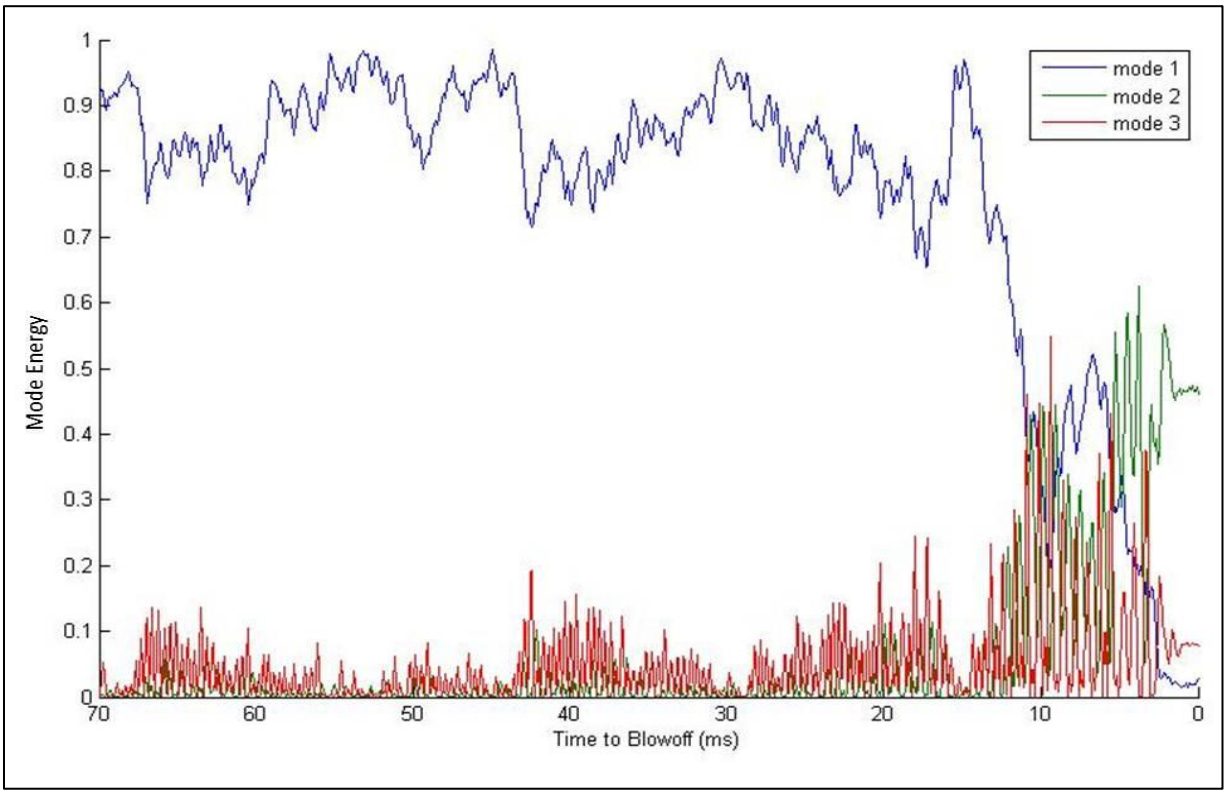

Figure 3.13: Energy constants for first three POD modes of a flat flame case.

Figure 3.13 gives a similar picture to that shown from the preliminary analysis in Fig. 3.8, but a more detailed look reveals some interesting features. Again, the first mode

dominates when the flame is stable, while minor recesses in this mode's energy are mirrored by increases in the vortex-shedding third mode energy.

The fourth mode energy follows that of the third mode and has been left off of this figure for clarity. However, as it visually serves as a compliment to the third mode, we expect that the mode energy will do the same; and indeed it does. A magnified view of the third and fourth mode energies reveals that, not only are these modes spatially offset from each other, but they are temporally out of phase as well (see Figure 3.14). Again, this beating of the modes against each other is necessary to reproduce the downstream advection of the vortices.

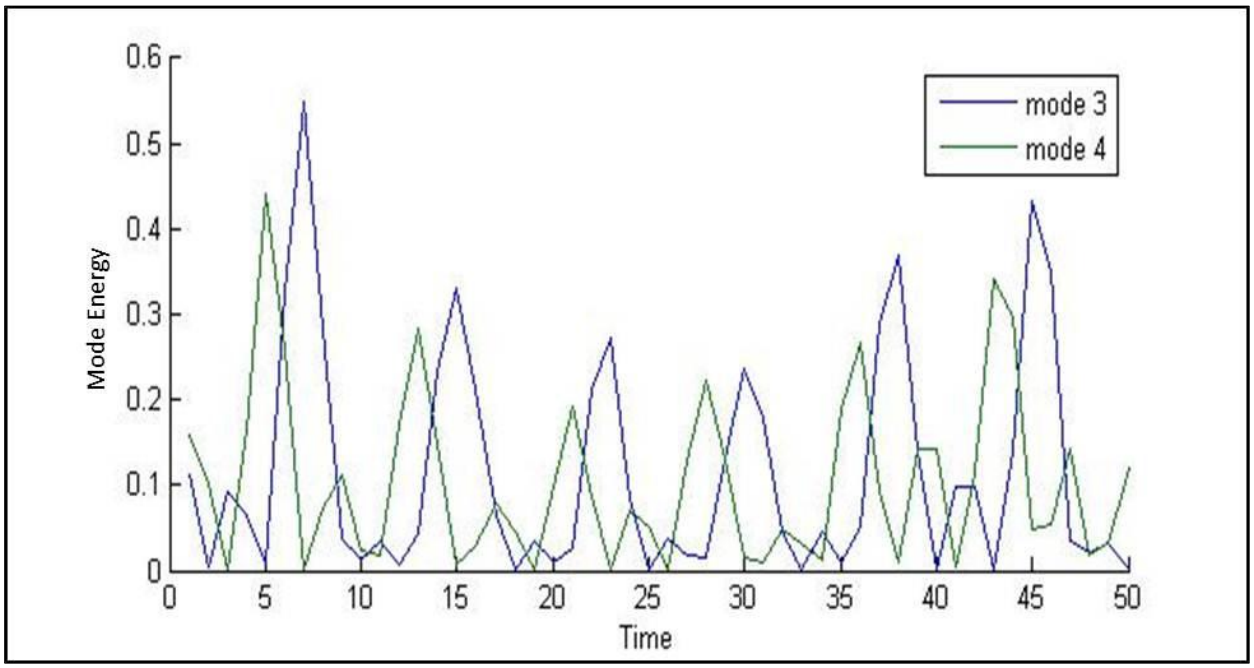

Figure 3.14: Energies of vortex modes.

Returning to Figure 3.13, the final blowoff sequence initiates at approximately 15 ms prior to blowoff. Vortex shedding rises sharply, which is followed by a brief recovery of

the stable flame behavior. Finally, the second mode energy surpasses the other modes and blowoff occurs.

This creates interest around the physical behavior of the second mode. It appears to display a relatively weak flame extending to the mid-field of the flow, which suggests it is representative of the strain-induced pinching observed previously. A look at the fifth mode reveals burning immediately downstream of the bluff body within the recirculation zone, with an absence of flame extending out to the point in the mid-field where the second mode flame cuts off. A more complete picture is obtained when comparing the behaviors of modes 2 and 5, as shown in Figure 3.15.

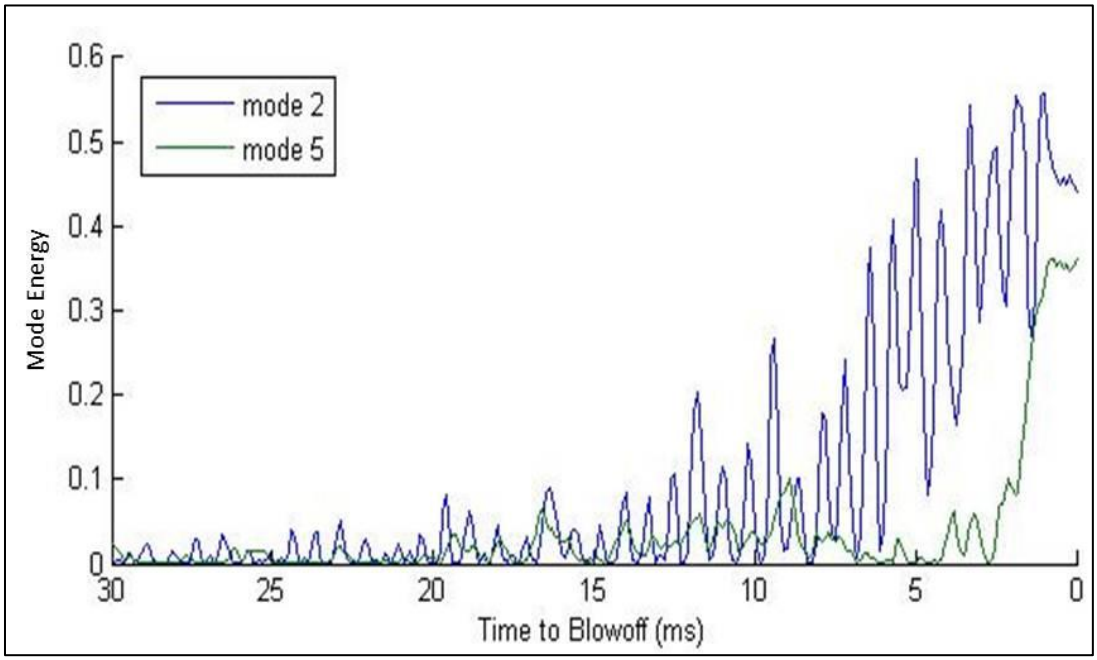

Figure 3.15: Energy of modes 2 and 5.

Significant second-mode activity begins around 12 ms prior to blowoff. This suggests that at this point, high strain pinches the flame off at midstream, where it continues to

reside for a brief time. The local extinctions from the flame pinching allow cooler air to flow with the density gradient and pull into the now extinct flame region. As this behavior continues, the increasing strain on the extinct region forces the flame to retreat closer to the bluff body, compressing the length of the recirculation zone. Then, significant fifth-mode activity begins. Its cool mid-field region and hot near-field region allow it to both negate the second mode's mid-field flame and enhance its near-field burning. A combination of the activity of these two modes provides for the flame to pull into the recirculation zone.

Further indications of this behavior come from an examination of the mode weighting coefficients, themselves. In the vortex-shedding modes, it is expected that the weighting constants will oscillate around zero to allow for alternating vortices within a single mode.

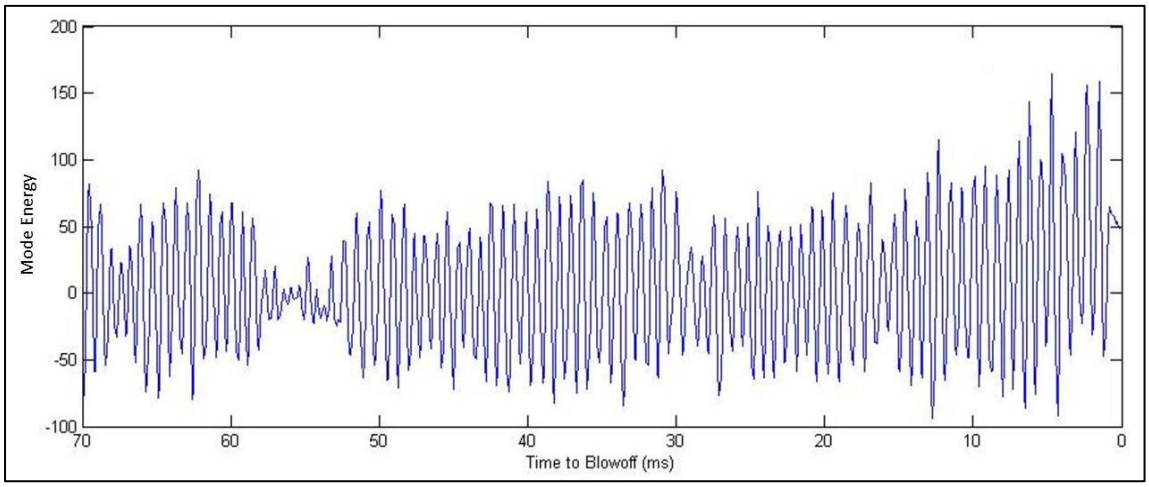

Figure 3.16: Mode 4 coefficients.

This indeed occurs, as shown in Figure 3.16. This mode oscillates fairly evenly around zero for the duration of the flame. Mode 5 exhibits a different behavior, however, as seen in Figure 3.17.

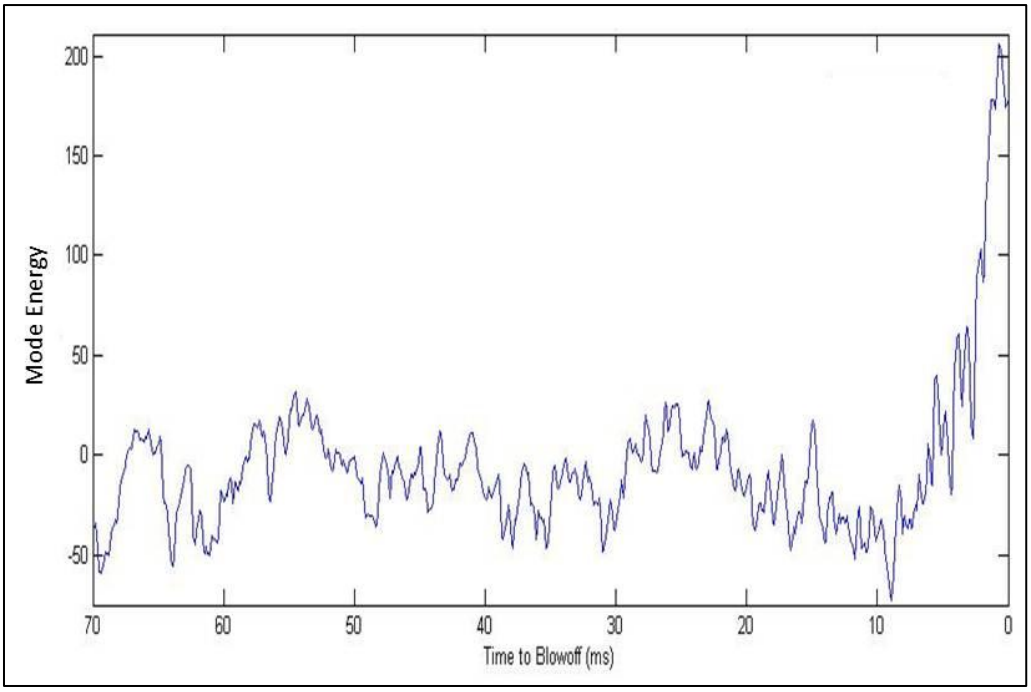

Figure 3.17: Mode 5 coefficients.

This mode remains negatively biased while the flame is stable, even at the point in time in the flame when the second mode becomes more active. Thus, the minor contributions to the flame reconstruction provided by this mode when the flame pinches off are additive to the mid-field burning. To compensate when the flame retreats, this mode's coefficients become positive as it follows the flame into the recirculation zone.

This sequence of events is best visualized from the high speed video frames shown in Figure 3.18. The images in Figure 3.18 have been selected to correspond with pertinent events from the mode energy plot.

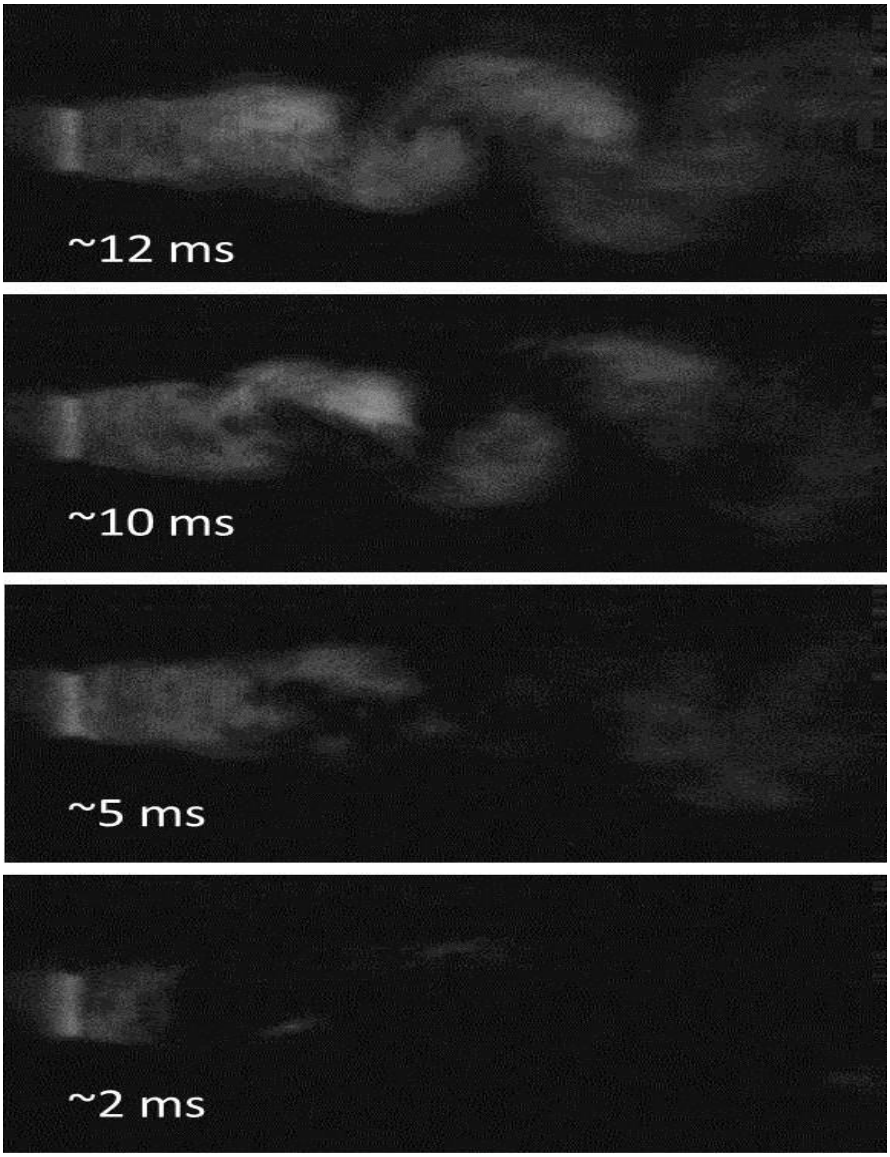

Figure 3.18: Flat-flame blowoff sequence of chemiluminescence images.

The first frame shows that at 12 ms prior to blowoff, strong vortex shedding is present, but the flame sheet remains intact throughout the entire flow field. The next frame at 10 ms prior to blowoff, shows the onset of flame pinching immediately upstream of

each vortex. At 5 ms prior to blowoff, when the strength of the flame pinching mode surpasses that of the vortex shedding modes, the high-speed image shows a significant decrease in chemiluminescence in the vortices. Now, the chemiluminescence emissions are largely secluded to the pinched flame. Finally, approximately 2 ms before blowoff, the flame pulls fully into the near-field of the recirculation zone where it resides until blowoff. This event corresponds with the rise in the recirculation zone burning mode.

Examining Figure 3.15 reveals that there is a clear characteristic frequency to the second mode oscillations, while the fifth mode dynamics are not as sharply defined. This is confirmed by an FFT of the mode coefficients. Figure 3.19 shows the frequency content of the second and fifth modes, together with the third mode, which represents vortex shedding.

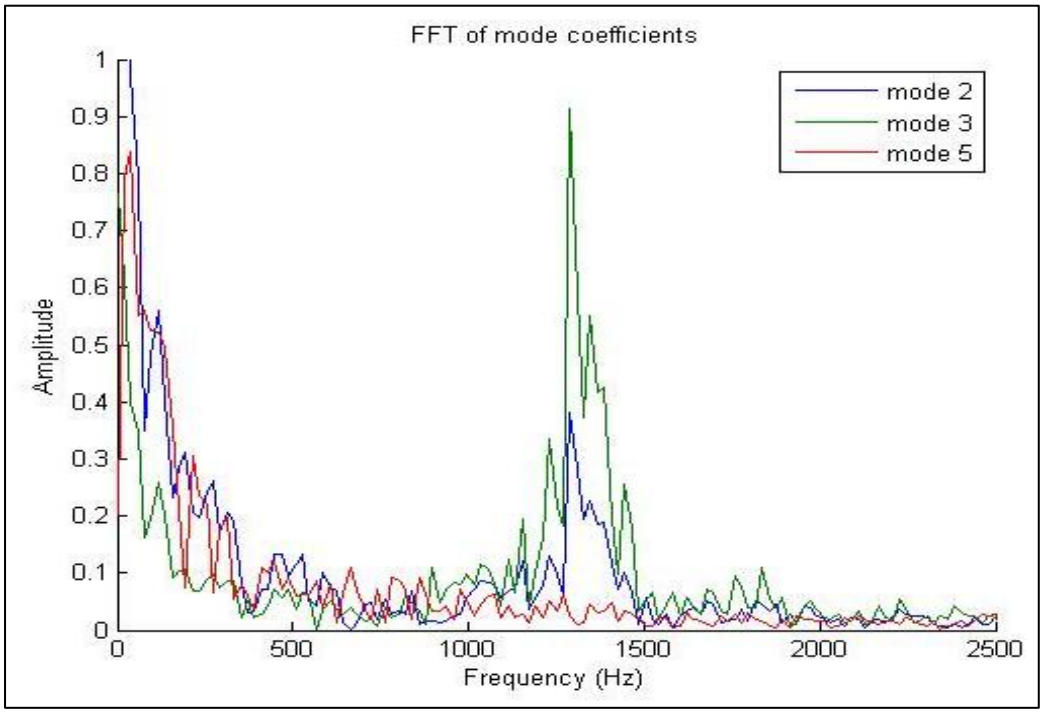

Figure 3.19: FFT of mode coefficients.

As previously expected, the fifth mode does not display a dominant frequency, while the second and third modes have a peak at 1289 Hz. This corresponds to the Strouhal number of vortex shedding and suggests that the second mode (flame pinching) and third mode (vortex shedding) are indeed coupled. This strengthens the conclusion drawn from the mode energy plot: the flame pinching comes as a result of strong vortex shedding.

The pattern displayed in the mode energies (Figure 3.13) and blowoff sequence images (Figure 3.18) are found in all of the symmetrically-fueled high speed videos, including those that did not contribute snapshot images to the POD mode shape determination.

3.6 Stratified flame analysis

To examine the effects of asymmetric fueling on the blowoff event, a similar POD analysis was performed on the high speed videos of the stratified flames. As was mentioned earlier, three different fuel gradients were imposed (ξ= 0.50, 0.75, and 1.00). All three stratified cases are similar in that they exhibit a single strong bottom shear layer, with significantly less burning in the ultra-lean top shear layer. As such, snapshot images from videos of all three cases were used together in the POD mode extraction, following the same algorithm of image selection from the three different temporal regions of the flame presented earlier. The results of the statistical analysis of mode shape correlations presented for the symmetrically-fueled cases were also followed. That is, four videos of each gradient type were deemed sufficient to completely

represent their respective flames, leading to a total of twelve videos and 3,000 snapshot images being used in the mode calculation.

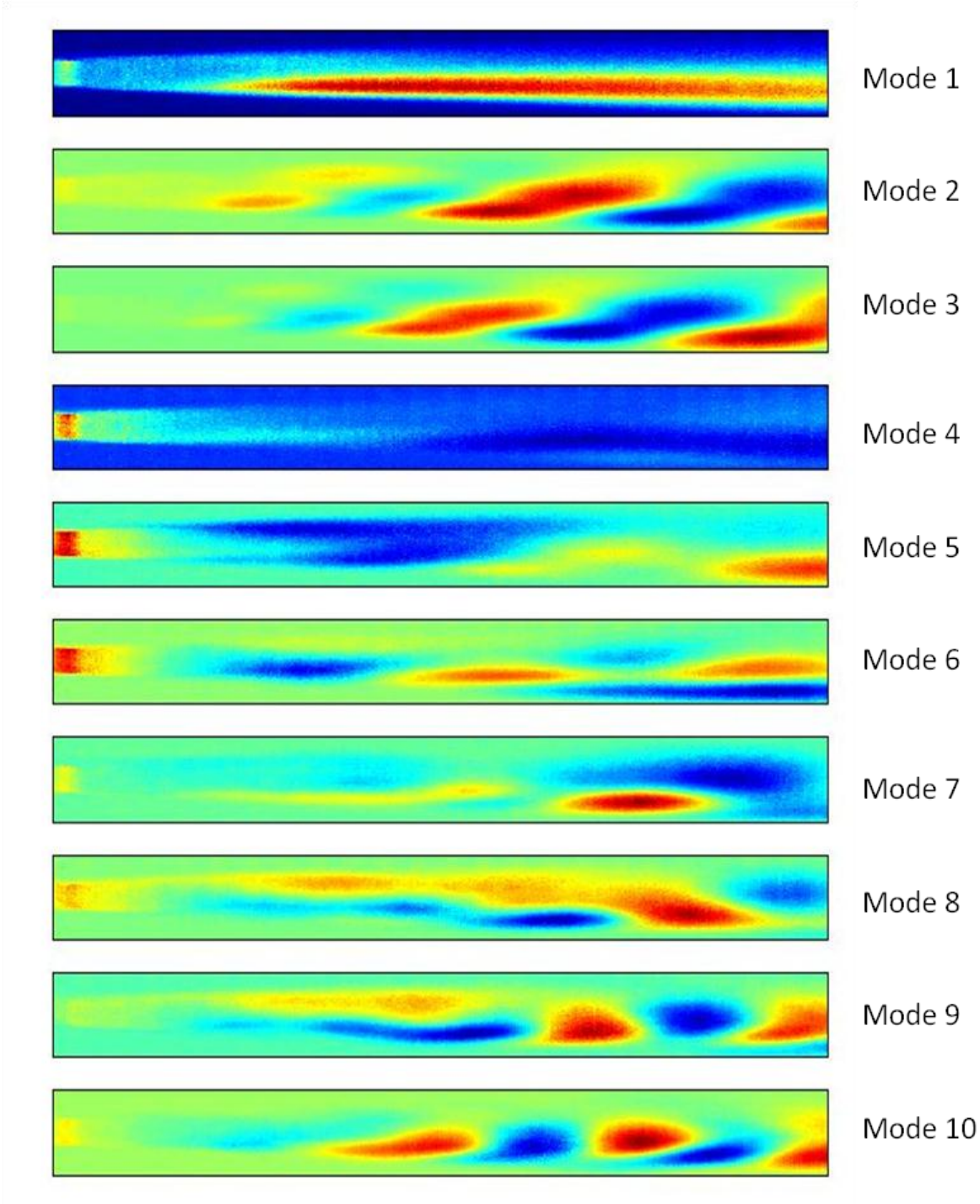

Figure 3.20: Mode shapes from all stratified fueling cases.

The first ten mode shapes are shown in Figure 3.20. The result is similar to the previous cases, in that the first mode is approximately the time-averaged flame, and among the next four modes are two phase-shifted vortex shedding modes (2-3), a flame pinching mode (4) and a recirculation zone burning mode (5).

The mode energies for a fuel gradient of 0.75 are shown in Figure 3.21. This time sequence is similar to that of the symmetrically-fueled flame. That is, vortex shedding weakens the time-averaged behavior until flame pinching occurs and leads to blowoff. However, other unique results come from a comparison of the flame pinching mode coefficients across the various fuel gradients (Figure 3.21).

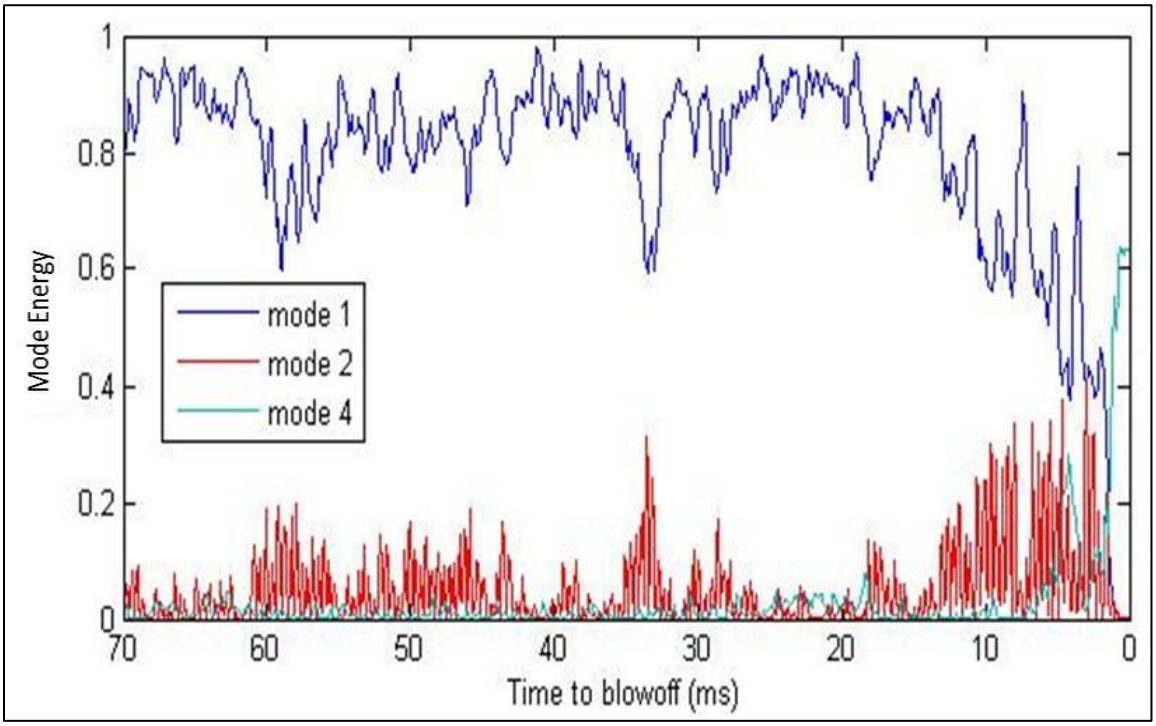

Figure 3.21: Mode energy for gradient 0.75.

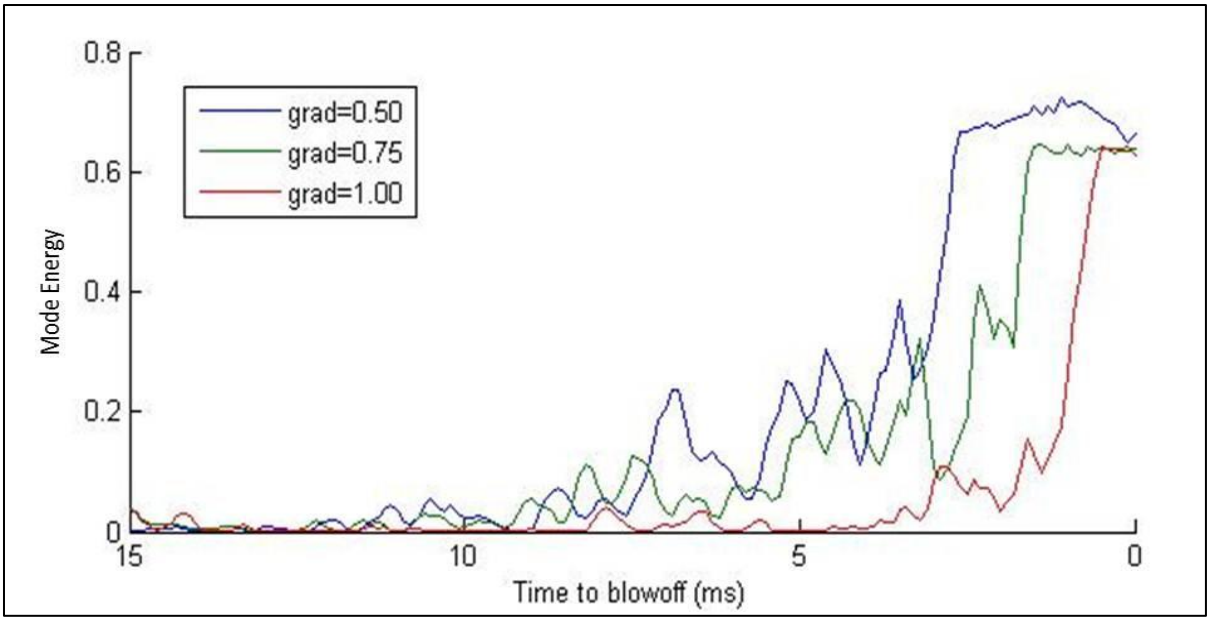

Figure 3.22: Fourth POD mode behavior of all fuel-gradient cases.

As the fuel gradient increases, the time lag between the peak of the flame pinching mode and the final blowoff event decreases. Although the flame pinching behavior has previously been shown to be coupled with vortex shedding, the increased longevity of the flame pinching mode with decreased fuel gradient is more closely related to the lean side burning of these stratified flames. Figure 3.2 showed that the fuel distribution along the rich shear layer of all these stratified flames at blowoff is nearly identical. Thus, the dilatative vorticity damping and overall vortex behavior along the rich shear layer at blowoff for each of these cases will be nearly identical. Figure 3.2 also showed that the equivalence ratios at the lean halves of the flames varied significantly from each other. In each case the lean shear layer was unable to support a flame without the piloting effect of the rich shear layer. However, the amount of burning in the lean shear layer still now appears to have a quantifiable effect on the flame. The increased fuel gradients decrease the fuel content and thus the amount of burning in the lean shear

layer. This makes it easier for the flame to retreat into the recirculation zone once it has been pinched. Hence, once the pinching occurs, the transition to blowoff happens more quickly.

Not only is the time between the peak of the flame pinching mode and blowoff longer with decreased flame gradients, but the onset of the flame pinching mode, on average, occurs sooner with decreased flame gradients. This means the phase between the start of flame pinching and the end of the chemiluminescence emission in the vortices endures longer. In the ξ=0.50 case, this transition phase is sufficiently long, in many instances, to allow the flame to strongly recover from this transient behavior. A few asymmetric data sets exclusive to the 0.50 gradient exhibited this pattern as shown in Figure 3.23.

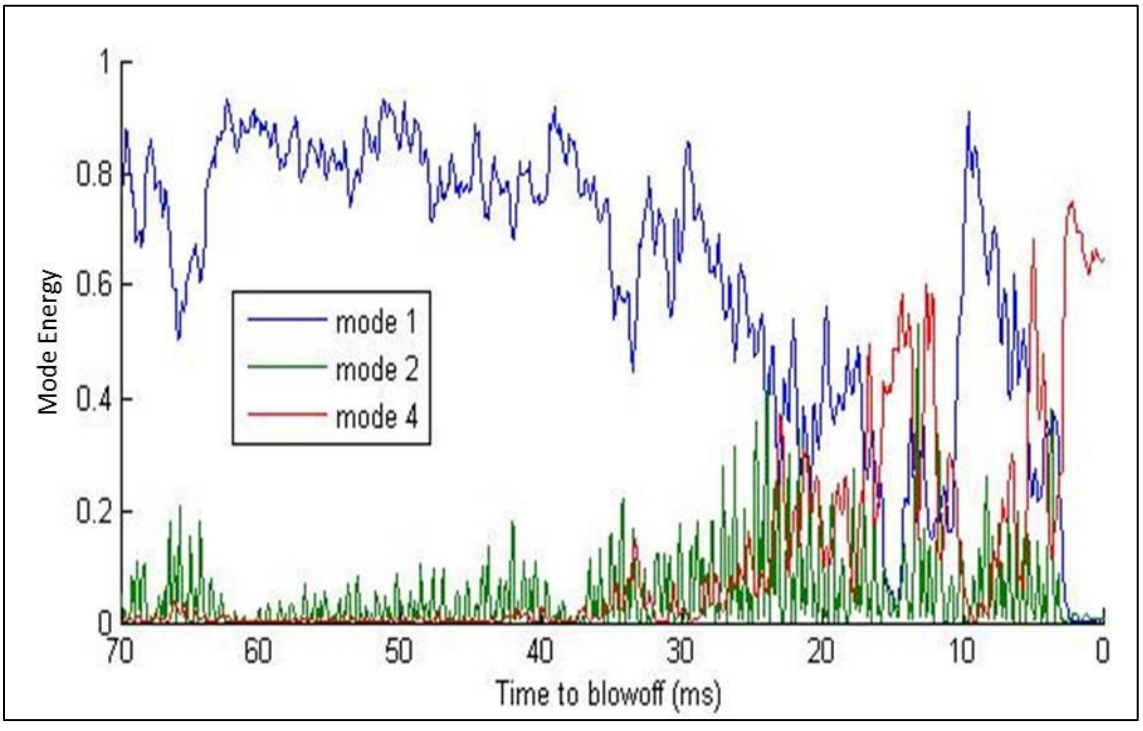

Figure 3.23: Mode energy plot with flame recovery for 0.50 gradient case.

As Fig. 3.23 shows, the first mode makes a full recovery after a point in which both the second and fourth mode behaviors surpass it. The rise time of the flame-pinching fourth mode during the first blowoff attempt is approximately 18 ms, whereas the rise time of the second and final attempt is approximately 10 ms. The 10-ms sequence is consistent with other 0.50 gradient blowoff sequences. The longer 18-ms sequence offers more time for a strong burst of burning to propagate through the pinched region of the flame, and realize a temporary recovery. Figure 3.24 shows a sequence of pertinent chemiluminescence images in this recovery process. In this particular data set, recovery occurs when a vortex from the top, lean shear layer curls into the high-strain, pinched region of the flame, allowing the flame sheet along the rich shear layer to reconnect.

The first frame in this figure shows that the flame pinching behavior is already dominant. In the next two frames, a pair of vortices are shed and then advect downstream where they connect, creating an intact top shear layer in their wake. Then, at 11 ms prior to blowoff, more vortices are shed which connect further upstream than the previous two, in the former pinched region. In the final frame, the bottom shear layer makes a full recovery, returning the flame to its time-averaged behavior.

The POD analysis reveals interesting dynamics from chemiluminescence but quantitative measurements of temperature and species are also required to understand changes in the flame and recirculation zone.

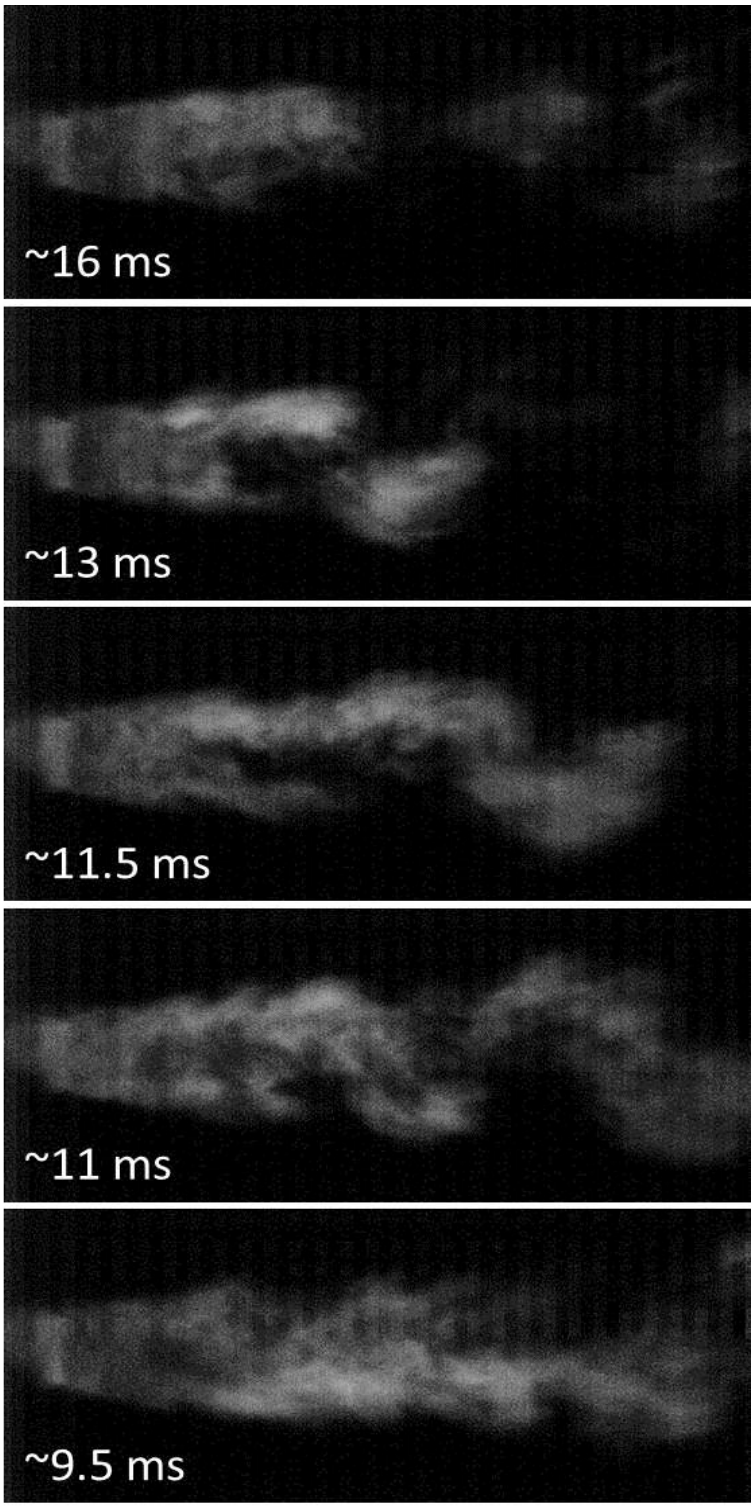

Figure 3.24: Flame recovery sequence of chemiluminescence images for 0.50 gradient case.

4 TDLAS Results

4.1 Laser characterization

Conventional equipment for characterizing the laser, such as a spectrometer, was not available in the wavelength range of this tunable diode laser. In order to understand the capabilities and limitations of the data-fitting techniques, certain information about the absorption lines must be known, such as their ground-state energies. Only the center wavelength at an unknown temperature of the laser was known from the manufacturer. The manufacturer-supplied laser calibration is shown in Figure 4.1.

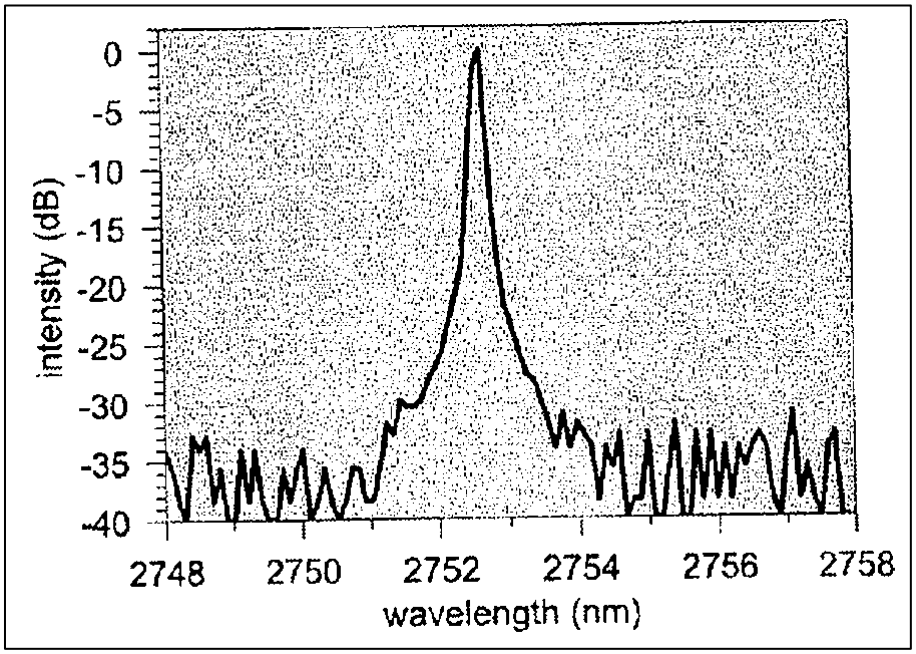

Figure 4.1: Laser power versus wavelength.

This calibration was used as a guideline for determining the full wavelength span of the laser. Multiple scans of the laser were performed at various temperatures and stitched together to map its full range (Figure 4.2). The data was processed using a direct

absorption analysis as described in detail in Section 4.3. This was then compared with the stick spectrum obtained from the HITRAN database [70], shown in Figure 4.3.

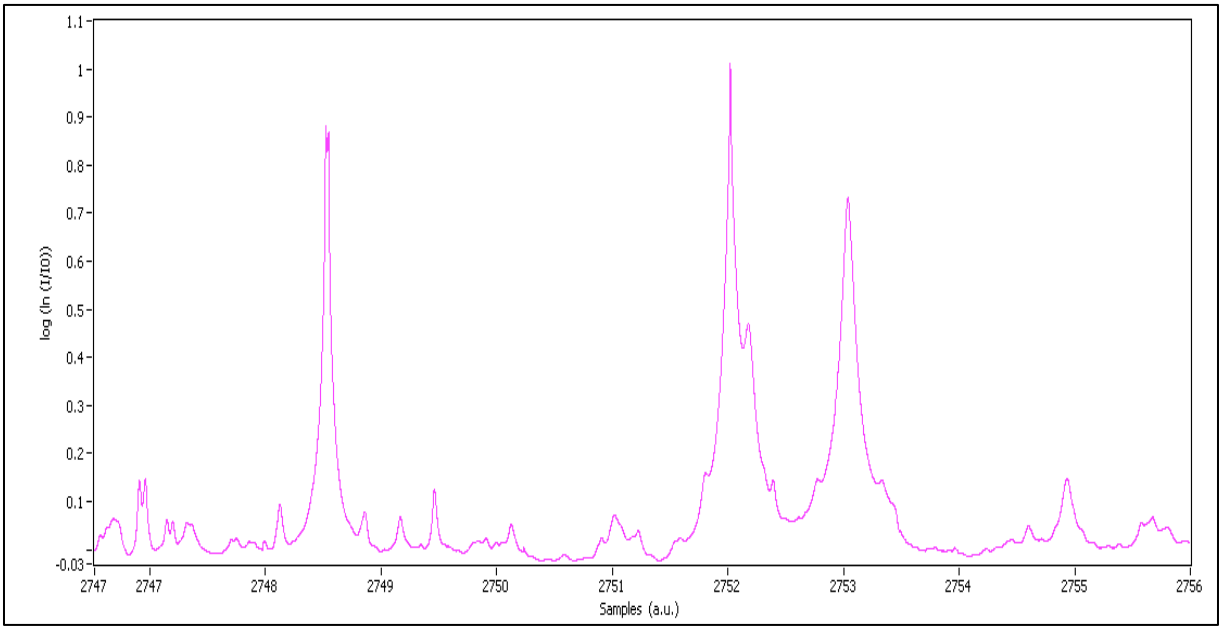

Figure 4.2: Spectral absorptivity across full range of TDL. Wavelength increases from left to right.

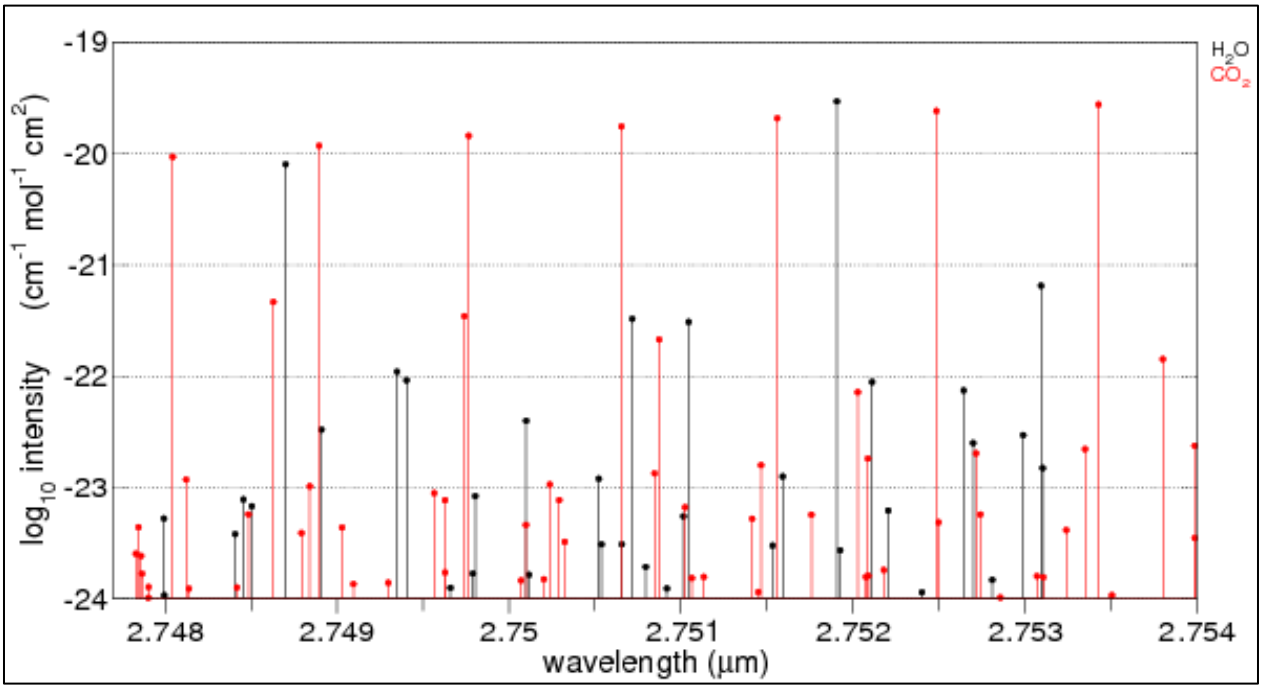

Figure 4.3: HITRAN spectra across full range of TDL [70].

The full wavelength range of the laser was determined to be approximately 6 nm. It is important to note that the wavelength response to changes in the laser current is not linear. According to the Joule effect, the rate of heat dissipation through a resistive conductor is proportional to the square of the current. Thus, the wavelength response will plateau slightly toward the top of the current ramp. This means, simply, that the laser mapping will not be able to line up perfectly with the HITRAN spectrum, and cannot be plotted accurately by wavelength without additional laser characterization which was not available during this study. As a result, a comparison of these two figures yielded a probable identification of the major absorption lines in the laser mapping.

4.2 Line selection

The purpose of the development of this TDLAS system is to obtain high frequency temperature and CO_2 species measurements near the bluff body in the previously discussed combustion rig. Temperature measurements are achieved from a ratio of the absorptivity of two lines of like species while species measurements can be obtained from a single line.

The full range of the laser was explored to find two CO_2 peaks that would work for these measurements. To identify which peaks were CO_2 absorption lines, as opposed to H_2O, the beam path was flooded with CO_2 gas while the detector response was monitored. Figure 4.4 highlights the significant CO_2 peaks on the laser mapping.

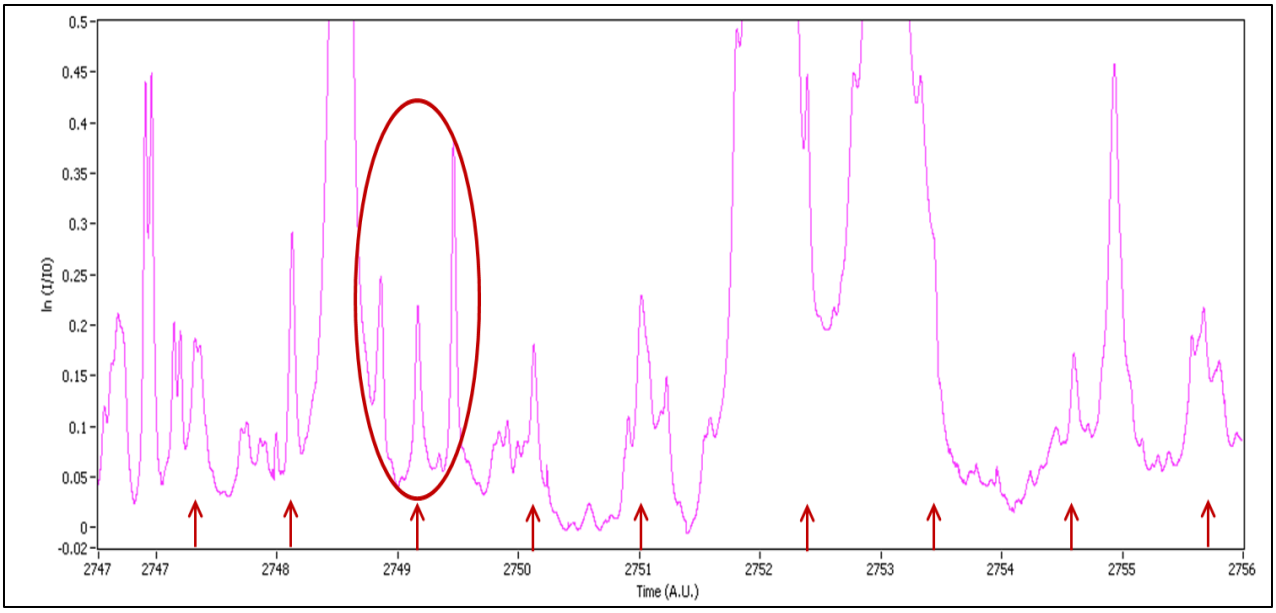

Figure 4.4: CO_2 absorption lines from TDL spectrum.

On the shorter wavelength end of the spectrum (left), the resistance to the thermoelectric controller (TEC) is high, resulting in little cooling of the laser. With the laser running hotter, it is difficult for the laser-heatsink system to reach thermal equilibrium. As a result, small perturbations in temperature yielded relatively large perturbations in output wavelength. Thus, for wavelengths below approximately 2749 nm, the laser output would oscillate significantly about the intended wavelength. Beyond the higher wavelengths on the spectrum, the laser power decayed to noise. Therefore, the optimal region to find suitable absorption lines was around the center of the laser's temperature tuning.

As is evident from Figure 4.4, many of the CO_2 line shapes are not isolated and are impacted significantly by other surrounding lines, both small and large. One CO_2 line that stands out as the most promising is surrounded by two similarly-intense H_2O lines.

This is fortuitous, as these lines can offer simultaneous CO_2 and H_2O species concentration measurements, and the ratio of the two water peaks can provide temperature readings. This triplet is circled in Figure 4.4. Note that the spectrum in this background does not reach the true background signal; i.e., these lines are superimposed on top of the wings of a large neighboring absorption line.

In order for the two H_2O lines to provide temperature readings, they must have sufficiently different ground state energies. In [71], it is shown that the ground state energies of the absorption lines must meet the following inequality:

$$|E_1" - E_2"| \geq \frac{X\% \cdot \sqrt{2}}{Y\%} \cdot \frac{k}{hc} \cdot T \tag{4.1}$$

where *X%* and *Y%* represent the percent errors of the calculated absorbance and resultant temperature, respectively. The H_2O transitions outlined in Figure 4.4 are at 3637.152 cm^{-1} and 3636.232 cm^{-1} with ground state energies of 325.216 cm^{-1} and 1908.016 cm^{-1}, respectively. Thus, if the absorbance can be determined within 4%, and a temperature accuracy of 6% is desired, the maximum temperature to which this line pair would be sensitive is 2415 K. This shows that these lines are suitable for this experiment, as their maximum temperature sensitivity for these parameters is greater than the adiabatic flame temperature for a propane flame at stoichiometric conditions. If this high sensitivity is not needed, the accuracy requirements can be made stricter.

4.3 Direct Spectroscopy

Direct spectroscopy is a simple method in which Voigt curves are simulated and fitted to the absorptivity of the experimental data. This is calculated by taking the natural log of the Beer-Lambert equation [38].

$$\alpha \propto \ln\left(\frac{I}{I_0}\right) \tag{4.2}$$

Difficulty can arise when determining the background laser intensity term, $I_{0.}$ In this case, a second order polynomial was fit along the absorption ramp to provide the background term. Portions of the output ramp where the least absorption occurs were sampled to provide curve-fitting data for the creation of the background quadratic. An absorption ramp with its associated background fit is shown in Figure 4.5.

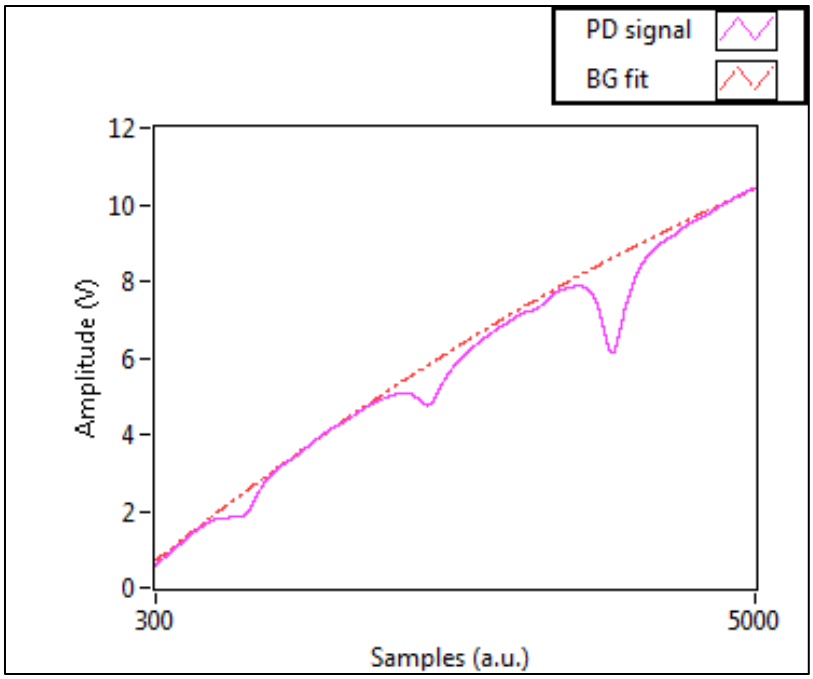

Figure 4.5: Detector signal with absorption and interpolated background.

The absorptivity is calculated and then fit using a Levenburg-Marquardt non-linear algorithm to determine the Voigt parameters that best match the data. As defined in Equation 1.17, a Voigt lineshape is a convolution of Gaussian and Lorentzian lineshapes. Thus, to resolve a single Voigt peak, four parameters are required: Gaussian halfwidth, Lorentzian halfwidth, peak intensity, and line center. When fitting to multiple peaks, each requires its own set of parameters. However, it was found that the relative difference between line centers of the different peaks was consistent across all temperatures examined. Thus, only one line center parameter was needed to describe multiple lines. Relations between the Gaussian and Lorentzian halfwidths of different peaks were examined; however, no conclusive results were obtained. This is likely due to the level of noise and background issues encountered. A return to these studies could provide increased performance of the fitting algorithm in the future.

The Voigt parameters described can be used to calculate the areas under the absorption curves. Applied to a calibration curve, the ratio of fit areas reveals the line-integrated temperature of the absorbing gas. As was mentioned previously, the algorithm used to create the Voigt profiles for least-squares data fitting employed a weighted sum equation of Gaussian and Lorentzian contributions. This equation was integrated analytically to produce the area under the curves:

$$A_V = m(1.77\sqrt{\frac{1}{\pi}}C_G + 2C_L) \tag{4.3}$$

where A_V is the area of a Voigt, m is the peak intensity, C_G is the Gaussian weight, and C_L is the Lorentzian weight. C_G and C_L are elements of [0,1] where $C_G + C_L = 1$ and are functions of their respective halfwidths [46].

Direct spectroscopy is highly dependent on the background term. Although a good background fit can be produced for the available data, it cannot take into account the absorption outside of its current scan that may be affecting the lines within its range. This point is illustrated in a comparison of Figure 4.6 and Figure 4.7.

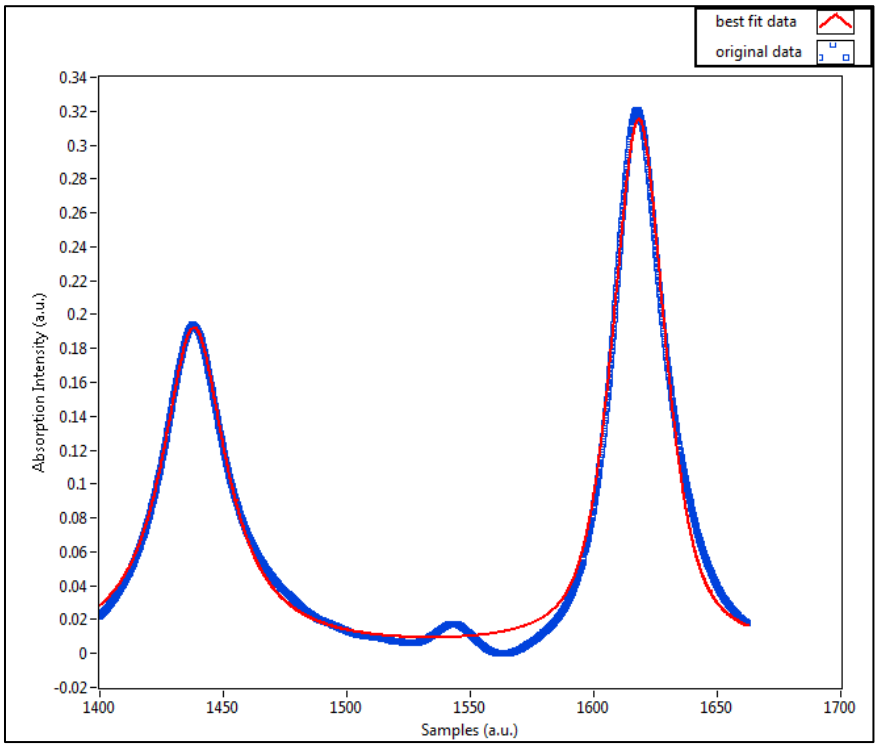

Figure 4.6: Two-peak Voigt fit.

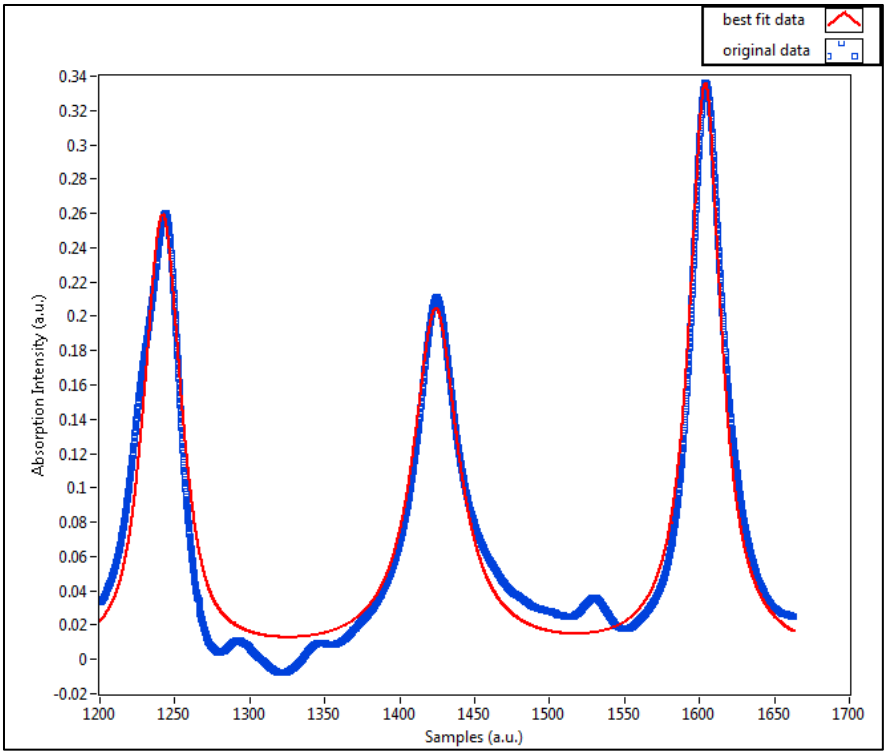

Figure 4.7: Three-peak Voigt fit.

The first (Fig. 4.6) is a scan over the right two lines from the circled region of Fig. 4.4, and the second (Fig. 4.7) is a scan over all three. Both figures display a good fit of the Voigt peaks. In the two-peak fit, data points between the two large peaks were used in the interpolation of the background. This forced the quantity (I/I_0) to be zero at those points. It is seen that the simulated Voigt peaks in the best fit curve are unable to decay to zero that quickly. In Figure 4.7, the range of the laser was wider, introducing a third major peak on the left. The points selected for use in this background interpolation were between the first two peaks. This raised the background floor between the original two peaks to a more accurate level, but the background between the first pair then became incorrect. From Fig. 4.4, it is apparent that neither of these scans determines the true background, which lies far outside this region of the spectrum.

It can be shown that the wing of a Voigt line shape will decay to 1% of its peak absorbance at approximately 4 line widths from the center wavelength [72]. A review of the laser mapping in Figure 4.4 shows that these selected peaks are sitting well within four line widths of other significant peaks. This means that the peaks of interest are riding on non-negligible amounts of absorption from other peaks.

Another source of error in the signal is the infrared emissions from the burner flame that are within the sensitivity of the photodiode detector. As was shown earlier in the setup, an aperture was positioned between the burner and detector to minimize reception of these photons while letting the collimated laser beam through. For the purposes of the calibration, it was found that this source of error increased at lower equivalence ratios. Figure 4.8 shows the detector output from the flame emissions at two different equivalence ratios without the presence of the laser.

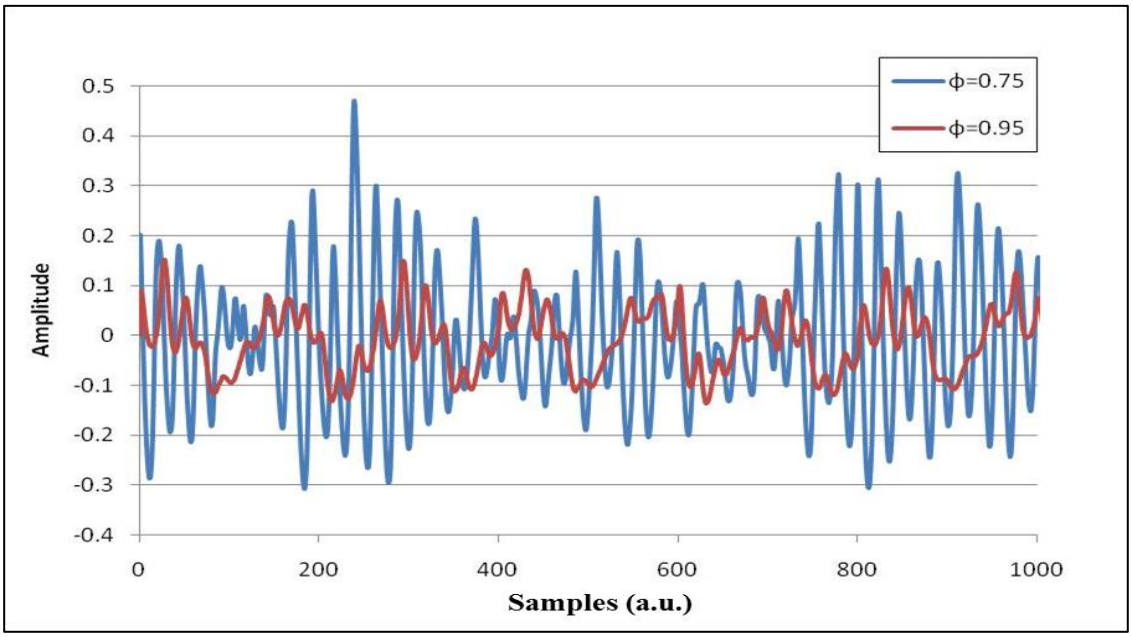

Figure 4.8: Detector signal of McKenna burner emissions.

The periodic nature of the emissions in Fig. 4.8 is likely due to buoyancy-driven oscillations in the flame. The effect of this flame signal on the absorption profiles will vary, depending on the laser power at a given absorption line. Compared to the scan shown in Fig. 4.5, the flame emission signal across the two equivalence ratios shown represents approximately 5-22% of the first (lower laser power) peak, and 1-5% of the last (higher laser power) peak. This flame emission signal was decreased by further closing the aperture in front of the detector (see Fig. 2.11).

These sources of error, namely the strong neighboring absorption and the flame emissions, contribute to an inaccurate calibration curve. Figure 4.9-Figure 4.10 show the results of the data fitting to obtain integrated absorption areas under the Voigt line shapes for calibration. The data points displayed are averages over multiple runs.

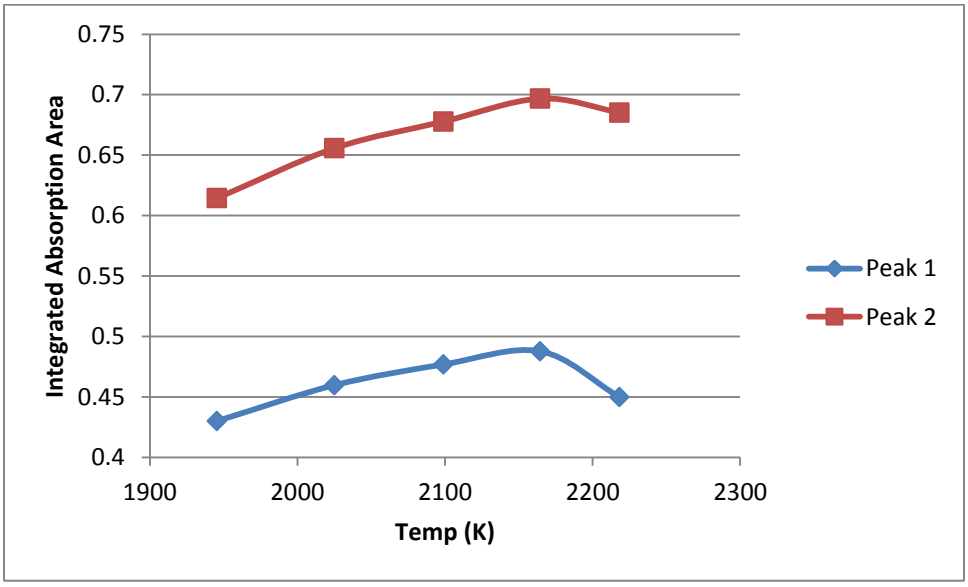

Figure 4.9: Integrated absorption areas of two H_2O peaks versus adiabatic flame temperature.

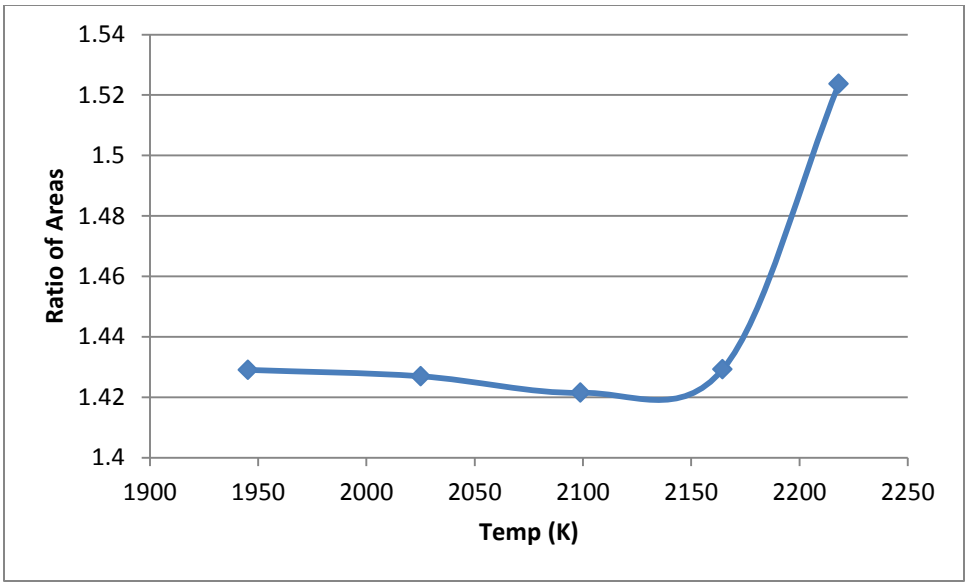

Figure 4.10: Area ratio of two H_2O lines versus adiabatic flame temperature.

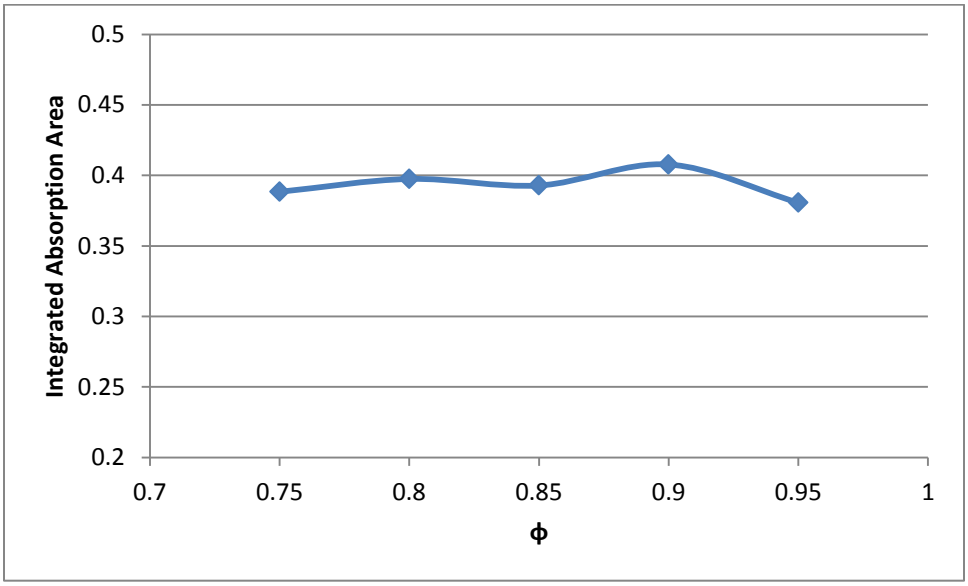

Figure 4.11: Integrated absorption area of CO_2 peak versus equivalence ratio.

The data in Figure 4.9-Figure 4.10 is plotted against the adiabatic flame temperatures of the injected equivalence ratios. It is well understood that there will be heat loss through the perforated surface of the McKenna burner; however, these temperatures represent a reasonable approximation of the actual flame temperature at this stage.

Figure 4.10 shows that there is a definite trend of increasing absorption in both peaks with increasing temperature, although this fails at the final data point. More importantly, the slope of increase in the two lines in Figure 4.9 is different, which allows for variation in their ratio at different temperatures (Figure 4.10). The results in Figure 4.10, however, are disappointing. The trend is not consistent at higher temperatures, and at lower temperatures, the sensitivity is extremely low. That is, the percent difference in the area ratio from approximately 1950 K to 2100 K is only .5%. Furthermore, the change in absorption of the CO_2 peak across the range of equivalence ratios, shown in Figure 4.11, is also negligible.

The low temperature sensitivity in the CO_2 and H_2O peaks can be explained by the lack of background accountability from a large neighboring H_2O line. The suggested range for a laser scan to appropriately account for the background signal is shown in Figure 4.12, and the pertinent parameters from HITRAN [70] for its major peaks are in Table 4.2.

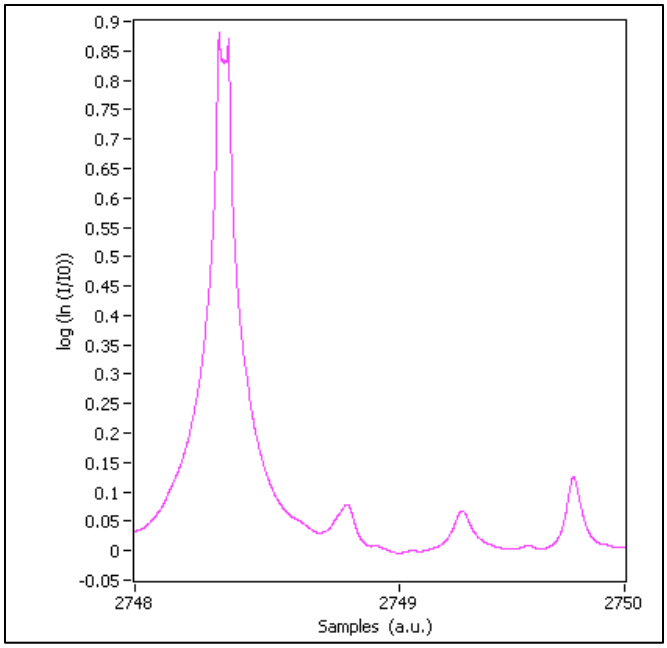

Figure 4.12: Suggested range of laser scan.

	Species	Line Center (nm)	Intensity ($cm^{-1}/mol*cm^{-2}$)	Lower-State Energy (cm^{-1})
Peak 1	H_2O	2748.701	7.988E-21	42.372
Peak 2	H_2O	2749.404	9.198E-23	325.216
Peak 3	CO_2	2749.766	1.442E-20	464.172
Peak 4	H_2O	2750.099	3.982E-23	1908.016

Table 4.2: Selected HITRAN [70] parameters for suggested absorption peaks.

Lines with very high lower-state energy (E") will exhibit less absorbance than lines with smaller E" [72]. As is shown from Figure 4.12 and Table 4.2, the H_2O line with the largest E" is situated furthest from the line with the largest intensity. That is, the line that should have the smallest magnitude of response to changes in temperature is the line that is least affected by the background, whereas the increases in intensity of the

more responsive line are “absorbed” into the changes in the background signal. This explains the lack of sensitivity in both the temperature data and the CO_2 species data. As is, this method is unable to resolve the temperature and species concentration information desired.

4.4 Wavelength Modulation Spectroscopy

Wavelength modulation spectroscopy (WMS) is a convenient and potentially more precise method than direct spectroscopy as it does not require the calculation of background intensity. In WMS, the diode laser is driven by a fast sinusoidal modulation superimposed on a slower ascending ramp. This can significantly reduce 1/f noise by shifting detection to higher frequencies [73].

An important dimensionless parameter in WMS is the modulation depth [73]:

$$m = \frac{a}{\Delta\nu/2} \tag{4.4}$$

where a (cm^{-1}) is the modulation amplitude and $\Delta\nu/2$ (cm^{-1}) is the half width of the transition. The work of Reid and Labrie [74] showed that the signal-to-noise ratio is optimized at m=2.2. For the absorption lines in this study, this equation yields optimum modulation amplitude in the range of [0.015, 0.02].

A software lock-in amplifier is applied to the signal to obtain the 1f and 2f signals, and to remove the modulation frequencies using a digital Bessel filter. The derivation relating the respective 1f and 2f line shapes to the first and second harmonic of the signal is

given in [74]. Figure 4.13 shows an example of raw data from the photodiode detector with its 1f, 2f, and 2f/1f signals.

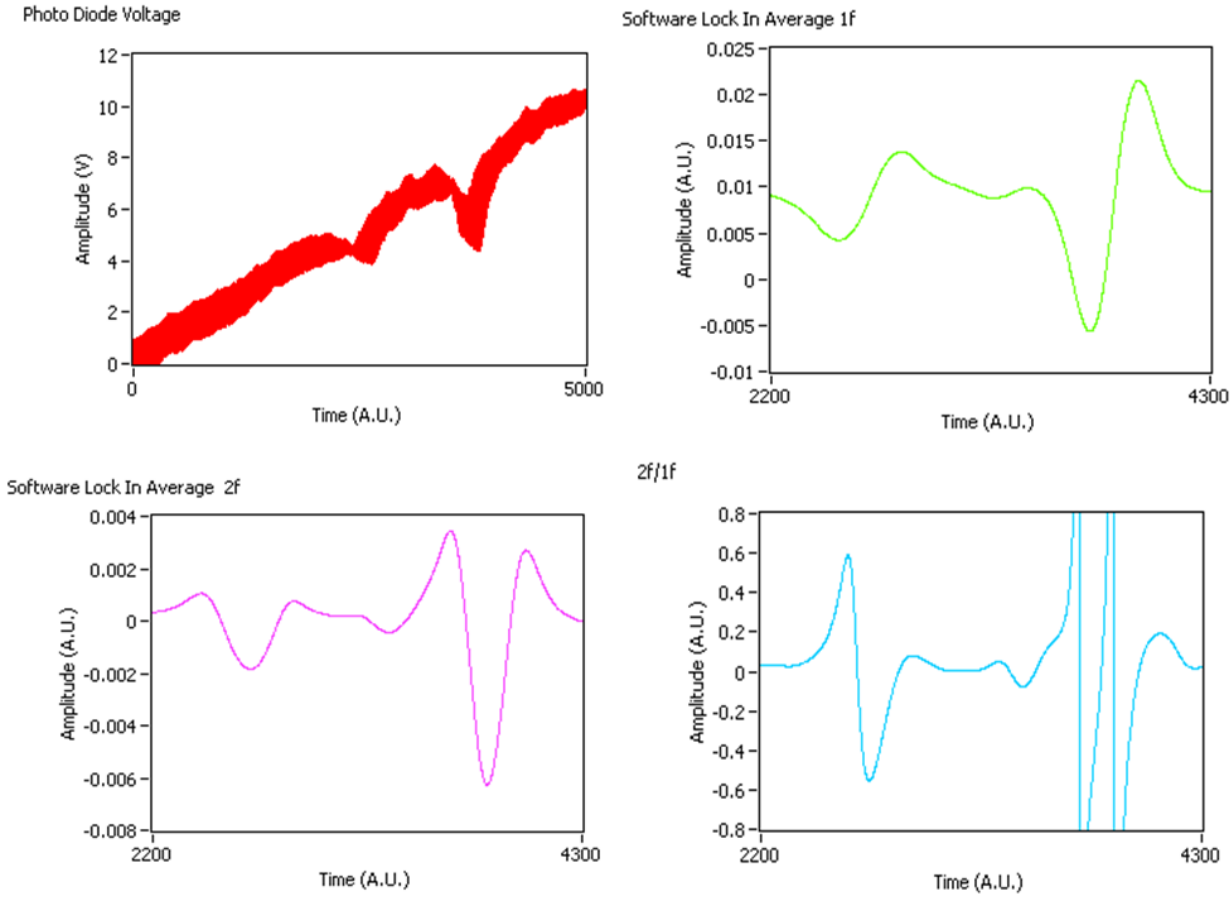

Figure 4.13: WMS data. Raw signal (top left), 1f signal (top right), 2f signal (bottom left), 2f/1f signal (bottom right)

The data in Figure 4.13 was obtained using a modulation depth in the approximate range specified by Equation 4.4, a modulation frequency of 2 kHz, and ramp frequency of 9 Hz with 10,000 samples per ramp (5000 ascending, 5000 descending).

There are a couple of important points that always hold true for the harmonic line shapes [72]. First, for a single absorption line, the Nth-harmonic has N+1 turning points. Second, the (N+1)th harmonic is smaller in magnitude than the Nth harmonic. Thus, for

an optimal signal, the first and second harmonics are widely used, rather than the third and fourth, for example.

As it is the ratio of the 2f to 1f harmonics that produce a background-independent signal [50], inherent problems come from the data shown above. The 2f and 1f signals are proportional to the approximate second and first derivatives of the absorption profile, respectively. If absorption is strong, the slope of the absorption line situated on an ascending ramp will become negative at certain points. This causes the 1f profile to cross zero and creates singularities in the 2f/1f signal, as shown in Figure 4.13.

These spikes can be avoided by decreasing the slope of the incident ramp, which means slightly defocusing the laser to decrease power to the detector, or by tuning the laser to position the absorption lines lower along the ramp. Less laser power means less absorption, which keeps the 1f signal above zero.

Another problem with WMS in this setup is the high frequency response requirements. As the ramp frequency increases for faster data rates, the modulation frequency must also increase in order for the technique to work. It was found for this experiment that these high frequency modulations produced fluctuations in the laser response that could not be simulated. This laser response is believed to be a result of heat management and significant lags in the thermal cooling. At lower frequencies, the 2f/1f profile visually appeared to be more accurate, but it still could not accurately be simulated. Figure 4.14 shows an attempted fit of a 2f/1f profile taken at 9 Hz. It is clear

that the general shape of the 2f/1f profile was simulated, but it was not able to fit the actual data.

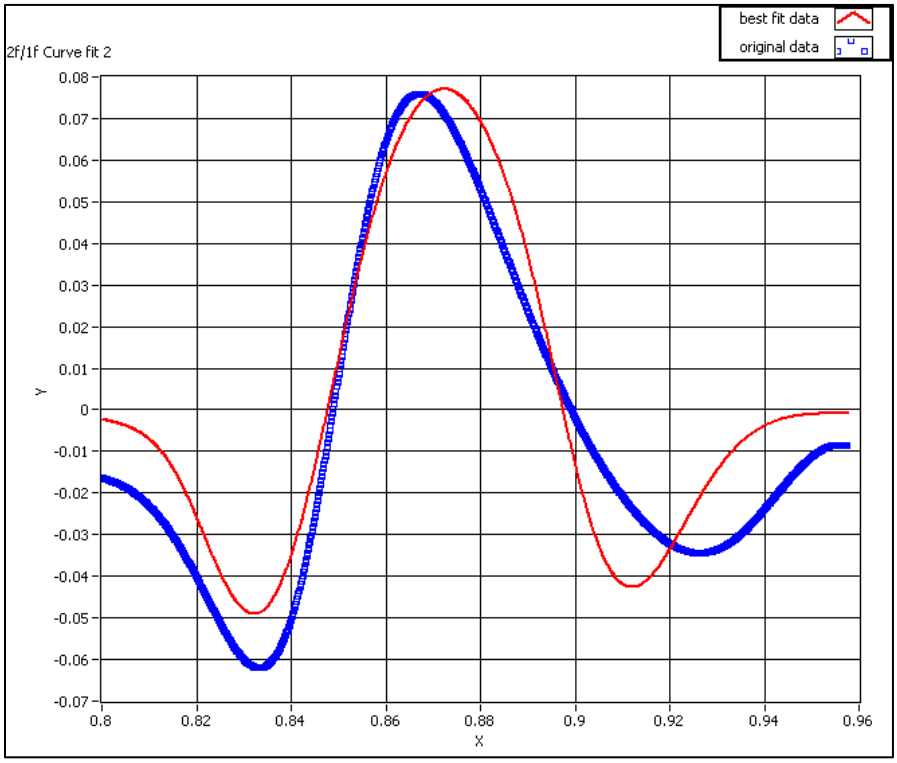

Figure 4.14: Fit of 2f/1f profile.

Both direct spectroscopy and WMS are determined to be promising techniques for this setup, although each requires further refinement to both the laser hardware and the simulation software.

5 Conclusions and Future Work

5.1 Vitiated Blowoff Mechanism

The principle orthogonal decomposition (POD) analysis presented in Chap. 3 was successful in capturing partial and final blowoff events from the chemiluminescence images. Precursors to both lean blowoff and flame recovery were identified. An effect of fuel stratification on blowoff was also discovered in the decreased time lag between the peak of the flame pinching behavior and final blowoff with increased fuel gradients. This is hypothesized to be due to the decreased burning in the lean shear layer offering less resistance for the flame retreating into the recirculation zone.

In the case of blowoff, the dominance of Von Kármán vortex shedding in the flame dynamics was the first major indicator of significant weakening of the flame. This led to local strain-induced extinction, or a "pinching off" of the flame at the trailing edges of the vortices – a process that immediately preceded blowoff. The frequency content of these two processes suggests they are coupled.

When sufficient burning is present in both shear layers, the flame has the ability to temporarily recover to its stable behavior after the onset of both heavy vortex shedding and strain-induced pinching. Given sufficient time, a strongly-burning vortex of opposite vorticity to that of the vortex which led to the extinct region can reconnect the shear layers and allow the flame to recover. This mechanism describing the blowoff and potential recovery process is summarized in Figure 5.1.

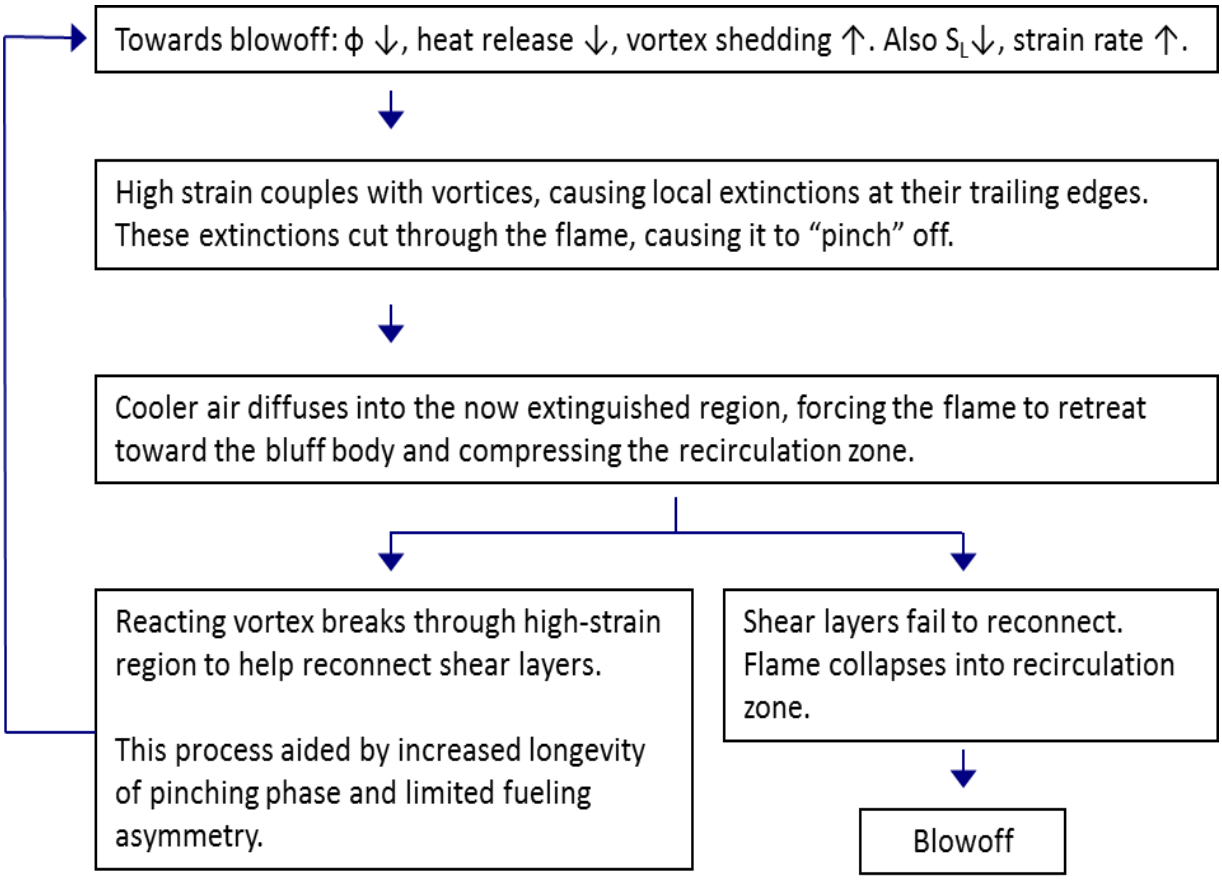

Figure 5.1: Vitiated blowoff mechanism.

An analysis was performed to ensure that the data set used in the POD algorithm was statistically converged, and able to accurately describe the flames it represented. There is still much, however, that can be learned from these flames. A more complete comparison of the vitiated flames to their unvitiated counterparts is needed. It is expected that vortex shedding has a lesser effect on unvitiated flames, and while recirculation zone burning has been identified as a major process preceding blowoff [68], the mechanism that leads to this can be different from that in the vitiated flames. It will also be interesting to examine how the time lag between the onset/peak of the final blowoff precursor mode in unvitiated flames compares to that in vitiated flames with varying fuel gradients.

Future work on the bluff body combustion rig will also certainly include an examination of strong acoustically-coupled flames. Preliminary tests were performed by removing the rig's acoustic mufflers downstream of the test section (see Fig. 2.1). FFT's of pressure transducer data with and without the acoustic mufflers are shown in Figure 5.2.

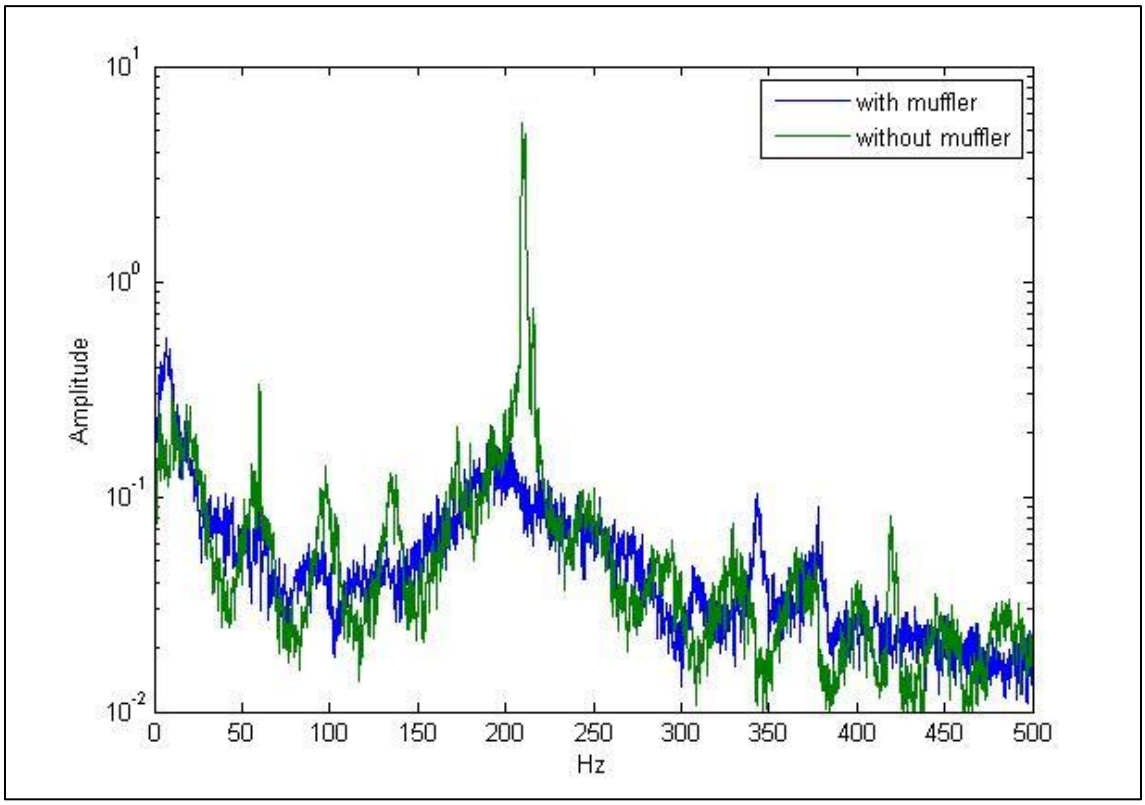

Figure 5.2: FFT's of pressure traces with and without acoustic damping.

It is clear from Figure 5.2 that the muffler significantly damps the primary mode at approximately 210 Hz and almost entirely damps out the modes around 100 and 135 Hz. The increased acoustic coupling has not had an effect on the vitiated blowoff equivalence ratio, but can still potentially affect the dynamics near blowoff.

Other future work will also include the testing of new bluff body geometries. In particular, a bluff body that can accommodate the TDLAS experiment needs to be machined.

5.2 TDLAS

The TDLAS system was successfully assembled and the diode laser was characterized. Experiments with a McKenna burner providing the absorbing medium were performed using various data acquisition techniques. The viabilities and limitations of both direct spectroscopy and wavelength modulation spectroscopy were examined.

Wavelength modulated spectroscopy is determined to be a potential technique for future use. This method is useful as it eliminates the necessity for a background laser signal. However, the laser was not able to respond accurately at the high frequency required by this technique. This caused discrepancies between the expected and actual laser wavelength output during modulation in the data acquired, making simulation of the data inaccurate. Future improvements can be made by finding a modulation frequency/amplitude to which the laser responds more linearly. Also, modifications to the laser's thermal system may aid in decreasing the time lag of its response.

Direct spectroscopy proved to be an excellent method for obtaining accurate data that is relatively simple to simulate. The resulting absorption peaks fit well with simulated Voigt peaks. The requirement that the background laser intensity be estimated in order for this technique to work caused the extrapolated temperatures and concentrations to be inaccurate; however, there was not an appropriate region of the laser scan that could provide a baseline for the background function. Other methods to estimate the background, for example by flooding the test section with non-absorbing gases, should be explored. This method can be improved by including the large H_2O line which has close proximity to the three lines of interest and is most significantly affecting the background signal (Fig. 4.4).

The larger H_2O peak, with an estimated line center at 2748.701 nm, could potentially be used in place of the first H_2O line for temperature measurements. It has a smaller ground state energy, which would make the ground state energy difference between the two peaks larger, thus increasing sensitivity at higher temperatures. However, because the line intensity is so much greater than that of the second, the signal-to-noise ratios of this line pair could be significantly different. Also, due to the strong line intensity of this peak, at some concentrations it tends to absorb more laser light than the detector can sense. Such a saturated signal would not be usable. If this large H_2O line proves to be unusable, it can still be simulated for the purposes of obtaining a background signal by scaling it appropriately with the other two measured peaks.

The reason these opportunities were not explored further is that the laser had difficulty stabilizing at this wavelength. The large heat sink did not allow the laser to reach thermal equilibrium without significant oscillations in this range. Improvements can be made by redesigning the heat sink to expand the laser's stable emission range. It is believed that a modification to the heat sink would make direct spectroscopy the most viable method for this setup.

When the TDLAS system issues are resolved and a bluff body is designed to support it, high frequency temperature and species measurements of gases near the bluff body and flame recirculation zone can be taken. This is expected to add significant insight into the blowoff behavior presented in this thesis.

Appendix A: Pin diagram for Nanoplus 525-2753-2 diode laser

Figure A.1 displays the pin labeling on the diode laser, and the pin assignments are shown in Fig. A.2, along with the corresponding cable wiring. Color-coding in Fig. A.2 indicates the color of the wire insulation.

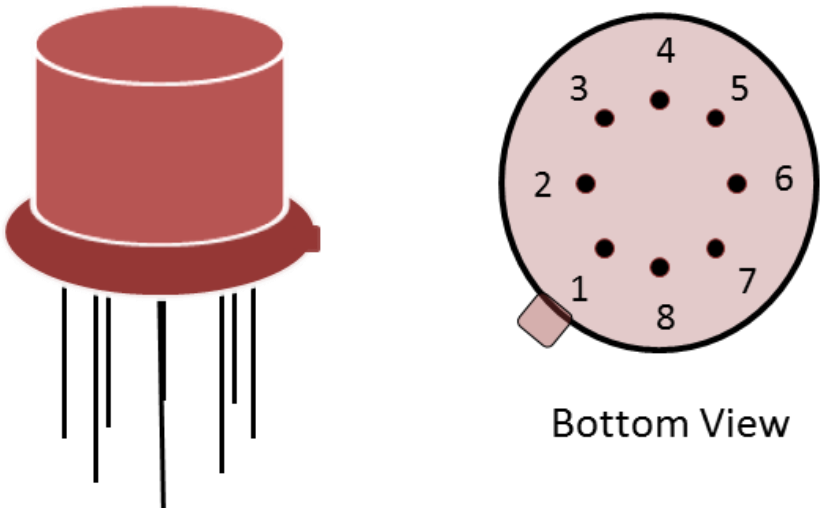

Figure A. 1: Diode laser diagram.

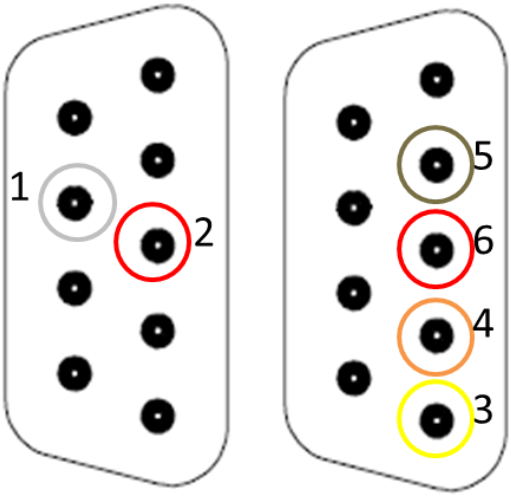

Pin	Function
1	LD (+)
2	LD (-)
3	TEC (-)
4	TEC (+)
5	Thermistor (-)
6	Thermistor (+)
7	N/A
8	N/A

Figure A. 2: Diode laser pin assignment and cable wiring for current controller (LDC 500) and thermoelectric controller (TEC 2000)

Appendix B: LabVIEW front panels and block diagrams for curve-fitting VI's

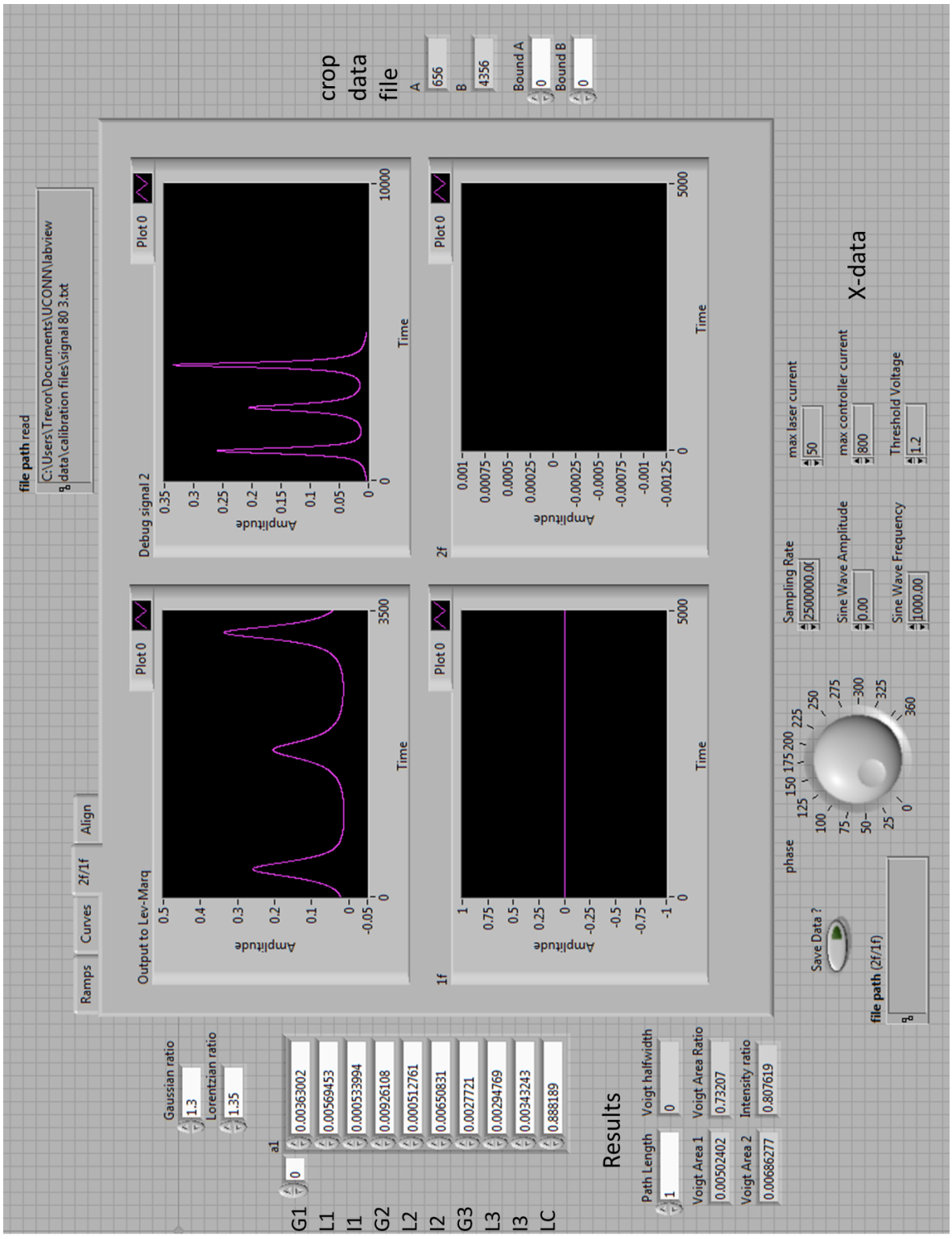

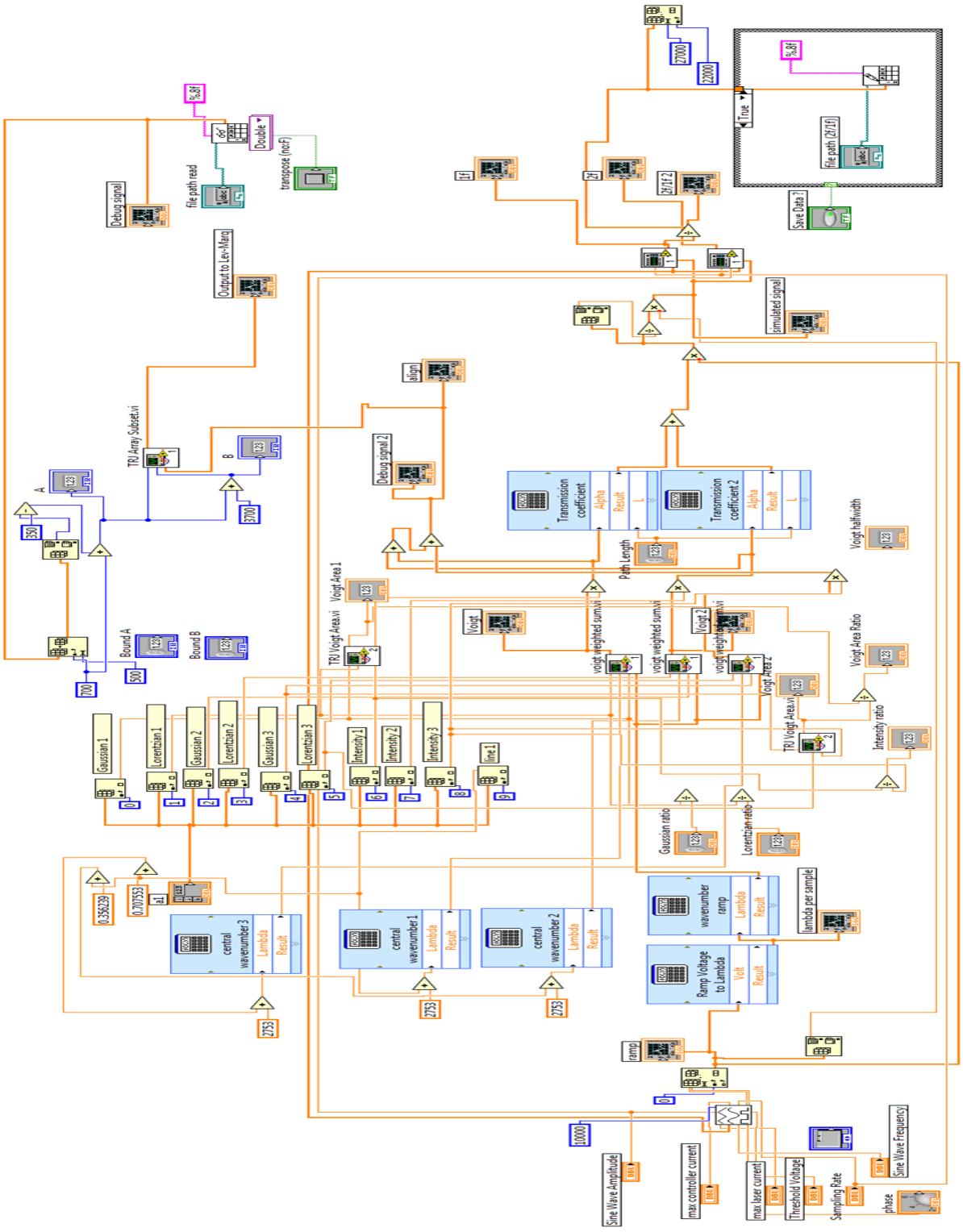
%.8f
Double
file path read
transpose (no)
Debug signal
Output to Lev-Marq
TRJ Array Subset.vi
A
B
3550
3700
700
500
Bound A
Bound B
align
Debug signal 2
Transmission coefficient
Alpha
Result
L
Transmission coefficient 2
simulated signal
Path Length
Voigt Area 1
TRJ Voigt Area.vi
Voigt
voigt weighted sum.vi
Voigt 2
Voigt Area2
Voigt halfwidth
Voigt Area Ratio
Intensity ratio
Gaussian 1
Lorentzian 1
Gaussian 2
Lorentzian 2
Gaussian 3
Lorentzian 3
Intensity 1
Intensity 2
Intensity 3
line 1
Gaussian ratio
Lorentzian ratio
0.356239
0.707553
central wavenumber 3
central wavenumber 1
central wavenumber 2
Lambda
2753
wavenumber ramp
lambda per sample
Ramp Voltage to Lambda
Volt
ramp
10000
Sine Wave Amplitude
max controller current
max laser current
Threshold Voltage
Sampling Rate
Sine Wave Frequency
phase
27000
22000
True
File path (2/15)
Save Data 3

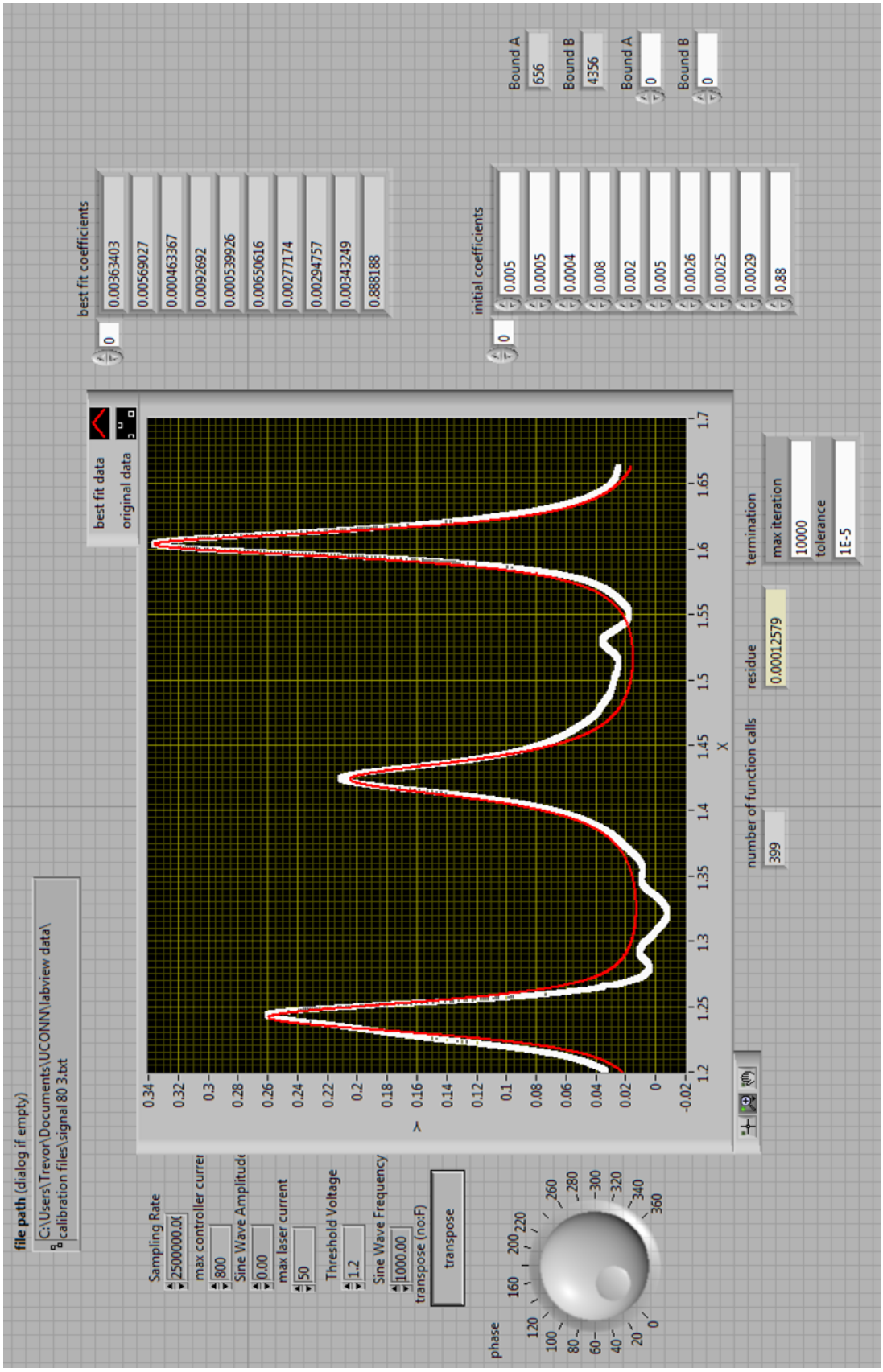
file path (dialog if empty)
C:\Users\Trevor\Documents\UCONN\labview data\calibration files\signal 80 3.txt
Sampling Rate
2500000.0
max controller curre
800
Sine Wave Amplitud
0.00
max laser current
50
Threshold Voltage
1.2
Sine Wave Frequency
1000.00
transpose (no:F)
transpose
phase
best fit data
original data
Y
X
best fit coefficients
0
0.00363403
0.00569027
0.000463367
0.0092692
0.000539926
0.00650616
0.00277174
0.00294757
0.00343249
0.888188
initial coefficients
0
0.005
0.0005
0.0004
0.008
0.002
0.005
0.0026
0.0025
0.0029
0.88
Bound A
656
Bound B
4356
Bound A
0
Bound B
0
number of function calls
399
residue
0.00012579
termination
max iteration
10000
tolerance
1E-5

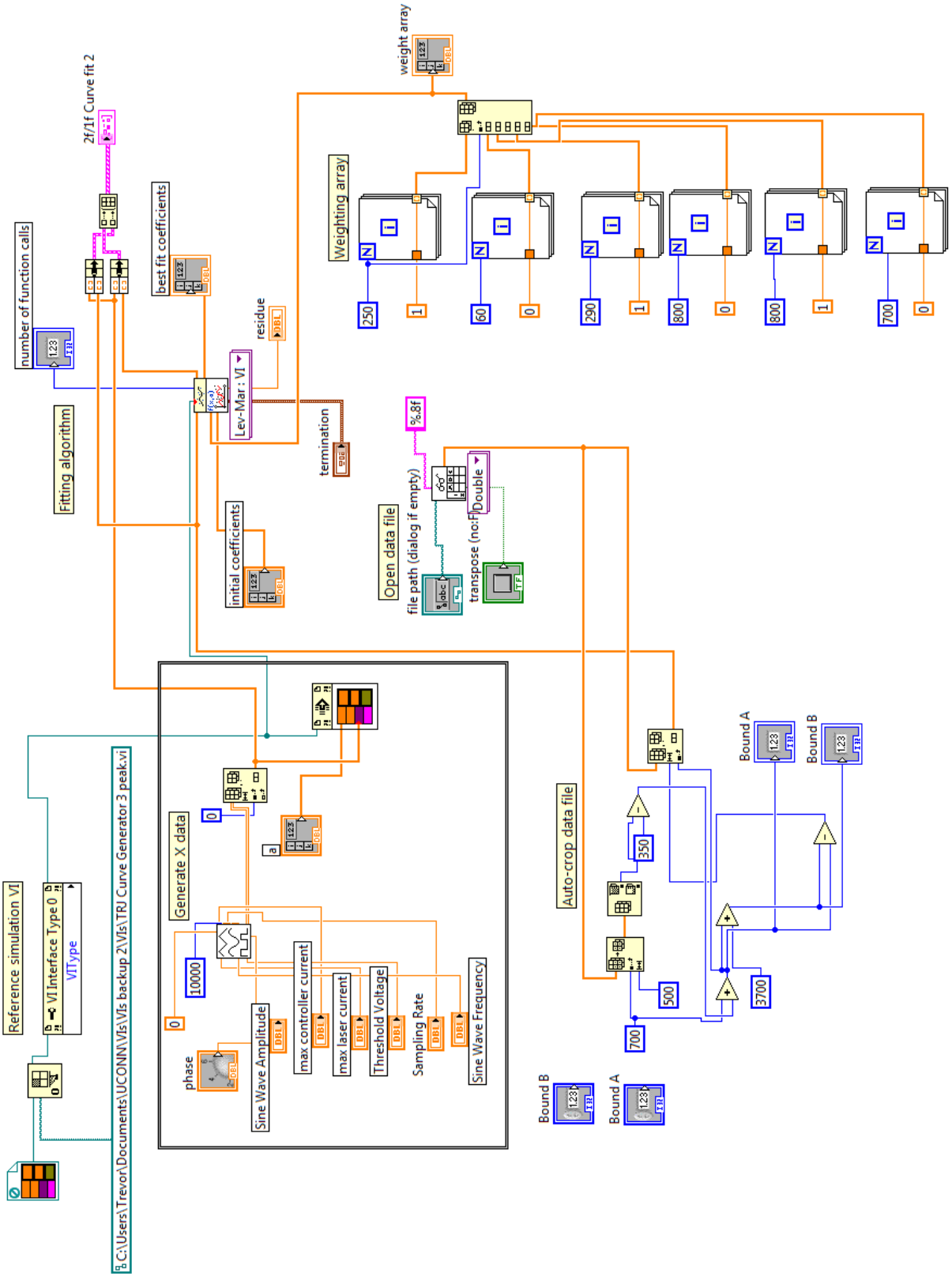
weight array
2f/1f Curve fit 2
Weighting array
best fit coefficients
number of function calls
residue
Lev-Mar : VI
termination
Fitting algorithm
initial coefficients
Open data file
%.8f
file path (dialog if empty)
transpose (no:F)
Double
Generate X data
Reference simulation VI
VI Interface Type 0
VIType
C:\Users\Trevor\Documents\UCONN\VIs\VIs backup 2\VIs\TRJ Curve Generator 3 peak.vi
phase
Sine Wave Amplitude
max controller current
max laser current
Threshold Voltage
Sampling Rate
Sine Wave Frequency
Auto-crop data file
Bound A
Bound B
Bound B
Bound A

References

[1] Lewis, B., and von Elbe, G., "Stability and Structure of Burner Flames," *Journal of Chemical Physics*, Vol. 11, No. 2, 1943, pp. 75-97.

[2] Zukoski, E. E., "Flame Stabilization on Bluff Bodies at Low and Intermediate Reynolds Numbers," Ph. D. Thesis, California Institute of Technology, Pasadena, CA, 1954.

[3] Tuttle, S. G., "Blowoff Behavior of Bluff Body Stabilized Flames in Vitiated and Partially Premixed Flows," Ph.D. Dissertation, UCONN, Storrs, CT, 2010.

[4] Williams, G. C., Hottel, H. C., and Scurlock, A., "Flame Stabilization and Propagation in high Velocity Gas Streams," *Symposium on Combustion, Flame and Explosion Phenomena Proceedings*, Vol. 3, 1949, pp. 21–40.

[5] Shanbhogue, S. J., Plaks, D. V., Nowicki, G., Preetham, and Lieuwen, T. C., "Response of Rod Stabilized Flames to Harmonic Excitation: Shear Layer Rollup and Flame Kinematics*," 42nd AIAA/ASME/SAE/ASEE Joint Propulsion Conference*, Sacrament, California, AIAA Paper 2006-5232, 2006.

[6] Oertel, H., "Wakes Behind Blunt Bodies," *Annu. Rev. Fluid Mech.*, Vol. 22, 1990, pp. 539-564.

[7] Williamson, C. H. K., "Vortex Dynamics in the Cylinder Wake," *Annu. Rev. Fluid Mech.*, Vol. 28, 1996, pp. 477-539.

[8] Ebrahimi, H. B., "Overview of Gas Turbine Augmentor Design, Operation and Combustion Oscillation," *42nd AIAA/ASME/SAE/ASEE Joint Propulsion Conference*, Sacramento, California, AIAA Paper 2006-4916, 2006.

[9] Lovett, J. A., Brogan, T. P., Philippona, D. S., Keil, B. V. and Thompson, T. V., "Development Needs For Afterburner Design," *40th AIAA/ASME/SAE/ASEE Joint Propulsion Conference*, Fort Lauderdale, Florida, AIAA Paper 2004-4912, 2004.

[10] Peters, N., *Turbulent Combustion*, Cambridge University Press, New York, 2000, pp. 78-86.

[11] Damköhler, G., and Zeitschr, F., "Influence of Turbulence on the Velocity Flames in Gas Mixtures," *Z. Elektrochem. Angew. Phys. Chem.*, Vol. 46, No. 11, 1940, pg. 601.

[12] Knaus, D. A., Sattler, S. S., and Gouldin, F. C., "Three-Dimensional Temperature Gradients in Premixed Turbulent Flamelets via Crossed-Plane Rayleigh Imaging," *Combustion and Flame*, Vol. 141, 2005, pp. 253-270.

[13] Bilger, R. W., "Future Progress in Turbulent Combustion Research," *Progress in Energy and Combustion Science*, Vol. 26, 2000, pp. 367-380.

[14] Law, C.K., *Combustion Physics*, Cambridge University Press, New York, 2006, pp. 396-400.

[15] Smith, C., Nickolaus, D., Leach, T., Kiel, B., and Garwick, K., "LES Blowout Analysis of Premixed Flow Past V-gutter Flameholder," *45th AIAA Aerospace Sciences Meeting and Exhibit*, Reno, Nevada, AIAA Paper 2007-170, 2007.

[16] Ghoniem, A., Annaswamy, A., Wee, D., Yi, T., and Park, S., "Shear Flow-Driven Combustion Instability: Evidence, Simulation, and Modeling," *Proceedings of the Combustion Institute*, Vol. 29, 2002, pp. 53-60.

[17] Lieuwen, T., Shanbhogue, S. J., Khosla, S., and Smith, C., "Dynamics of Bluff Body Flames near Blowoff," *45th AIAA Aerospace Sciences Meeting and Exhibit*, Reno, Nevada, AIAA Paper 2007-0169, 2007.

[18] Huerre, P., and Monkewitz, P. A., "Local and Global Instabilities in Spatially Developing Flows," *Annu. Rev. Fluid Mech*, Vol. 22, 1990, pp. 473-537.

[19] Prasad, A., and Williamson, A., "The Instability of the Shear Layer Separating from a Bluff Body," *Journal of Fluid Mechanics*, Vol. 333, 1997, pp. 375-402.

[20] Mehta, P. G., and Soteriou, M. C., "Combustion Heat Release Effects on the Dynamics of Bluff Body Stabilized Premixed Reacting Flows," *41st Aerospace Sciences Meeting and Exhibit*, AIAA Paper 2003-835, 2003.

[21] Nicholson, H., and Field, J., "Some Experimental Techniques for the Investigation of the Mechanism of Flame Stabilization in the Wake of Bluff Bodies," *Proceedings of the Combustion Institute*, Vol. 3, 1951, pp. 44-68.

[22] Thurston, D.W., "An Experimental Investigation of Flame Spreading from Bluff Body Flameholders," Thesis, California Institute of Technology, Pasadena, CA, 1958.

[23] Williams, G. C., Hottel, H. C., and Scurlock, A. C., "Flame Stabilization and Propagation in High Velocity Gas Streams," *Third Symposium on Combustion Flame and Explosion Phenomena Proceedings*, Baltimore, MD, 1949, pp. 21-40.

[24] Longwell, J. P., Frost, E. E., and Weiss, M. A., "Flame Stability in Bluff Body Recirculation Zones," *Industrial Engineering Chemistry*, Vol. 45, 1953, pp. 1629-1633.

[25] Zukoski, E. E., and Marble, F. E., "The Role of Wake Transition in the Process of Flame Stabilization on Bluff Bodies," *AGARD Combustion Researches and Reviews*, Butterworth Scientific Publishers, London, 1955, pp. 167-180.

[26] Plee, S. L., and Mellor, A. M., "Characteristic Time Correlation for Lean, Blowoff of Bluff Body Stabilized Flames," *Combust. Flame*, Vol. 35, 1979, pp. 61–80.

[27] Rao, K. V. L., and Lefebvre, A. H., "Flame Blowoff Studies Using Large Scale Flameholders," *ASME Journal of Engineering Power*, Vol. 104, No. 4, 1982, pp. 853–857.

[28] Lefebvr, A.H., *Gas Turbine Combustion*, 2nd Ed., CRC Press, Boca Raton, Florida, 1998, pp. 53-57.

[29] Sun, C. J., Sung, C. J., He, L., and Law, C. K., "Dynamics of Weakly Stretched Flames: Quantitative Description and Extraction of Global Flame Parameters," *Combustion and Flame*, Vol. 118, 1999, pp. 108-128.

[30] Bechtold, J. K., and Matalon, M., "Effects of Stoichiometry on Stretched Premixed Flames," *Combustion and Flame*, Vol. 119, 1999, pp. 217-232.

[31] Sung, C. J., Liu, J. B., and Law, C. K., "On the Scalar Structure of Nonequidiffusive Premixed Flames in Counterflow," *Combustion and Flames*, Vol. 106, 1996, pp. 168-183.

[32] Karlovitz, B., Denniston, D. W., Knapschaefer, D. H., and Wells, F. E., "Studies on Turbulent Flames," *Proc. Combust Inst.*, Vol. **4**, 1953, pp. 613-620.

[33] Nair, S. and Lieuwen, T., "Near Blowoff Dynamics of Bluff Body Stabilized Flames," *Journal of Propulsion and Power*, Vol. 23, No. 2, 2007, pp. 421-427.

[34] Kobayashi, H. and Kitano, M., "Extinction Characteristics of a Stretched Cylindrical Premixed Flame," *Combustion and Flame*, Vol. 76, No. 3-4, 1989, pp. 285-296.

[35] Wang, P., Hu, S., Wehrmeyer, J., and Pitz, R., "Stretch and Curvature Effects on Flames," *42nd AIAA Aerospace Sciences Meeting and Exhibit*, AIAA Paper 2004-148, 2004.

[36] Rehm, J. E. and Clemens, N. T., "Relationship between Vorticity/Strain and Reaction Zone Structure in Turbulent Non-Premixed Jet Flames," *Proceedings of the Combustion Institute*, Vol. 27, 1998, pp. 1113-1120.

[37] Chaudhuri, S., Kostka, S., Renfro, M., and Cetegen, B., "Blowoff Dynamics of Bluff Body Stabilized Two Dimensional Turbulent Premixed Flames," *Combustion and Flame*, Vol. 157, 2010, pp. 790-802.

[38] Laurendeau, N. M., *Statistical Thermodynamics: Fundamentals and Applications*, Cambridge University Press, New York, 2005, Chap. 11.

[39] Bernath, P. F., *Spectra of Atoms and Molecules*, 2nd ed., Oxford University Press, New York, 2005, pp. 21-41.

[40] Arroyo, M. P., and Hanson, R. K., "Absorption Measurements of Water-Vapor Concentration, Temperature, and Line-Shape Parameters Using a Tunable InGaAsP Diode Laser," *Applied Optics*, Vol. 32, 1993, pp. 6104-6116.

[41] Sobelman, I. I., Vainshtein, L. A., and Yukov, E. V., *Excitation of Atoms and Broadening of Spectral Lines*, 2nd Ed., Springer-Verlag, New York, 2002, pp. 237-269.

[42] Lorentz, H. A., Koninklijke Akad. Wetenschappen, Amsterdam, Versl., 14, 518, 577(1905-1906).

[43] Armstrong, B. H., ''Spectrum Line Profiles: the Voigt Function,'' *J. Quant. Spectrosc. Radiat. Transfer*, Vol. 7, 1967, pp. 61–88.

[44] Gautschi, W., ''Algorithm 363, Complex Error Function [S15],'' *Commun. ACM*, Vol. 12, 1969, pg. 635.

[45] Humlicek, J., ''An Efficient Method for Evaluation of the Complex Probability Function: the Voigt Function and its Derivatives,'' *J. Quant. Spectrosc. Radiat. Transfer*, Vol. 21, 1979, pp. 309–313.

[46] Liu, Y., Lin, J., Huang, G., Guo, Y., and Duan, C., "Simple Empirical Analytical Approximation to the Voigt Profile," *J. Opt. Soc. Am. B.*, Vol. 18, 2001, pp. 666-672.

[47] Moses, E. I., and C.L. Tang, "High-Sensitivity Laser Wavelength-Modulation Spectroscopy," *Opt. Lett.*, Vol. 1, 1977, pp. 115-117.

[48] Bjorklund, G. C., "Frequency-Modulation Spectroscopy: A New Method for Measuring Weak Absorptions and Dispersions," *Opt. Lett.*, Vol. 5, 1980, pp. 15-17.

[49] Fernholz, T., Teichert, H., and Ebert, V., "Digital, Phase-Sensitive Detection for in situ Diode-Laser Spectroscopy under Rapidly Changing Transmission Conditions," *Appl. Phys. B*, Vol. 75, 2002, pp. 229-236.

[50] Li, H. J., Rieker, G. B., Liu, X., Jeffries, J. B., and Hanson, R. K., "Extension of Wavelength-Modulation Spectroscopy to Large Modulation Depth for Diode Laser Absorption Measurements in High-Pressure Gases," *Appl. Opt.*, Vol. 45, No. 2, 2006, pp. 1052-1061.

[51] Li, H. J., Rieker, G. B., Liu, X., Jeffries, J. B., Hanson, R. K., Allen, M. G., Wehe, S. D., Mullhall, P. A., and Kindle, H. S., "A Diode Laser Sensor for Rapid, Sensitive Measurements of Gas Temperature and Water Vapour Concentration at High Temperatures and Pressures, "*Meas. Sci. Technol.*, Vol. 18, 2007, pp. 1195-1204.

[52] Rea, E. C. and Hanson, R. K., "Rapid Laser-Wavelength Modulation Spectroscopy Used as a Fast Temperature Measurement Technique in Hydrocarbon Combustion," *Appl. Opt*., Vol. 27, 1988, pp. 4454-4464.

[53] Upschulte, B. L., Sonnenfroh, D. M., and Allen, M. G., "Measurements of CO, CO_2, OH, and H_2O in Room-Temperature and Combustion Gases by Use of a Broadly Current-Tuned Multisection InGaAsP Diode Laser," *Applied Optics*, Vol. 38**,** No. 9, 1999, pp. 1506-1512.

[54] Hanson, R. K., Kuntz, P. A., and Kruger, C. H., "High-Resolution Spectroscopy of Combustion Gases Using a Tunable Ir Diode Laser," *Applied Optics*, Vol. 16, No. 8, 1977, pp. 2045-2048.

[55] Hanson, R. K., Jeffries, J. B., and Allen, M. G., "Tunable Diode Laser Absorption Sensor Applications to Aeropropulsion Testing," NATO RSM-017 Applied Vehicle Technology Panel Specialists' Meeting on Recent Developments in Non-Intrusive Measurement Technology, Budapest, Hungary, 2005. (RTO-MP-AVT-124)

[56] Çengel, Y. A., and Boles, M. A., "Thermodynamics: An Engineering Approach," 6^{th} ed., McGraw-Hill, Boston, 2006, pp. 863-865.

[57] Brokaw, R. S., "Viscosity of Gas Mixtures," NASA Technical Note, NASA TN D-4496, 1968.

[58] Boucher, T. J., "The Design and Development of an In-Situ Laser Diagnostic Tool for Water Measurements in a Commercial PEM Fuel Cell," Master's Thesis, UCONN, Storrs, CT, 2009.

[59] Furlong, E. R., "Diode-Laser Absorption Spectroscopy Applied for the Active Control of Combustion," PhD Dissertation, Stanford University, Stanford, CA, 1998.

[60] Berkooz, G., Holmes, P., and Lumley, J. L., "The Proper Orthogonal Decomposition in the Analysis of Turbulent Flows," *Annu. Rev. Fluid Mech.*, Vol. 25, 1993, pp. 539-575.

[61] Singer, M. A., and Green, W. H., "Using Adaptive Proper Orthogonal Decomposition to Solve the Reaction-Diffusion Equation," *Applied Numerical Mathematics*, Vol. 59, 2009, pp. 272-279.

[62] Lumley, J. L., "The Structure of Inhomogeneous Turbulence," *Atmospheric Turbulence and Wave Propagation*, ed. A. M. Yaglom, V. I. Tatarski, Moscow: Nauka, 1967, pp. 166-178.

[63] Shvartsman, S. Y., Theodoropoulos, C., Rico-Martinez, R., Kevrekidis, I. G., Titi, E. S., and Mountziaris, T. J., "Order Reduction for Nonlinear Dynamic Models of Distributed Reacting Systems," *J. Process Control*, Vol. 10, 2000, pp. 177-184.

[64] Pinnau, R., and Schulze, A., "Model Reduction Techniques for Frequency Averaging in Radiative Heat Transfer," *J. Comput. Phys.*, Vol. 226, No. 1, 2007, pp. 712-731.

[65] Graham, M. D., and Kevrekidis, I. G., "Alternative Approaches to the Karhunen-Loève Decomposition for Model Reduction and Data Analysis," *Comput. Chem. Engr.*, Vol. 20, No. 5, 1996, pp. 495-506.

[66] Zhang, X., and Perot, B., "Turbulent Vortex Shedding from Triangle Cylinder Using the Turbulent Body Force Potential Model," *ASME 2000 Fluids Engineering Division Summer Meeting*, Boston, Massachusetts, FEDSM2000-11172, 2000.

[67] Jensen, T. R., Kopp-Vaughan, K. M., Biswas, S., Renfro, M. W., and Cetegen, B. M., "High-Speed Imaging of Near-Blowoff Behavior for Bluff-Body Stabilized Flames in Vitiated Flow with Stratified Fueling," *7th US National Technical Meeting of the Combustion Institute*, Atlanta, Georgia, 2011.

[68] Kopp-Vaughan, K. M., Jensen, T. R., Cetegen, B. M., and Renfro, M. W., "Blowoff Dynamics and Time Series Analysis of Bluff Body Stabilized Stratified Flames," *7th US National Technical Meeting of the Combustion Institute*, Atlanta, Georgia, 2011.

[69] *MatLab*, Software Package, Ver. R2007A, The MathWorks, Inc., Natick, MA, 2007.

[70] Rothman, L. S., Gordon, I. E., Barbe, A., Chris Benner, D., Bernath, P. F., Birk, M., Boudon, V., Brown, L. R., Campargue, A., Champion., J.-P., Chance, K., Coudert, L. H., Dana, V., Devi, V. M., Fally, S., Flaud, J.-M., Gamache, R. R., Goldman, A., Jacquemart, D., Kleiner, I., Lacome, N., Lafferty, W. J., Mandin, J.-Y., Massie, S. T., Mikhailenko, S. N., Miller, C. E., Moazzen-Ahmadi, N., Naumenko, O. V., Nikitin, A. V., Orphal, J., Perevalov, V. I., Perrin, A., Predoi-Cross, Rinsland, C. P., Rotger, M., Simeckova, M., Smith, M. A. H., Sung, K., Tashkun, S. A., Tennyson, J., Toth, R. A., Vandaele, A. C., and Vander Auwera, J., "The *HITRAN* 2008 Molecular Spectroscopic Database," *J. Quant. Spectrosc. & Radiat. Transfer*, Vol. 110, 2009, pp. 533-572.

[71] Zhou, X., Liu, X., Jeffries, J. B., and Hanson, R. K., “Development of a Sensor for Temperature and Water Vapor Concentration in Combustion Gases Using a Single Tunable Diode Laser,” *Meas. Sci. and Technology*, Vol. 14, 2003, pp. 1459-1468.

[72] Zhou, X., “Diode-Laser Absorption Sensors for Combustion Control,” Ph.D. Dissertation, Stanford University, Stanford, CA, 2005.

[73] Dharamsi, A. N., and Bullock, A. M., “Application of Wavelength-Modulation Spectroscopy in Resolution of Pressure and Modulation Broadened Spectra,” *Appl. Phys. B*, Vol. 63, 1996, pp. 283-292.

[74] Reid, J., and Labrie, D., “ Second-Harmonic Detection with Tunable Diode Lasers – Comparison of Experiment and Theory,” *Appl. Phys. B.*, Vol. 26, 1981, pp. 203-210.